National Library
of Canada

Acquisitions and
Bibliographic Services Branch

395 Wellington Street
Ottawa, Ontario
K1A 0N4

Bibliothèque nationale
du Canada

Direction des acquisitions et
des services bibliographiques

395, rue Wellington
Ottawa (Ontario)
K1A 0N4

Your file Votre référence

Our file Notre référence

NOTICE

The quality of this microform is heavily dependent upon the quality of the original thesis submitted for microfilming. Every effort has been made to ensure the highest quality of reproduction possible.

If pages are missing, contact the university which granted the degree.

Some pages may have indistinct print especially if the original pages were typed with a poor typewriter ribbon or if the university sent us an inferior photocopy.

Reproduction in full or in part of this microform is governed by the Canadian Copyright Act, R.S.C. 1970, c. C-30, and subsequent amendments.

AVIS

La qualité de cette microforme dépend grandement de la qualité de la thèse soumise au microfilmage. Nous avons tout fait pour assurer une qualité supérieure de reproduction.

S'il manque des pages, veuillez communiquer avec l'université qui a conféré le grade.

La qualité d'impression de certaines pages peut laisser à désirer, surtout si les pages originales ont été dactylographiées à l'aide d'un ruban usé ou si l'université nous a fait parvenir une photocopie de qualité inférieure.

La reproduction, même partielle, de cette microforme est soumise à la Loi canadienne sur le droit d'auteur, SRC 1970, c. C-30, et ses amendements subséquents.

Canada

UNIVERSITY OF ALBERTA

$MoSi_2$ DIFFUSION BARRIER FOR THE PASSIVATION OF COPPER AT ELEVATED TEMPERATURES

BY

Robert CVITKOVIC

©

A thesis submitted to the Faculty of Graduate Studies and Research in partial fulfillment of the requirements for the degree of **MASTER OF SCIENCE**.

IN

METALLURGICAL ENGINEERING

DEPARTMENT OF **MINING, METALLURGICAL AND PETROLEUM ENGINEERING**

EDMONTON, ALBERTA

Fall 1994

National Library
of Canada

Acquisitions and
Bibliographic Services Branch

395 Wellington Street
Ottawa, Ontario
K1A 0N4

Bibliothèque nationale
du Canada

Direction des acquisitions et
des services bibliographiques

395, rue Wellington
Ottawa (Ontario)
K1A 0N4

Your file Votre référence

Our file Notre référence

The author has granted an irrevocable non-exclusive licence allowing the National Library of Canada to reproduce, loan, distribute or sell copies of his/her thesis by any means and in any form or format, making this thesis available to interested persons.

L'auteur a accordé une licence irrévocable et non exclusive permettant à la Bibliothèque nationale du Canada de reproduire, prêter, distribuer ou vendre des copies de sa thèse de quelque manière et sous quelque forme que ce soit pour mettre des exemplaires de cette thèse à la disposition des personnes intéressées.

The author retains ownership of the copyright in his/her thesis. Neither the thesis nor substantial extracts from it may be printed or otherwise reproduced without his/her permission.

L'auteur conserve la propriété du droit d'auteur qui protège sa thèse. Ni la thèse ni des extraits substantiels de celle-ci ne doivent être imprimés ou autrement reproduits sans son autorisation.

ISBN 0-315-95021-8

Canada

UNIVERSITY OF ALBERTA

RELEASE FORM

NAME OF AUTHOR: **Robert Cvitkovic**

TITLE OF THESIS: **$MoSi_2$ Diffusion Barrier for the Passivation of Copper at Elevated Temperatures**

DEGREE: **Master of Science**

YEAR THIS DEGREE GRANTED: **Fall 1994**

Permission is hereby granted to the University of Alberta Library to reproduce single copies of this thesis and to lend or sell such copies for private, scholarly or scientific research purposes only.

The author reserves all other publication and other rights in association with the copyright in the thesis, and except as hereinbefore provided neither the thesis nor any substantial portion thereof may be printed or otherwise reproduced in any material form whatever without the author's prior written permission.

3165 Mulberry Court
Windsor, Ontario, Canada
N8R-2A4

Date: Aug 31/94

UNIVERSITY OF ALBERTA

FACULTY OF GRADUATE STUDIES AND RESEARCH

The undersigned certify that they have read, and recommend to the Faculty of Graduate Studies and Research for acceptance, a thesis entitled **$MoSi_2$ DIFFUSION BARRIER FOR THE PASSIVATION OF COPPER** submitted by **Robert Cvitkovic** in partial fulfillment of the requirements for the degree of **MASTER OF SCIENCE** in **METALLURGICAL ENGINEERING.**

Dr. D.G. Ivey
Supervisor

Dr. S.A. Bradford

Dr. U. Sundararaj

Date: Aug. 31/94.

To

My Family

Abstract

Copper is increasingly being studied as a low cost electrical interconnect in VLSI and thick film technologies. Copper has superior electromigration resistance and has good conductivity. Unfortunately copper oxidizes readily at elevated temperatures. Because processing involves high temperatures, in order to have a useable copper interconnect, oxidation issues must be addressed.

Sputter deposited $MoSi_2$ coatings on copper have been studied in an attempt to slow or prevent the oxidation of copper. Two thicknesses of $MoSi_2$ were studied, namely 200nm and 400nm, in metallization systems of $Si/SiO_2/Cu/MoSi_2$. Samples were exposed to an air ambient between 600°C and 850°C for up to 15 minutes. Sputter deposited $MoSi_2$ is amorphous upon deposition. Silicon from the $MoSi_2$ was found to diffuse into the copper causing the $MoSi_2$ to transform to lower silicides. Because of the reduced amount of copper ions reaching the surface, CuO formed with very minute amounts of Cu_2O. The decrease in the amount of copper consumed by the oxide, with a 200nm $MoSi_2$ coating, was reduced by ~140x at 600°C, and ~30x at 800°C. The mechanism for copper diffusion through a 400nm $MoSi_2$ coating appears to be different than for a 200nm coating. This is due to the loss of silicon and the phase transformations that occur for the various barrier thicknesses. A 400nm $MoSi_2$ coating further reduced the amount of copper consumed by oxidation by ~420x at 600°C, and ~200x at 850°C. This translates to a 35 nm CuO layer for a 400nm $MoSi_2$ coating at 600°C and a 300nm thick oxide layer at 850°C, for 15 minutes in an air ambient.

Acknowledgements

I am greatly indebted to Dr. D. G. Ivey for his supervision of this project and his support throughout my stay at the University of Alberta.

I wish to thank Sherritt for their financial support, for providing this project with many of the necessary materials, and for the use of their facilities in Fort Saskatchewan. I wish to thank the staff at Sherritt who helped in this project, namely, Dr. J. Stiles my Sherritt contact, and the technical staff, Dan Seale, Kelvin Lobbin, and Sandra Dexter.

I am grateful to the Alberta Microelectronic Centre for the thin film depositions they carried out for me. I would especially like to thank Graham McKinnon and Mike Konoveki who accommodated my repeated requests for samples. Also, thanks are due to Dr. R. Mikula for access to the atomic force microscope at CANMET.

I am also grateful to the technical staff at the University of Alberta, especially Tina Barker's scanning electron microscopy help. Special thanks to the Wisest student, Cheryl Steer, for her help with TEM samples.

I would like to thank J. Suzuki for the invaluable motivation she gave me and finally to my parents, for their support, the least of which was financial during the long course of my academic education.

Table of Contents

Chapter 1
Introduction 1

Chapter 2
Oxidation Theory 5

2.1 Fundamentals of Oxidation 5
2.2 Simplified Treatment of Diffusion Controlled Oxidation 8
2.3 Theory of Multilayed Scale Growth 10
2.4 Double Oxide Layer on Pure Copper; Experimental Results 11
2.5 Oxidation of Silicon 13
2.6 Protective Coatings 14

Chapter 3
Diffusion Barriers 22

3.1 The Thick Film Approach 22
3.1.1 Nitrogen Furnace Solution 22
3.1.2 Steel Vessel Solution 23
3.1.3 Boron Solution 24
3.2 The Diffusion Barrier Approach 25
3.2.1 Diffusion Barriers - Basic Theory 26
3.2.2 Types of Barriers 28
3.3 The Silicides 30
3.3.1 Transition Metal Silicide Stability 31
3.3.2 Empirical Data 32
3.3.3 Oxidation Mechanisms 33
3.3.4 Molybdenum Silicide 35
3.4 Borides, Nitrides, and Carbides 39
3.4.1 Empirical Data 40
3.5 The Selection Process 42

Chapter 4
Experimental Procedures 53

4.1 Substrates and Depositions 53
4.2 Annealing Procedure 54
4.3 X-Ray Diffraction 55
4.4 Light Microscopy 55
4.5 Atomic Force Microscopy 56
4.6 Scanning Electron Microscopy 56
4.7 Transmission Electron Microscopy 56
4.8 Thermal Gravimeteric Analysis 57

Chapter 5
Results and Discussion 63

5.1 Oxidation of Copper 63
5.2 Diffusion Barriers for Copper Substrates (Preliminary Work) 66
5.3 $MoSi_2$(200nm) Barrier Layer for Copper 73
5.3.1 Film Uniformity and Integrity (Surface Analysis) 73
5.3.2 X-Ray Diffraction Analysis 76
5.3.3 Oxide Phase Identification 77
5.3.4 Kinetics of Oxidation 80
5.3.5 Thermal Gravimetric Analysis 82
5.4 $MoSi_2$(400nm) Barrier Layer for Copper 104
5.4.1 Film Integrity for the $MoSi_2$(400nm) Coating 104
5.4.2 X-ray Diffraction Analysis 105
5.4.3 $MoSi_2$ Phase Transformation and Grain Growth 106
5.4.4 Kinetics of Oxidation 108

Chapter 6
Conclusions and Recommendations 121

6.1 Conclusions 121
6.2 Recommendations 122

References 123

Appendix A: Calculation Used for Tables 2-3a - d 129

Appendix B: Factors Which Affect Adhesion 131

Appendix C: Calculation for the Reduction of CuO to Copper by Ion Milling 133

Appendix D: Raw Data 134

List of Tables

Table		Page
2 - 1	Parablic rate constants for the oxidation of copper at various temperatures	18
2 - 2	Comparison of copper oxidation results from two different reseachers, Mrowec and Ananth et al. [11,31]	18
2 - 3 a	Copper oxide thicknesses at 850°C calculated from parabolic rate constants	19
2 - 3 b	Copper oxide thicknesses at 800°C calculated from parabolic rate constants	19
2 - 3 c	Copper oxide thicknesses at 700°C calculated from parabolic rate constants	20
2 - 3 d	Copper oxide thicknesses at 600°C calculated from parabolic rate constants	20
2 - 4	Oxide to metal volume ratios of some common metals	21
2 - 5	Linear coefficients of thermal expansion of some metals and oxides	21
3 - 1	Properties of refractory metal silicides and their oxides	49
3 - 2	Kinetics of SiO_2 growth by thermal annealing of silicide films in a dry oxidizing ambient	49
3 - 3	Bulk properties of the refractory metal carbides and nitrides	51
3 - 4	Resistivity and melting points for thin film ZrB_2 and TiB_2	52
3 - 5	Mass gain of a copper plate coated with ZrB_2 for various coating thicknesses	52
4 - 1	Cleaning procedures for copper substrates	59
4 - 2	Film depositions on copper substrates	59
4 - 3	Film depositions on alumina substrates	59
4 - 4	Film depositions on silicon substrates	60
4 - 5	Firing schedule for thin films on alumina and silicon substrates	60
5.1	A comparison of the parabolic rate constant of bare copper from the literature and this experiment	71

Table		Page
5 - 2	A comparisen of the rate constants, apparent activation energy, oxide thickness at 15 minutes, and copper consumed at 15 minutes for bare copper and Si/Cu/$MoSi_2$(200nm)	102
5 - 3	A comparison of the rate constants, apparent activation energy, oxide thickness at 15 minutes, and copper consumed at 15 minutes for bare copper and Si/Cu/$MoSi_2$(400nm)	120
6 - 1	Parabolic rate constants and oxide formation at 15 minutes for 200nm and 400nm $MoSi_2$ coatings on copper	121
B - 1	Summary of initial phase formation in copper/metal bilayers	132
D - 1	Raw data for the oxide thickness measurements of bare copper	134
D - 2	Raw data for the oxide thickness measurements for Si/Cu/$MoSi_2$(200nm) samples	135
D - 3	Raw data for the oxide thickness measurements for Si/Cu/$MoSi_2$(400nm) samples	135

List of Figures

Figure		Page
1 - 1	Schematic of a thick film hybrid microcircuit	2
2 - 1	Interfacial reactions and transport processes for high temperature oxidation	17
2 - 2	Schematic representation of the formation of metal deficit p-type semiconductor	17
2 - 3	Schematic scale structure of a double oxide layer on the surface of copper	18
3 - 1	First generation thick film air fired copper conductors	44
3 - 2	Second generation thick film air fired copper conductors	44
3 - 3	Arrhenius plot of self diffusion values for silver	45
3 - 4	Schematic of a sacrificial diffusion barrier that forms compounds	45
3 - 5	The effects of a sink on diffusion barriers	46
3 - 6	The effect of impurities on diffusion barriers	46
3 - 7	The oxide to metal volume ratio for various oxides of groups 4A to 6A elements	47
3 - 8	A plot of the melting points of the oxides of group 4A to 6A elements	47
3 - 9	The heats of formation per oxygen atom of various oxides of groups 4A to 6A elements	48
3 - 1 0	Schematic drawing showing the various steps of the pesting reaction occurring in single crystal $MoSi_2$	50
4 - 1	Typical thick film firing profile	61
4 - 2	Typical modified firing profile for test samples using an IR furnace	61
4 - 3 a	Schematic of the initial stages of a TEM cross-section sample	62
4 - 3 b	Schematic of TEM cross-section after dimpling	62
5 - 1	Illustration of the 100% and 90% line nomenclature	68
5 - 2	A typical firing profile	69
5 - 3	Optical micrograph of the oxide on bare copper 800°C for 15 minutes	69

Figure		Page
5 - 4	A plot of thickness squared vs. time for the oxidation of bare copper at 850°C	70
5 - 5	A plot of thickness squared vs. time for the oxidation of bare copper at 600°C, 700°C, 800°C, and 850°C	70
5 - 6	Arrhenius plot of the experimental rate constants	71
5 - 7	$Cu/MoSi_2$(150nm)/Ag(1000nm) SEM backscattered electron image. Annealed at 700°C for 10 minutes	72
5 - 8	Cu/Mo(200nm)/Ag(1000nm) SEM backscattered electron image. Annealed at 800°C for 10 minutes	72
5-9a	AFM 25μm scan plan view of $Al_2O_3/Cu/MoSi_2$(100nm) as deposited sample	84
5-9b	AFM 25μm scan plan view of $Si/Cu/MoSi_2$(100nm) as deposited sample	84
5-10a	AFM 25μm scan plan view of $Al_2O_3/Cu/MoSi_2$(200nm) as deposited sample	85
5-10b	AFM 25μm scan plan view of $Si/Cu/MoSi_2$(200nm) as deposited sample	85
5-11a	SEM secondary electron image of as deposited $Al_2O_3/Cu/MoSi_2$(200nm) sample	86
5-11b	SEM secondary electron image of as deposited $Si/Cu/MoSi_2$(200nm) sample	86
5-12	SEM secondary electron images of $Al_2O_3/Cu/MoSi_2$(200nm) samples	87
5-13	SEM secondary electron images of $Si/Cu/MoSi_2$(200nm) samples	88
5-14	$Al_2O_3/Cu/MoSi_2$(200nm) XRD spectra for 700°C	89
5-15	$Al_2O_3/Cu/MoSi_2$(200nm) XRD spectra for 800°C	90
5-16	$Si/Cu/MoSi_2$(200nm) XRD spectra for 700°C	91
5-17	$Si/Cu/MoSi_2$(200nm) XRD spectra for 800°C	92
5-18	TEM cross section images from a $Si/Cu/MoSi_2$(200nm) sample annealed at 700°C for 10 minutes	93
5-19	TEM cross section images and SAD indexed patterns for $Si/Cu/MoSi_2$(200nm) samples annealed at 700°C for 5 min	94
5-20	TEM cross section image, SAD pattern and EDX spectrum for $Si/Cu/MoSi_2$(200nm) as deposited sample	95
5-21	TEM cross section image EDX spectra for a $Si/Cu/MoSi_2$(200nm) sample annealed at 600°C for 5 minutes	96

Figure		Page
5-22	TEM cross section image EDX spectra for a Si/Cu/$MoSi_2$(200nm) sample annealed at 800°C for 2 minutes	97
5-23	A comparison of the same Si/Cu/$MoSi_2$(200nm) sample annealed at 700°C for 10 minutes, imaged in the SEM and TEM	98
5-24	SEM secondary electron image of a Si/Cu/$MoSi_2$(200nm) sample annealed at 850°C for 5 minutes	99
5-25	Kinetic plots for 600°C, 700°C, and 800°C for Si/Cu/$MoSi_2$(200nm) samples	100
5-26	Log plot of the data from Figure 5-25	101
5-27	Arrhenius plot of the rate constants from Figure 5-25	101
5-28	TGA plots for Al_2O_3/Cu/$MoSi_2$(200nm) samples	103
5-29a	AFM 14μm scan of Si/Cu/$MoSi_2$(400nm) as deposited sample	111
5-29b	AFM 14μm scan (3-dimensional view) of Si/Cu/$MoSi_2$(400nm) as deposited sample	111
5-30	SEM secondary electron image plan view of Si/Cu/$MoSi_2$(400nm) as deposited sample	112
5-31	The effect of surface roughness on the diffusion barrier	112
5-32	SEM secondary electron images comparing $MoSi_2$(200nm) and $MoSi_2$(400nm) coatings	113
5-33	Si/Cu/$MoSi_2$(400nm) XRD spectra for 700°C	114
5-34	Si/Cu/$MoSi_2$(400nm) XRD spectra for 800°C	115
5-35	TEM cross section image, and EDX spectra for a Si/Cu/$MoSi_2$(400nm) sample annealed at 800°C for 2 minutes	116
5-36	Comparison of the grain size and phases of Si/Cu/$MoSi_2$(400nm) sample	117
5-37	Kinetic plots for 600°C, 700°C, 800°C and 850°C for Si/Cu/$MoSi_2$(200nm) samples	118
5-38	Log plot of the data from Figure 5-37	119
5-39	Arrhenius plot of the rate constants from Figure 5-37	119

CHAPTER 1
INTRODUCTION

Thick Film Technology

A hybrid circuit is composed of thick and thin film components, semiconductor devices and discrete parts incorporated onto an insulating substrate (Figure 1-1). In many cases hybrids are used because there is no alternative technology. In the late sixties and early seventies when fast growing monolithic integrated circuits began to replace hybrids, many predicted the end of hybrid technology; however, hybrids survived and now they fill special niches in the micro-electronic industry. Two of their main applications are in microwave and high frequency circuits. Both thick and thin film technologies are used in the fabrication of hybrids. Thin films are a generic term used to describe films with a thickness of 10-1000 nm, whereas thick films range from 10^4-$5x10^4$ nm. They also differ in the type of deposition techniques used. Thin films are generally deposited using vacuum technology (sputtering, evaporation, etc.) whereas thick films are formulated into pastes, applied to the substrate by silk screening techniques, and fired (sintered).

Thick films are generally divided into three categories depending on the functional material: conductor, resistor, or dielectric. Each paste has similar constituents: the binder (or sometimes called glass frit), the vehicle which consists of organic solvents, and the functional element which could be a metal, alloy, oxide or ceramic material. Generally, the thick film conductor constitutes the largest quantity of the thick film pastes and has the largest costs associated with it. Thick film conductor pastes are traditionally made from precious metals such as gold, silver, palladium, and platinum, or combinations thereof. These are inorganic powders in organic fluid vehicles. The powders are made into pastes and are screen printed onto ceramic substrates, such as alumina. The pastes are dried, temporary binders are removed by air oxidation and then the paste is sintered at temperatures of about 850^{o}C. These pastes can be produced with the desired properties required for thick film conductors; namely, low resistivity, good adhesion to the substrate, solderability with high leaching

resistance, good line resolution, good screening properties, etc. The above mentioned metals do not oxidize in air at the processing temperatures needed to sinter the powders; however they are very expensive. There has always been an interest in developing low cost, non-noble metal thick film pastes as replacements for gold pastes, but it wasn't until gold approached 1000 dollars per ounce in 1978-80 that the industry became serious about developing them, and in particular copper pastes.

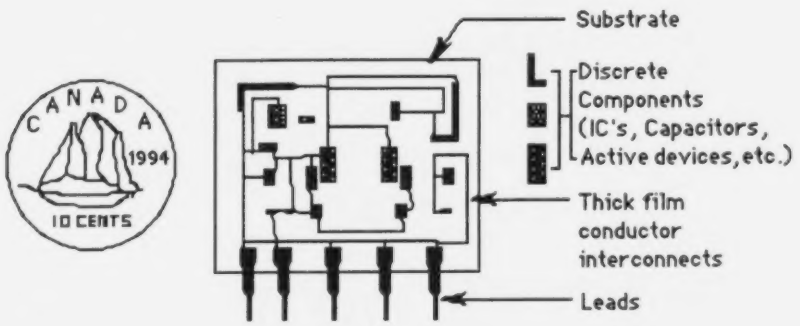

Figure 1-1: Schematic of a thick film hybrid microcircuit.

VLSI Technology

Interconnects electrically join various components on a substrate. They can determine performance limits for very large scale integration (VLSI) technology. Interconnects are becoming termed as devices in themselves because they perform the function of transmitting a signal reliably and are increasingly being designed to meet specific design requirements to do so. Copper is increasingly being studied as a new metallization material because of its low bulk electrical resistivity, good electromigration resistance, and low cost. As dimensions of VLSI circuits are scaled down in order to increase circuit density, stability and performance, interconnects are becoming more important, particularly for multilayered structures. There are advantages to using copper as an interconnect if a number of problems can be solved. Some of the problems associated with the use of copper interconnects include susceptibility to corrosion, diffusion into silicon, adhesion, and patterning. Other problems arise due to the type of application and the requirements imposed by processing.

The study of diffusion barriers has increased because of VLSI technology. VLSI technology has moved into the submicron range with complex multilayer structures of different materials. This has increased the possibility for material reactions or interdiffusion of materials in multilayer thin films. Thus, suitable diffusion barriers have been called upon to serve in the role of separating different layers to prevent undesired reactions or atomic migration. This is also one of the techniques being tried to passivate copper at elevated temperatures from oxidation. Passivation or encapsulation of copper may be one method for solving some of the problems with using copper as an interconnect.

Objective

The objective of this thesis was to prevent copper from oxidizing for 600 to 900 seconds during annealing at 850°C in an air ambient. This project was considered to be a preliminary study for determining which materials would be best for the passivation of copper. The potential application for such a coating would be for copper interconnects in VLSI applications or a coating for copper conductors in thick film applications. The main focus in this study was a thick film application, where individual copper powders might be coated prior to sintering. By applying a diffusion barrier to the surface of copper the rate of diffusion of the mobile species can be slowed. If the rate of diffusion is slowed enough for the processing conditions desired and for the life of the device, copper can be effectively passivated.

The processing criteria that were imposed on the diffusion barrier were taken from thick film technology. The processing constraints were:

1) Low diffusivity for oxygen, copper (and silver).
2) Immiscibility in copper (and silver), and vice versa.
3) Good electrical conductivity.
4) Good adhesion with copper (and silver).
5) Inexpensive processing.

The ultimate approach taken was to deposit a diffusion barrier onto the surface of copper to prevent it from oxidizing at the free surface. The goal was to find a diffusion

barrier to slow the rate of diffusion of copper to the free surface at 850°C for 600-900 seconds, so as to effectively prevent oxidation. The barrier chosen was $MoSi_2$. Details of the selection process are outlined in Chapter 3. Additionally, work was carried out on molybdenum, to continue work started by Sherritt Inc.

This thesis is organized into six chapters. A literature review is presented in Chapters 2 and 3. Oxidation theory as related to the oxidation of copper is presented in Chapter 2. Chapter 3 is a review of what has been done to passivate copper as a thick film, the relevant theory of diffusion barriers, and material properties used in the selection for possible barriers in the passivation of copper. Chapter 4 describes the experimental procedures used. Results and discussion are presented in Chapter 5. Chapter 6 gives conclusions and recommendations.

Chapter 2

Oxidation Theory

The mechanism by which ions and electrons transport through a growing oxide layer, as it applies to the oxidation of copper, is described below. For the case of surface oxidation where the oxide is uniform and continuous, the oxide separates the metal from the gas as: Metal(M)/Oxide(M_xO_y)/Gas(O_2). It is clear then that the mechanisms by which the reactants penetrate the oxide layer are an important part of the mechanism of high temperature oxidation [1].

2.1 Fundamentals of Oxidation

Metal oxides are ionic in nature. The mechanisms available to explain the transport of ions through ionic solids can be divided into stoichiometric and non-stoichiometric. There are two limiting cases for stoichiometric crystals, transport involving Schottky defects or Frenkel defects. Ionic mobility by means of Schottky defects is explained by ionic vacancies. Electroneutrality dictates an equivalent number or concentration of vacancies on both cation or anion sub-lattices. Since vacancies exist on both sub-lattices, it is expected that both anions and cations will be mobile. Frenkel defects represent the case where only the cations are mobile. It is assumed that the anion lattice is perfect and the cation lattice contains vacancies and interstitials in equivalent concentrations to maintain electroneutrality. However, neither defect structure can be used exclusively to explain material transport during oxidation because neither provides a mechanism for electron migration.

In order to explain the simultaneous migration of ions and electrons, it is necessary to assume the oxide(s) formed during oxidation are non-stoichiometric compounds. If cations are the dominant mobile species, (Figure 2-1a), then the scale will form at the scale/gas interface. If anions are the dominant mobile species then the

scale will form at the metal/scale interface (Figure 2-1b). The corresponding interfacial reactions are also given in Figure 2-1. By non-stoichiometry, it is implied that the metal to nonmetal atom ratio is not exactly that given by the chemical formula, even though the compound is electrically neutral. It is therefore necessary to assume that either the anion or the cation exhibits variable valency on its sub-lattice. It is much more likely that the metal or cation shows variable valency.

Nonstoichiometric ionic compounds are classified as semiconductors and may show negative or positive behaviour. Cu_2O is a p-type semiconductor. P-type semiconduction arises from the formation of vacancies on the cation lattice together with electron holes giving rise to conduction. The possibility of forming electron holes lies in the ability of many metal ions, especially the ions of transition metals, to exist in several valence states. The closer together the different valence states are in terms of energy of ionization, the more easily cation vacancy formation can be induced by the metal deficit p-type mechanism.

To visualize the defect structure, consider Figure 2-2; a schematic of the interaction of a NiO lattice with oxygen. NiO is a typical p-type metal deficient semiconductor with cation vacancies and electron holes. Step (a) in Figure 2-2 shows oxygen adsorbed onto the surface of the perfect crystal. In step (b) the oxygen chemisorbs by attracting an electron from a Ni^{2+} site thus forming an Ni^{3+} ion with a hole. In step (c) the chemisorbed oxygen is fully ionized forming another Ni^{3+} ion with a hole, and a Ni^{2+} ion enters the surface to partner the O^{2-} thus forming a vacancy in the cation sub-lattice. Note, the overall reaction in Figure 2-2, step (d) should be:

$$\frac{1}{2} O_2 = O_O + (V_{Ni})^{2-} + 2(h^+) \qquad (1)$$

instead of

$$\frac{1}{2} O_2 = NiO(s) + (V_{Ni})^{2-} + 2(h^+) \qquad \text{taken from Figure 2-2 step (d)}$$

The oxide, NiO in this case, is used instead of O_O in order to illustrate that the oxide has been formed. The latter equation will be used for the sake of convention, as given by Mrowec and others [2].

Now, using Cu_2O as an example, the defect equation for singly charged vacancies is given as:

$$\frac{1}{2} O_2(g) = Cu_2O(s) + 2(V^-) + 2(h^+) \qquad (2)$$

For the case of equilibrium, the equilibrium constant (K_p) is:

$$K_{eq} = \frac{[V^-]^2[h^+]^2}{(P_{O_2})^{1/2}} \qquad (3)$$

In Equation 3, the defects are in dilute solution in the oxide. Therefore, assuming that they are in the range obeying Henry's law, concentrations instead of activities are used. Henry's law states that the activity exerted by a component i in a solution is proportional to the mole fraction of i in the solution. If Equation 2 represents the only mechanism by which defects are created, then the concentration of singly charged vacancies is equal to the hole concentration by:

$$[V^-] = [h^+] \qquad (4)$$

Inserting (4) into (3):

$$K_{eq} = \frac{[V^-]^2[V^-]^2}{(P_{O_2})^{1/2}} \qquad (5)$$

and simplifying for the concentration of vacancies:

$$(P_{O_2})^{1/2} \cdot K_{eq} = [V^-]^4 \qquad (6)$$

$$[V^-] \alpha (P_{O_2})^{1/8} \qquad (7)$$

The electrical conductivity is expected to vary proportionally to the electron hole concentration and so with the eighth root of the oxygen partial pressure. However, it is also possible for the vacancies and electron holes to associate, producing uncharged copper vacancies [3]; this can be represented by:

$$\frac{1}{2} O_2(g) = Cu_2O(s) + 2(V) \qquad (8)$$

Using Equation 8, and following a similar method as above, the vacancy concentration is then:

$$[V] \alpha (P_{O_2})^{1/4} \qquad (9)$$

Each mechanism predicts a different dependence of defect concentration on oxygen partial pressure. Measurement of electrical conductivity as a function of oxygen partial pressure can serve to define the dependence law and indicates which defect is predominant. Since the formation of neutral vacancies does not involve electrical defects, their presence will not be detected by electrical conductivity measurements made as a function of oxygen partial pressure. However, neutral vacancies can and do affect the diffusion of cations. It will be shown later that the diffusion constant is also a function of partial pressure. Conversely, if the value of k_p (parabolic rate constant) is measured as a function of external oxygen partial pressure at a constant temperature the diffusion constant, D, and predominant type of defect(s) can be determined.

2.2 Simplified Treatment of Diffusion Controlled Oxidation

Assuming that ionic transport across the growing oxide layer controls the rate of scaling and that thermodynamic equilibrium is established at each interface, the process can be analyzed as follows. The outward cation flux, $J_{M^{2+}}$, is equal and opposite to the inward flux of cation defects (here taken to be vacancies). This is represented in Figure 2-1a and gives Equation 10:

$$J_{M^{2+}} = -J_V = D_V \frac{[V'']-[V']}{x} \qquad (10)$$

Where x is the oxide thickness, D_V is the diffusion coefficient for cation vacancies, and [V''] and [V'] are the vacancy concentrations at the gas/scale and scale/metal interface respectively.

Since there is thermodynamic equilibrium at each interface, the value of [V'']-[V'] is constant, which gives:

$$J_V = (\text{const})\frac{dx}{dt} = ([V'']-[V']) \frac{D_V}{x} \qquad (11)$$

Rearranging Equation (11) gives

$$\frac{dx}{dt} = \frac{k}{x} \qquad (12a) \qquad \text{where,} \qquad k = D_V \frac{[V'']-[V']}{\text{const.}} \qquad (12b)$$

Integrating and noting that x=0 at t=0:

$$x^2 = 2kt \qquad (13)$$

which is the common parabolic rate law.

It was shown in Equation 7 and 9 that the cation vacancy concentration is related to the oxygen partial pressure by:

$$[V] \alpha (P_{O_2})^{1/n} \qquad (14)$$

Substituting Equation 14 into 12b, the vacancy concentration values can be replaced with the partial pressures, and the variation of the parabolic constant with oxygen partial pressure can be predicted as:

$$k \alpha [(\bar{P}_{O_2})^{1/n} - (\grave{P}_{O_2})^{1/n}] \qquad (15)$$

Since $\grave{P}_{O_2}$ (scale/metal interface) is usually negligible compared with $\bar{P}_{O_2}$ (gas/scale interface):

$$k \alpha (\bar{P}_{O_2})^{1/n} \qquad (16)$$

Note, the derivation here has been simplified to explain the variation of parabolic rate constant with partial pressure. However, Wagner's theory of oxidation produces the same results and will not be discussed at this time. For a full derivation using Wagner's theory of oxidation see References [1,4].

2.3 Theory of Multilayered Scale Growth

The high temperature oxidation of many metals results in the formation of two or more product compounds, as in the case of pure copper. Ideally, the oxidation products form as flat, parallel layers on the surface of the metal. The compound richest in metal forms adjacent to the metal phase, and the compound poorest in metal forms adjacent to the gas phase, (i.e., $Cu/Cu_2O/CuO/O_2$). Assumptions for the formation of double-layered scale formation are: the reaction is diffusion controlled, the concentrations at the boundaries are constant, local equilibrium is attained at the phase boundaries, and cations and electrons are the predominant diffusers through the product layers.

The total oxidation reaction for pure copper can be written as:

$$3Cu + O_2 = Cu_2O + CuO \qquad (17)$$

Not all of the cations produced at the Cu/Cu_2O interface contribute to the growth of the lower oxide, (Cu_2O). Some of these cations must diffuse farther, through the CuO, in order to contribute to the growth of this oxide at the CuO/O_2 interface. The partitioning of the Cu cations between the two oxide layers can be demonstrated by considering the reactions that take place at each interface in the scale. The total oxidation reaction in Equation 17 is the sum of these interfacial reactions, given here as defect equations. Figure 2-3 illustrates the growth model [5], with the direction of cations, electrons and vacancies shown.

The consumption of the copper phase at the Cu/Cu_2O interface is:

$$3V^{1-} + 3Cu(s) = 3Cu^{1+} + 3e^- \quad (Cu/Cu_2O \text{ interface}) \qquad (18)$$

The Cu_2O grows at the expense of CuO at the Cu_2O/CuO interface, however, not all of the Cu ions that arrive at the Cu_2O/CuO interface contribute to the growth of the Cu_2O. The reactions at this interface are separated for the sake of clarification:

$$CuO(s) + Cu^{1+} + e^- = Cu_2O(s) + V^{1-} \qquad (19)$$

and (Cu_2O/CuO interface)

$$2V^{2-} + 2Cu^{1+} = 2Cu^{2+} + 2e^{-} + 2V^{1-} \qquad (20)$$

Finally, the CuO layer grows at the CuO/O_2 interface according to:

$$O_2(g) + 2Cu^{2+} + 4e^{-} = 2CuO(s) + 2V^{2-} \quad (CuO/O_2 \text{ interface}) \qquad (21)$$

Summing Equations 18 through 21 will give Equation 17. (Note, the above four equations will balance even if the vacancies are not considered, and it is easier to follow initially. But, for completeness, the vacancies on the cation sub-lattice are indicated.)

2.4 Double Oxide Layer on Pure Copper; Experimental Results

Again, considering the case of Cu_2O and CuO forming on the surface of copper, the oxidation reaction can be given by Equation 17 above. Copper cations diffuse to the Cu_2O/CuO interface and some of them form Cu_2O, while the rest diffuse to the CuO/O_2 interface to form CuO. CuO forms at the CuO/O_2 interface and is consumed at the Cu_2O/CuO interface. This model assumes a uniform and continuous scale across the surface of the metal. Yurek et al. [5] have proposed a theory to determine the thicknesses of simultaneously formed oxide layers. The ratio of the oxide thicknesses formed is given as a function of the average molar volume and the parabolic rate constants of the respective oxides, as shown by Equation 22. The ratio of the thicknesses of the two oxide layers, for simultaneous parabolic growth, is independent of reaction time at a particular temperature.

$$\frac{X(Cu_2O)}{X(CuO)} = \text{fcn}\{V(Cu_2O), \delta, k_p(Cu_2O), V(CuO), \upsilon, k_p(CuO)\} \qquad (22)$$

where X_i - thickness of the oxide,
V_i - average molar volume of the oxide,
δ, υ - the number of copper atoms per formula unit for each oxide,
$k_p(i)$ - parabolic oxidation constant for the respective oxide.

Garnaud [6], has taken Yurek's theoretical model of the growth of a double oxide on the surface of a metal and applied it to pure copper. Garnaud then used Valensi's [7] diffusion data to complete Equation 22 and compared theoretical calcuations to experimental data. The data is in very good agreement between 300°C and 700°C. This is supported by other studies on copper done by Paidassi [8] and Oudar [9], who had summarized the results of a number of researchers. There have been a number of

experimental studies done to support the model for a double oxide layer at intermediate temperatures (i.e., 300°C to 700°C), and Equation 22 is in good agreement with them.

However, it is the high temperature data which is not consistent from study to study. At high temperatures, Mrowec's data [10] gives a value of 9.2% CuO (at 900°C) which is very close to the 9.5% obtained with the above model (which assumes parabolic growth for Cu_2O and CuO). He also gives the pressure dependence to be $k_p \alpha (P_{O_2})^{1/4}$ which would indicate the predominant defect to be neutral vacancies (on the cation sub-lattice). Mrowec also reported an activation energy of 100.4 kJ/mol in the range of 850°C - 1050°C and $P_{O_2} = 1.01 \times 10^2$ - 8.1×10^4 Pa, (P_{O_2} (in air) = 2.127×10^4 Pa). Paidassi [8], on the other hand has shown the formation of CuO on Cu_2O does not follow the parabolic rate law. The amount of CuO is nonexistent below about 150°C, passes through a maximum between 300°C and 500°C and decreases again at higher temperatures.

Ananth et al. studied the high temperature oxidation of pure copper in a recent studies [11]. Oxidation studies conducted between 700°C - 900°C in dry air at $P_{O_2}=2.127 \times 10^4$ Pa gave an activation energy of 166.7±10 kJ/mol. The oxygen pressure dependence was $k_p \alpha P^{1/7}$, which suggests singly charged cation vacancies are predominant with a minor role played by neutral vacancies. The parabolic rate constants given for various temperatures are given in Table 2-1, [11,31]. This data is supported by other researchers as well. The rate constant at 850°C is quite comparable to that obtained from extrapolation of Moore and Selikson's data [13]. The activation energy is quite close to Moore and Castellan's value of Q=154.8 kJ/mol [14], for the diffusion of Cu^+ ions through Cu_2O, in a comparable temperature range. There is also good agreement with Hauffe's result of Q=159.0±8.4 kJ/mol [15].

Mrowec's results differ substantially. His results suggest a different mechanism by which the copper ions migrate (i.e., Mrowec suggested the presence of neutral vacancies in the growing Cu_2O layer, whereas Ananth et al. predicted singly charge vacancies). To clear up this discrepancy, we can consider Wagner's model [4]. It is proposed by Ananth et al. [11] that neutral vacancies have no role to play, since Wagner's diffusional growth has been assumed solely due to the migration of charge defect species. Therefore it is difficult to explain Mrowec's experimental results. Table 2-2 summarizes the results of Ananth et al. and Mrowec.

Furthermore, although the dual scale forms at intermediate temperatures (300°C - 700°C), and obeys the model proposed by Yurec and interpreted by Gaurnaud, it doesn't match the data at high temperatures as given by Ananth et al. and others. According to Kubaschewski and Hopkins [16], under the condition of high temperature reaction, CuO is not stable and Cu_2O is the only oxide present (for the oxidation of pure copper). According to Kroger's [17] analysis, the relative thickness of the two oxide layers comes out to be $X(CuO)/X(Cu_2O) \sim 10^{-4}$, at high temperatures, if both the layers grow according to parabolic kinetics. Furthermore, extensive study on the transformation of Cu_2O to CuO by Hauffe and Kofstad [18] shows the validity of a cubic law rather than a parabolic law, and the activation energy for CuO formation on Cu_2O, in the temperature range of 800°C - 900°C, is ~8.4 kJ/mol. Finally, according to Leroux and Raub [19], the CuO layer is prone to porosity.

Given all this, Ananth et al. concluded that the role played by CuO growth on Cu_2O can be neglected at high temperatures (i.e., greater than about 800°C). If the outer CuO growth takes place by a cubic law mechanism, then the thickness will be still smaller than that if the parabolic law was valid for the same time of exposure, which suggests that the ratio of $X(CuO)/X(Cu_2O)$ will be practically insignificant. Even if a thin layer of CuO forms, it must be porous and should not be considered at all. Also, the activation energy of CuO compared with that of Cu_2O is negligibly small and the CuO film is not a hindrance to the growth of Cu_2O on copper. Table 2-3a-d shows calculated mass gains from parabolic oxidation constants and oxide thicknesses for various temperatures and times. Examples of calculations used in Tables 2-3a-d are shown in Appendix A.

2.5 Oxidation of Silicon

High temperature oxidation of silicon has been extensively investigated due to its importance in silicon device technology [20-25]. Oxidation of silicon leads to the formation of a thin, non-crystalline scale of SiO_2, which is very protective. Deal and Grove [20] were the first to interpret the high temperature oxidation of silicon in dry oxygen in terms of a combined linear-parabolic equation (equation 23). The parabolic part is the rate determining diffusion of oxygen through the SiO_2 layer and the linear part is due to phase boundary reactions at the oxide interfaces and the solubility of oxygen in SiO_2.

$$x^2 + Ax = k_p(t + \tau) \qquad (23)$$

x is the scale thickness

t is time

k_p is the parabolic rate constant

k_p/A is the linear rate constant

τ is a time coordinate correction for the presence of an initial oxide thickness

This equation describes the overall oxidation between 700-1300°C for partial pressures of either oxygen or water vapour between 0.1 and 1 atm and for oxide thicknesses ranging from 30 to 2000 nm. Parabolic oxidation becomes increasingly important as the oxide thickness increases.

Studies of oxygen tracer distributions in growing SiO_2 [23,24] scales have confirmed that the diffusion controlled growth of SiO_2 takes place by inward oxygen transport. It was also shown [25] that oxidation in steam follows equation 23 and proceeds faster than that in dry oxygen. In wet oxygen the oxidation increases with increasing water vapour content. The activation energy associated with steam oxidation is smaller than that for dry oxidation.

2.6 Protective Coatings

Many metals are thermodynamically unstable with respect to ambient gases and will react to form oxides, sulphides, carbides, nitrides, etc. In dry oxygen atmospheres at room or low temperatures this instability may not pose any practical problem because the rates of reactions are low, but the reaction rates increase rapidly with temperature. The high temperature corrosion problem is encountered in many areas from high temperature processes in the chemical industry to structural materials, to the electronic industry. In this respect, it is necessary to understand the corrosion-oxidation process and it is essential to control high temperature oxidation. Of particular interest is the study of protective coatings.

The purpose of a corrosion resistant coating is to serve as an effective solid state diffusion barrier between oxygen (or other gaseous reactants) and the base material.

Most of the high temperature corrosion designers other than those for electronic applications generally do not consider resistivity a factor when choosing a coating material. In such cases then, protection is usually provided by continuous, highly stable oxide layers with low rates of solid state diffusion. Protective coatings are generally divided into three main groups depending on the type of protective scales that are formed: a) alumina formers, b) chromia formers, and c) silica formers. High temperature alloys may be also classified as diffusion coatings or overlay coatings. Diffusion coatings are formed through diffusional interaction between the coating material and the substrate alloy or may also be made by chromizing or siliconizing. Overlay coatings are applied by techniques such as vacuum evaporation (electron beam techniques), sputtering, plasma spraying, etc. [26]. Overlay coating techniques permit a high control of composition and flexibility in the design of coatings.

Coating Degradation

Coatings degrade by two main processes: a) diffusional interaction between coating and substrate; and b) degradation of the coating through reaction and interaction with the environment. Diffusional interaction between coating and substrate can take place through outward diffusion of the base metal into the coating or through inward diffusion of the coating component into the substrate. In either case the coating becomes diluted in the components that form the protective oxide scales. One case of the latter is $MoSi_2$ on Mo [27]. Silicon diffuses inwards into the substrate metal to form lower silicides Mo_5Si_3 and Mo_3Si. A 50 μm layer of $MoSi_2$ will be completely converted to lower silicides after 17 hours at 1500°C. The degradation of the coating through high temperature corrosion is usually more complex than that of the bulk material for various reasons. The cross-sectional composition of the coating, the method of application, and porosity can affect the coating's corrosion performance.

Stress Development in Oxide Films

Stress development in oxide layers can lead to spalling or cracking which reduces the effectiveness of a protective oxide layer. This has been discussed by a number of researchers [28,29]. The two principal sources of stress are growth stresses, which develop during the isothermal formation of the scale, and thermal stresses, which arise due to differential thermal expansion or contraction between the substrate and the scale.

The growth stresses may occur due to a number of causes which include:

a) volume differences between the oxide and the metal from which it forms;

b) epitaxial stresses;

c) compositional changes in the alloy or scale.

In 1923, Pilling and Bedworth [30] proposed the rule that oxide scales can be divided into two main classes with regard to the stresses that develop and the protective properties of scales. If the oxide to metal volume ratio (Pilling-Bedworth Ratio, PBR) is smaller than 1, the growth stresses will be tensile and the oxide will fail to cover the entire metal surface, hence it is non-protective. If the PBR is larger than 1, the stresses will be compressive and the oxide will initially be protective (Table 2-4). However, the Pilling-Bedworth principle has a limited applicability. The volume ratio is of minor importance when the oxidation proceeds via an outward migration of metal ions. When this is the case, the oxide is formed at the outer free surface and is not constrained to occupy the volume of the consumed metal. Epitaxial stresses are relevant during the initial nucleation stages of oxide growth and, as the scale thickens, the epitaxial constraints are reduced. Compositional stresses can occur by a number of means. Changes in scale composition due to selective oxidation, the dissolution of oxygen or impurities, or internal oxidation can result in stress development. There are other growth stresses that can arise in coatings such as specimen geometry and point defect stresses, but these will not be discussed here.

Even if no stress exists at the oxidation temperature, stresses will be generated during cooling due to the difference in thermal expansion coefficients of the metal and oxide. The magnitude of the stress will be proportional to the difference in thermal expansion coefficients [29]. The coefficient of thermal expansion for the oxide will generally be less than that of the metal and so compressive stresses in the oxide will develop in the oxide during cooling. Since the adhesive bond between metal and oxide is generally weaker than the cohesive bonds in either the metal or the scale, the result of large thermal stresses is generally spalling of oxide from the metal surface. This is the case for copper and chromium. Table 2-5 lists the linear coefficients of thermal expansion for some metals and oxides.

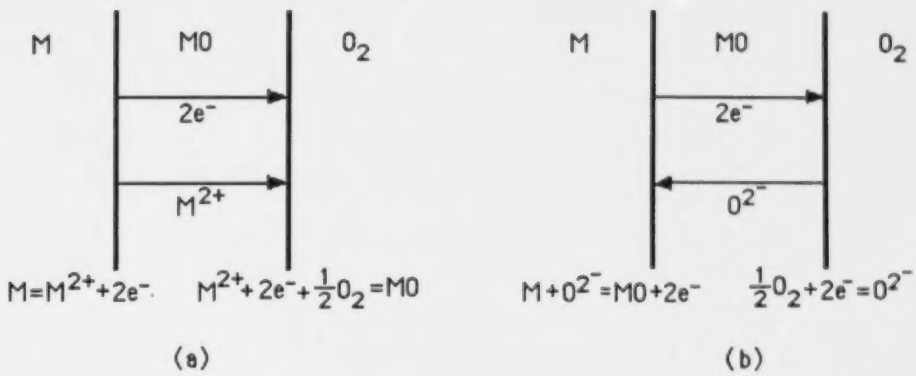

Figure 2-1: Interfacial reactions and transport processes for high temperature oxidation; a) cations mobile, and b) anions mobile [1].

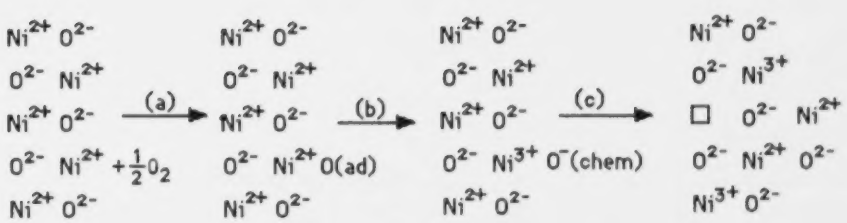

Step a) Adsorption: $\frac{1}{2}\,O_2(g) = O\ (ad)$

b) Chemisorption: $O\ (ad) = O^-(chem) + h^+$

c) Ionization: $O^-(chem) = NiO(s) + V^{2-} + h^+$

d) Overall Reaction $\frac{1}{2}\,O_2(g) = NiO(s) + V^{2-} + 2h^+$

Figure 2-2: Schematic representation of the formation of a metal deficit p-type semiconductor with cation vacancies and electron holes by incorporation of oxygen into the 'perfect' lattice [1].

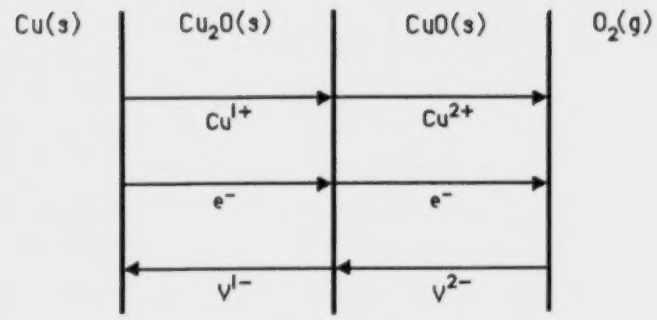

Figure 2-3: Schematic scale structure of a double oxide layer on the surface of copper [5].

Table 2-1: Parabolic rate constants for the oxidation of copper at various temperatures.

Temperature (°C)	Parabolic Rate Constant $x10^8$ ($g^2 \cdot cm^{-4} \cdot sec^{-1}$)[11]	Parabolic Rate Constant** $x10^8$ ($g^2 \cdot cm^{-4} \cdot sec^{-1}$) [31]
550	- -	0.117
600	**0.0153***	**0.145**
650	- -	0.191
700	**0.123**	**0.316**
750	0.285	0.525
800	**0.733**	1.175
850	**2.860**	2.82
900	4.130	4.00

* Extrapolated to 600°C.
* * Taken from graph.

Table 2-2: Comparison of copper oxidation results from two different researchers, Mrowec and Ananth et al.

	Ananth et al. [11]	Mrowec [10]
Year(s)	'80, '91	'70, '71
Activation Energy (kJ/mol)	166.7±10	100.4
$k_p \alpha P^{1/n}$	$\sim P^{1/7}$ Predicts singly charged vacancies	$\sim P^{1/4}$ Predicts neutrally charged vacancies
Temp. range (°C)	700 - 900	900 - 1100
Pressure range (Pa)	$2.5x10^3$ - $2.13x10^4$	$1.0x10^2$ - 8.1 $x10^4$

Table 2-3a: Copper oxide thicknesses for 850°C calculated from parabolic rate constants taken from [11,31].

850°C kp* (g^2/cm^4s) $2.86x10^{-8}$	kp (cm^2/s) $3.06x10^{-8}$	%CuO negligible	
Time (s)	$\Delta m^2/cm^4$ ($x10^{-6}$) (g^2/cm^2)	$\Delta m/cm^2$ (mg/cm^2)	Total oxide Thickness (μm)
120	3.40	1.85	27.1
300	8.60	2.93	43.8
600	17.2	4.14	61.6
900	25.7	5.07	74.2
1800	51.5	7.17	105
2700	77.2	8.79	128
3600	103.0	10.1	148

* Parabolic rate constant from Table 2-1 in **bold** was used.

Table 2-3b: Copper oxide thicknesses for 800°C calculated from parabolic rate constants taken from [11,31].

800°C kp (g^2/cm^4s) $7.33x10^{-9}$	kp (cm^2/s) $7.83x10^{-9}$	%CuO negligible	
Time (s)	$\Delta m^2/cm^4$ ($x10^{-6}$) (g^2/cm^2)	$\Delta m/cm^2$ (mg/cm^2)	Total oxide Thickness (μm)
120	0.880	0.938	13.7
300	2.19	1.48	21.7
600	4.41	2.10	30.6
900	6.60	2.57	37.6
1800	13.2	3.63	53.1
2700	19.8	4.45	65.0
3600	26.4	5.14	75.1

* Parabolic rate constant from Table 2-1 in **bold** was used.

Table 2-3c: Copper oxide thicknesses for 700°C calculated from parabolic rate constants taken from [11,31].

700°C k_p^* (g^2/cm^4s) 3.16×10^{-9}# 1.23×10^{-9}!	k_p^* (cm^2/s) 2.03×10^{-9} 7.89×10^{-10}	%CuO ~25.0		
Time (s)	$\Delta m^2/cm^4$ ($\times10^{-6}$) (g^2/cm^4)#	($\times10^{-6}$) (g^2/cm^4)!	Total oxide Thickness (μm)#	Total oxide Thickness (μm)!
120	0.380	0.148	7.33	4.57
300	0.948	0.369	11.6	7.20
600	1.90	0.738	16.4	10.2
900	2.84	1.11	20.1	12.5
1800	5.69	2.21	28.4	17.7
2700	8.53	3.32	34.8	21.7
3600	11.4	4.43	40.1	25.0

* Parabolic rate constants from Table 2-1 in **bold** were used.

Table 2-3d: Copper oxide thicknesses for 600°C calculated from parabolic rate constants taken from [11,31].

600°C k_p^* (g^2/cm^4s) 1.45×10^{-9}# 1.53×10^{-10}!	k_p^* (cm^2/s) 7.50×10^{-10} 7.90×10^{-11}	%CuO ~40.0		
Time (s)	$\Delta m^2/cm^4$ ($\times10^{-6}$) (g^2/cm^4)#	($\times10^{-6}$) (g^2/cm^4)!	Total oxide Thickness (μm)#	Total oxide Thickness (μm)!
120	0.17	0.0184	4.46	1.45
300	0.44	0.0459	7.06	2.29
600	0.87	0.0918	9.98	3.24
900	1.3	0.138	12.2	3.97
1800	2.6	0.275	17.2	5.62
2700	3.9	0.413	21.1	6.88
3600	5.2	0.551	24.4	7.94

* Parabolic rate constants from Table 2-1 in **bold** were used.

Table 2-4: Oxide to metal volume ratios of some common metals [29].

Oxide	Oxide-metal volume ratio
SiO_2	2.15
Al_2O_3	1.28
Cr_2O_3	2.07
CuO	1.72
Cu_2O	1.64
TiO_2	1.70
Ta_2O_5	2.50
Nb_2O_5	2.68
WO_3	3.30

Table 2-5: Linear coefficients of thermal expansion of some metals and oxides [29].

System	Oxide coefficient / K	Metal coefficient / K	Ratio
Cu/Cu_2O	4.3×10^{-6}	18.6×10^{-6}	4.32
Cu/CuO	9.3×10^{-6}	18.6×10^{-6}	2.00
Cr/Cr_2O_3	7.3×10^{-6}	9.5×10^{-6}	1.30
Co/CoO	15.0×10^{-6}	14.0×10^{-6}	0.93
$MoSi_2/CuO$	9.3×10^{-6}	$7\text{-}10 \times 10^{-6}$	0.75-1.08
$MoSi_2/Cu_2O$	4.3×10^{-6}	$7\text{-}10 \times 10^{-6}$	1.63-2.32

Chapter 3
Diffusion Barriers

In an attempt to passivate copper the literature search has led to three main areas of study. The first was oxidation theory and its relevance to copper oxidation. This was discussed in Chapter 2. The next two, which are topics of this chapter, are thick film hybrids and diffusion barriers in VLSI technology. The information from these two areas were used to assist in the selection of the materials and methods used for passivating copper.

3.1 The Thick Film Approach

In hybrid electronic technology, thick film copper conductor pastes are an alternative to precious metal pastes. The major problem with using copper pastes is that copper oxidizes rapidly in oxygen at high temperatures. If copper is to be used as a thick film conductor, then methods of firing the paste need to be found in order to prevent its oxidation. To date, there have been a number of attempts at using copper as a thick film conductor. The first method which has been used successfully replaces the oxygen atmosphere with nitrogen using a nitrogen furnace. The second method, which has had limited success, uses a sacrificial material which preferentially oxidizes instead of copper.

3.1.1 Nitrogen Furnace Solution

The first attempts to use copper for thick film pastes employed nitrogen furnaces in order to prevent copper from oxidizing. Nitrogen furnaces are used to keep the oxygen partial pressure, at 850°C, below ~7 ppm. This solved the problem of preventing the copper from oxidizing, but it caused other problems, such as; incomplete

burnout of organics from the paste material, and incompatibility between the nitrogen atmosphere and other resistive and capacitive components on the circuit board. However, much research has been done to advance the nitrogen furnace approach. A recent study [32] showed that nitrogen firable pastes are, or are rapidly, approaching the performance criteria established for air fired materials. Nitrogen firable pastes, resistor systems, and various other components have been developed along with the nitrogen furnace demands of a) time-temperature uniformity, b) the flushing action of the atmosphere, and c) the cleanliness of the processing environment [33].

However, in an attempt to reduce the added cost of expensive nitrogen furnaces, a continuous flow of gas, and the development of all the other nitrogen compatible components, other attempts to prevent copper from oxidizing are necessary. The ideal situation would be to fire inexpensive copper thick film pastes in air, and retain the use of most of the other materials and processes currently employed in the thick film industry.

3.1.2 Steel Vessel Solution

Copper paste can be fired in air with an attachment of a low carbon steel vessel with small holes using a conventional conveyor belt furnace [34]. The principle of this method exploits the difference in heat of formation between copper oxide and iron oxide. During firing at 700-900°C, iron oxide is formed preferentially because of the larger negative heat of formation compared with copper oxide, as shown by the following equations:

$$Cu + \frac{1}{2}O_2 = CuO \qquad \Delta H = -155 \text{ kJ/mol}$$

$$2Cu + \frac{1}{2}O_2 = Cu_2O \qquad \Delta H = -167 \text{ kJ/mol}$$

$$3Fe + 2O_2 = Fe_3O_4 \qquad \Delta H = -1096 \text{ kJ/mol} \qquad [34].$$

The formation of iron oxide can prevent the oxidation of copper because the atmosphere in the vessel is expected to be inert or reductive. The reason for the small holes in the top of the carbon steel vessel is to allow the decomposed gas of the organic vehicle contained in the printed paste to escape during the drying and firing processes.

There are a number of drawbacks to this method. It is important to maintain a non-reducing atmosphere when firing thick film copper multilayers, because when processed under reducing conditions electrical shorts can develop. Reducing conditions during firing are caused by incomplete burnout of organics from the thick film compositions. Also, a reducing atmosphere induced in the vessel can alter the function of other components on the hybrid circuit board. For example, this technique gives poor compatibility with commercial resistors based on noble metal oxides (ruthenium oxide or palladium oxide).

The low carbon steel vessel produced acceptable copper paste properties. The sheet resistivity of the fired copper used, CERMalloy 7029 nitrogen firing copper conductor, was in the range 2-3 mΩ/sq (normalizing to a 25.4 μm (1mil) thickness, gives a resistance value of 5.1-7.6 μΩ-cm) when fired from 750 to 900°C, for a total firing time of 40 minutes. Peel strength increased with increasing firing temperature, and solderability was excellent after some burnishing. The electrical and mechanical properties of fired copper conductor are about the same as that of nitrogen fired conductor. However, since the inner atmosphere of the low carbon steel vessel is reductive, this firing process is limited and causes problems for the other components on the hybrid circuit board.

3.1.3 Boron Solution

Boron has been successfully applied to base metal (nickel, cobalt and copper) thick film pastes to prevent their oxidizing when fired in air. The reason boron works is that it is a strong reducing agent. Boron powder fired in air becomes boron oxide. Two techniques have been used. The first generation paste incorporated boron into the copper paste [35], and the second generation system used boron as a coating over the surface of the copper paste [36].

The first generation boron air firable base metal conductor incorporated a boron powder with a base metal powder, so that any oxidized or unreacted boron remained in the fired films, (Figure 3-1). This technique causes problems for any soldering afterwards. A heavy layer of boron oxide is present on the surface of the conductor film and in order to become solderable, the surface has to be treated either by mechanical burnishing or by chemical etching.

The second generation applied the copper and boron layers in steps, (Figure 3-2). The copper paste is printed onto a substrate. The thick film is dried and the entire substrate is covered with a coating of boron paste which is then dried a second time. It is then fired in air at a temperature from 600°C to 850°C to sinter the glass frit and bond the copper powder together onto the substrate. The coated layer of boron, where continuous with the copper printing, is fused as a protective layer. This allows the copper to sinter and to bond with the substrate without oxidation of the copper. Oxidized boron covering portions of the substrate which are not occupied by the thick film and are not superposing the copper layer, is then washed away, as boron oxide is soluble in hot water. The boron bonded to the copper remains as a protective coating.

The effect of the boron coating on the copper film is equivalent to an inert or reducing atmosphere upon firing. Another advantage of the second generation boron method is solderability. The resulting copper surface is readily solderable without further treatment. As compared with silver bearing thick film conductors, copper conductors yield a high conductivity, more resistant to solder leaching and almost no cation migration. Compared with the first generation of air fired copper conductors, the second generation is much less sensitive to humidity and offers much better aging characteristics. No special furnace is required and no nitrogen or hydrogen is needed. Ordinary air fired ovens can be used and the copper can be readily soldered without further treatment.

3.2 The Diffusion Barrier Approach

The ideal diffusion barrier physically separates materials A and B, with a material X, so that under processing and operating conditions the undesirable mixing of materials is suppressed. Ideally the diffusion barrier should meet many requirements [37]:

1) The transport of A and B should be negligible.
2) The loss of material X into A and B should be negligible.
3) Contact resistances should be small.
4) Adhesion between materials should be strong.
5) X should be thermodynamically stable against A and B.
6) X should be of uniform thickness and structure.
7) X should be highly thermally and electrically conducting.
8) The process should be inexpensive.

In practice additional constraints may be imposed due to processing. Often it is easier to outline how a barrier material should not be made than on how it should. Over the past 20 to 30 years, knowledge has grown in the understanding of atomic migration and reaction in thin films but it is somewhat fragmented and empirical. However, there are certain major facts and trends for thin film diffusion barriers which are understood. These are discussed below.

3.2.1 Diffusion Barriers - Basic Theory

The driving force for atomic motion is the chemical potential gradient of the atoms. A chemical gradient can be caused by a concentration gradient, a negative free energy of reaction, an electric field, or a strain gradient. For the purpose of this paper, the first two are of primary importance.

Structural defects can affect the diffusion rate of atoms in thin films. The diffusion of atoms occurs fastest at free surfaces. Diffusion along grain boundaries and dislocations is intermediate and diffusion in the interior of crystals (lattice diffusion) is slowest for thin films. Each of these processes has a different activation energy. As early as 1935, DuMond and Youtz [38] observed something fundamental about 'low' temperature diffusion. For temperatures less than about $0.6T_m$, the diffusion in a polycrystal solid phase is many orders of magnitude faster than if high temperature data is extrapolated down to low temperatures. This has significance for thin film diffusion barriers. In a polycrystalline thin film, lattice diffusion is dominant at high temperatures but at low temperatures grain boundary diffusion is dominant. A crossover from one diffusion process to the other is expected as the temperature changes. The crossover temperature is called the Tammann temperature which is one-half to three-fourths the absolute melting temperature.

The explanation for low temperature defect diffusion dominance is as follows. It is well established that an atom can more readily make a successful jump from one location to the next at dislocations, boundaries or surfaces than that of the same atom in the lattice [39]. The diffusivity is therefore higher in these regions. Since the grain boundaries represent a small part of the cross-sectional area, they contribute only a small percentage of the diffusing atoms. Since each of these processes has a different activation energy, this results in a different temperature behaviour for the various

processes. The activation energy is lower for defect diffusion, thus as the temperature decreases the effect becomes progressively more important. Therefore, because the diffusivities are exponentially dependent on temperature, at low temperatures the difference between lattice diffusion and defect diffusion becomes significant. Hence a 'short circuit path' is set up for the diffusing atoms. Figure 3-3 illustrates this concept with an example for the self diffusion of silver for single crystal and polycrystalline samples. The polycrystalline sample has the same diffusivity values as the single crystalline sample at high temperatures, but as the temperature decreases the diffusivity of the polycrystalline sample is higher because defect diffusion becomes dominant. Therefore, even if a diffusion barrier can be found such that it has a negligible solubility with materials A and B, it may fail in the form of a thin film due to structural defects at low temperatures. Using this logic it would be desirable to have a single crystal barrier layer, which is not practical or possible in many applications. The next best alternative is then to have a large grained polycrystalline barrier. Another option is an amorphous thin film diffusion barrier which behaves in a manner intermediate to lattice and grain boundary diffusion [40]. However, the diffusion mechanism in amorphous materials is not understood very well.

Diffusion barriers do not eliminate the driving force for diffusion, they reduce the rate of interdiffusion by presenting a region of reduced mobility for atomic migration. Thus the usefulness of the diffusion barrier can be measured by how well it reduces the mass transport through the diffusion paths present [41].

There are many cases where the bulk solubilities of A and B are nil, but intermixing can be found as grain boundary decoration. For instance, consider a diffusion couple of copper and lead, which are mutually immiscible in their bulk solid phases and do not form compounds [42]. After an anneal in argon, copper can be found in lead if the lead grains are significantly smaller. The reverse situation can be created, where there is lead in copper, if the copper grains are significantly smaller than lead. The grain size, other structural characteristics such as defects, the texture and the stress generally depend on the method of fabrication of the thin film [37]. For diffusion barriers this means that the procedures applied in the fabrication process can be a critical factor in the success or failure of a diffusion barrier.

3.2.2 Types of Barriers

There are various types of diffusion barriers used for VLSI technology. A brief description of each is given below and some examples of barriers are used to illustrate points.

Sacrificial barriers

Thermodynamically, for a potential reaction to take place at a given temperature, it must have a negative Gibbs free energy change for the reaction, where the change in Gibbs free energy (ΔG) is defined by equation 1:

$$\Delta G = \Delta H - T\Delta S \qquad (1)$$

ΔH is the change in enthalpy and ΔS is the change in entropy. For solid state reactions ΔS is small and the reaction is thus determined primarily from ΔH. Figure 3-4 illustrates the concept of the sacrificial barrier. The metal X can react with both A and B. If the reactions with both A and B are laterally uniform and fully characterized (i.e., which compounds form, the rates of reactions and the activation energies), then it becomes straightforward to predict how long it will take at any given temperature for the barrier X to be fully consumed. A number of successful sacrificial barriers have been used between aluminum and silicon [43]. Titanium and vanadium are two examples. When an aluminum layer is deposited on a film of polycrystalline silicon, the resulting bilayer is unstable. Aluminum and silicon do not form compounds and their eutectic temperature is 577°C. Aluminum diffuses through polysilicon at 150°C and a thin film couple of aluminum and silicon becomes structurally unstable around this temperature. However, titanium is a good diffusion barrier between aluminum and silicon. At 450°C titanium reacts negligibly with silicon but it forms $TiAl_3$ with aluminum. As long as some unreacted titanium remains, the contact retains its structural integrity. Since aluminum reacts 20 times slower with vanadium than with titanium, the same protective action is offered with less vanadium.

Sinks (and Solid Solutions)

The presence of a sink at the boundary of a film which contains rapidly diffusing impurity atoms constitutes a strong driving force in thin film couples [37]. In the case where material A forms a solid solution with material B, the presence of a sink (S) can affect the final outcome of an experiment. Without the sink present, the diffusion

couple, when annealed at a suitable temperature, will form a solid solution. However, with the sink present, say on the top layer (for material stack, A/B/S), it is possible for a compound AS to form which removes A atoms from the grain boundaries of B at a much faster rate than does the process of diffusion into the grains of B. The presence of the sink prevents the solid solution from forming [44,45].

Sinks can affect the behavior of thin metal layers significantly. Figure 3-5 illustrates this point. A polycrystalline gold film is deposited onto single crystal silicon [46,47,48]. Silicon and gold below the 370°C eutectic temperature are mutually insoluble. In a vacuum or a forming gas, negligible amounts of SiO_2 are formed on the surface of the Si/Au diffusion couple at 300°C. As low as 100°C in air, SiO_2 will grow rapidly on the surface of the gold film. The oxidizing ambient acts as a sink for the silicon atoms.

Compound Barriers

The number of compound barriers to choose from is large and therefore they offer a large selection of properties. It is this wide selection of compounds that poses a problem; that is, the choice of the right barrier for the job. In practice, the solutions adopted for a given problem have been arrived at empirically, because most of the data needed to make decisions on logical grounds is not available. For example, the bulk material properties generally deviate from thin film properties, where thin film conditions of stress and structure differ from those of bulk materials. Thermodynamic data and diffusivity data are not available for many of the compounds. More data needs to be collected if a complete characterization of materials is to be had.

Diffusion barriers based on oxides are generally not suitable if electrical conduction is desirable, because they are usually insulators. However, electrical current can pass through an insulator if that layer is thin enough for electrons to tunnel. This is possible only for very thin barriers. However, with very thin layers of the order of tens of nanometres there is the added problem of reproducibility and uniformity without pinholes. One study has observed that layers of SiO_2, between 20nm and 200nm thick, grown thermally on single crystal silicon wafers, are permeable to gold [49]. The oxide films were covered with dots of evaporated gold 50nm thick and heated at 500°C for 4-16 hours in a dynamic vacuum of about 10^{-6} torr. A deterioration is observed at localized points. At these points gold seeps through the oxide and forms slowly, spreading patches of Au-Si eutectic along the SiO_2-Si interface. It was found

that the diffusion rate is dependent on the partial pressure of oxygen in the vacuum. The phenomenon does not occur in other atmospheres such as air, helium or encapsulated vacuum. It is possible that films of other metals on ultra thin SiO_2 layers are stable or that insulating layers other than SiO_2 may be useful as barriers. This will not be known until careful experiments are carried out, which may depend on the film deposition technique.

Chemical compounds such as transiton metal nitrides, carbides, borides and silicides are strongly bonded compounds with large negative heats of formation (ΔH) and high melting points. They generally have low resistivities and have been applied in VLSI technology as diffusion barriers in various atmospheres. These materials seem to be the best compounds for the job of diffusion barriers [37].

Impurities and Stuffed Barriers

This type of diffusion barrier is the least understood and there is only experimental evidence at the present time. If impurities are used to try to stuff the fast diffusion paths (defects) then a material may be a good barrier (see Figure 3-6). Impurities can be a) an interfacial layer, b) co-deposited contaminants in the as-deposited films or, c) impurities from external sources such as an annealing environment [50]. Impurities can affect, among other things, electrical properties and the stability of films. Oxygen contamination has a large influence, both as a contaminant in films and as the oxide layer at the interface and grain boundaries. One example of oxygen contamination is a Ti/Mo/Au metallization [51]. If the layers are deposited using a good vacuum, titanium diffuses through the molybdenum layer to react with gold. However, if the vacuum is broken before the deposition of the molybdenum layer, then no diffusion occurs at similar processing temperatures. How the diffusion is prevented is not clear but if pure layers are used the molybdenum diffusion barrier layer will not work. The distinction between a stuffed barrier and a compound barrier is not a sharp one.

3.3 Silicides

Silicides have been the topic of many papers. A substantial amount of data has been collected regarding resisivities, heats of formation, oxidation and various other data related to VLSI technology. The following section is a discussion of the various

properties regarding silicides. Although silicides have been deposited onto silicon or silicon dioxide, there is still relevant information available.

A number of oxidation studies have been done on the transition metal silicides, i.e., $CoSi_2$ [52,53], $NiSi_2$ [54], PtSi [52], and the refractory metal silicides, i.e., $TiSi_2$ [55], $HfSi_2$ [56], $TaSi_2$ [57], $MoSi_2$ [58,59], and WSi_2 [51,60,61]. Oxidizing conditions are at elevated temperatures, so only the most silicon rich oxides have been studied. The reason, in part, is that the silicides richest in silicon are the most stable. The oxidizing atmospheres are either classified as wet or dry oxygen, but a strict quantification of the gaseous species has not been done by researchers. The important point to note is that silicon is sensitive to water vapour in amounts <1%, and Murarka [62] hypothesized that silicides may behave in a similar way. Another important point is that silicides have different properties depending on the method of preparation [51], so diffusion and oxidation rates can vary for the same material depending on the type of preparation. One example of this phenomenon is WSi_2 [61] . WSi_2 was shown to behave differently depending whether it was prepared by rf sputtering of hot pressed targets or by coevaporation. The former disintegrated when annealed in wet oxygen at 1000°C while the latter formed an SiO_2 layer at the surface and maintained its integrity and stoichiometry after being annealed in steam at 900-1100°C. This point will be discussed later. Another example of how properties can vary depending on the method of preparation is $TaSi_2$, but this case will also be discussed later.

3.3.1 Transition Metal Silicide Stability

To determine what makes one silicide more stable than another in oxidizing ambients, Murarka [50,63] has looked at the oxide to metal volume ratio, oxide melting points, oxygen solubility in silicides, and the heats of formation of oxides. One important point to note is that without exception, silicon rich silicides have more negative heats of formation per metal atom than do the lower silicides of the same metal.

The oxide to metal volume ratio is given for the refractory metals in Figure 3-7 [63]. During the oxidation of a silicide, groups 4A and 5A oxidize with volume changes very close to that of silicon (except for V). Group 6A metals oxidize with a much higher volume expansion than that of silicon which leads to significantly larger accommodating stresses during the oxidation of the silicides. The melting points for oxygen rich

refractory metals are given in Figure 3-8. Melting points decrease as the group number increases within the same period. V, Cr, and Mo have oxide melting points below 1000°C and MoO_3 and WO_3 are volatile. The heats of formation of transition metal oxides are given in Figure 3-9. Most elements form more than one oxide, but there is a similarity in behaviour of the oxides of the same element because the heats of formation per oxygen atom do not vary significantly (except for Cr). The heats of formation decrease with increasing oxygen content of the oxide. Oxygen rich oxides are generally formed in the presence of an oxidizing medium and at the elevated temperatures [50]. Figure 3-9 shows that WSi_2 and $MoSi_2$ are more stable when silicon is available for oxidation and that Ti, Zr, and Hf disilicides may decompose during oxidation. Property data is given in Table 3-1 for silicon rich refractory metal silicides and their oxygen rich oxides.

Considering the above three concepts, Murarka believes that when subjected to oxidizing conditions group 4A and 5A are somewhat more stable than group 6A disilicides [50]. This contradicts some of the other reported findings of $MoSi_2$ and WSi_2. However, it is recognized that SiO_2 forms on the surface of $MoSi_2$ and WSi_2 to give them their stability.

3.3.2 Empirical Data

The following is a summary of the results from a number of experimental studies on the oxidation of silicides. The silicides were oxidized in dry oxidizing ambients and were either deposited on silicon or SiO_2.

$MoSi_2$ and WSi_2 on silicon leads to an initial loss of metal in the form of MoO_3 or WO_3 [58,59,64-66], and SiO_2 forms a capping layer on the surface. As oxidation continues, the SiO_2 layer continues to grow and thus the silicon to metal ratio in the silicide decreases with time, allowing lower silicides to form. $MoSi_2$ and WSi_2 on SiO_2 decompose during oxidation, leading to metal rich silicides, metal in the film, and loss of metal as volatile WO_3 or MoO_3. It is noteworthy that these oxidizing times were in the range of 1 to 2 hours at 800 to 1000°C.

$TaSi_2$ is an interesting case. Depending on the type of silicide film preparation used, the oxidation characteristics vary at 900 and 1050°C. Sintering tantalum on

polysilicon results in no oxidation except for the formation of a thin (<10nm) oxide layer on the surface [57]. For cosputtered $TaSi_2$ on polysilicon, SiO_2 grows on the surface as long as there is available silicon present. Murarka hypothesizes that these differences for $TaSi_2$ could be due to the following reasons [50]: a) the silicon/tantalum ratios may be different; b) the metal and/or silicon concentration gradient at the silicon-silicide interface is abrupt for the cosputtered film (an abrupt concentration gradient increases the diffusion rates); c) the transport mechanisms may be different. For cosputtered silicides with small grain sizes, silicon can be expected to diffuse quickly to the surface so the rate limiting step is the slower oxygen diffusion through the growing oxide layer. For the reacted silicide, the silicon transport across the silicide grains is slow and controls the oxidation rate. At 1000°C, half the $TaSi_2$ melting point, diffusion can be very slow.

Murarka and Chang [56] have shown that $HfSi_2$ is not stable during oxidation. At temperatures of 400°C, hafnium preferentially oxidizes leaving silicon behind. At 700°C, for 20 minutes of dry oxidation, all the hafnium oxidizes leaving the silicon in the silicide unoxidized.

3.3.3 Oxidation Mechanisms

It has been reported by many researchers [50,52,55-59,65-67], that the oxidation of silicides on silicon or polysilicon proceeds by silicon diffusion through the silicide to the top surface and then oxidation to form SiO_2. As the SiO_2 layer grows, the oxygen diffuses through the silicon dioxide. This is similar to the case of a sink. The equation many of the researchers use for modeling the oxidation of a silicide on silicon is similar to the equation for silicon [68]:

$$x^2 + Ax = B(t + \tau)$$

or

$$x^2 = B(t + \tau)$$

- x is the oxide thickness
- t is the oxidation time
- B is the parabolic rate constant
- B/A is the linear rate constant
- τ is a time coordinate correction for the presence of an initial oxide thickness.

Murarka et al. [57] have studied the oxidation of silicides on silicon and have proposed the following based on thermodynamic and kinetic arguments. The energetically favourable process is the one where silicon diffuses through the silicide to the surface and forms SiO_2. This is the case reported above. However, initially, a thin layer of silicide may decompose to provide silicon atoms for oxidation. The free metal atoms then form a very thin metal oxide on the surface; this has been verified for $CoSi_2$ [53], $TaSi_2$ [57], and $TiSi_2$[55]. For WSi_2 and $MoSi_2$ [58,66], WO_3 and MoO_3 form and vaporize. $HfSi_2$, which has a very low negative metal oxide formation energy compared with SiO_2, continues to decompose during oxidation. Table 3-2 shows the kinetics of oxidation for various silicides in a dry oxidizing ambient.

Looking at the activation energies for the parabolic rate constants of Allessandrini et al. shown in Table 3-2, Murarka has noted [50] that the values for the various silicides are somewhat higher than for silicon. The rate at which silicon becomes available at the SiO_2-silicide interface is the rate controlling process. An activation energy between 1.24-1.6 eV suggests that silicon is diffusing through the silicide by a substitutional mechanism. $CoSi_2$ [52,53], and PtSi [53] have been demonstrated to exhibit substitutional diffusion of silicon through their silicides. For $TiSi_2$ [55], however, a radioactive tracer technique was used to show that the diffusion occurred by a fast diffusing mechanism such as a grain boundary, dislocation or an interstitial diffusion mechanism. For $NiSi_2$ [54], it was shown that the oxide growth rates were independent of the film thickness, structure and the stoichiometry. This suggests the oxidation rate limiting step was through the SiO_2 layer.

For all cases studied of a silicide on SiO_2, the silicide decomposes to produce SiO_2 and a metal rich silicide. With continued oxidation, the silicide will decompose to form additional SiO_2 and a metal oxide. Sinha [60] has shown that cosputtered WSi and WSi_2 on SiO_2 can decompose catastrophically at 1000^{o}C in a pest reaction, (a further discussion of pest behaviour will be discussed later). This is contrary to some of the other findings for cosputtered WSi_2, but it is noted that the method of preparation is an important factor in the film behaviour. The silicide locally lifts off the substrate and a volatile compound (probably WO_3) forms hillocks on the surface of the film. This is probably due to a combination of compressive film stresses upon annealing and the volatile nature of the oxide. $TiSi_2$ films also develop compressive stresses, but do not exhibit a pest reaction.

3.3.4 Molybdenum Silicide

Properties of Bulk $MoSi_2$ and $MoSi_2$ Coatings

Recently an extensive survey of progress in the area of high temperature silicides has been published [69], with an emphasis on $MoSi_2$. Potential silicides for elevated temperature applications are those based on refractory and transition metals. Of these materials, $MoSi_2$ has a good combination of high melting point, good high temperature oxidation resistance, and low electrical resistivity. Molybdenum silicide exhibits a combination of ceramic and metal properties. Its bonding is a mixture of covalent and metallic type. Molybdenum disilicide is known to exist in two different crystal structures: a hexagonal (metastable) structure with lattice parameters of a=0.46nm and c=0.66nm, and a tetragonal structure, with lattice parameters of a=0.32nm and c=0.785nm. The thermal expansion coefficient of $MoSi_2$ is $7\text{-}10 \times 10^{-6}/^{o}C$ in the range of 20°C to 1400°C and its thermal conductivity is 65 W/mK at room temperature and decreases to 30 W/mK at 1400°C [70].

The phase transformations in thin film $MoSi_2$ produced by sputter deposition have been studied by Chou and Nieh [71]. 50 nm of $MoSi_2$ were deposited by d.c. magnetron sputtering from a hot-pressed $MoSi_2$ target. The as deposited films were amorphous. Annealing the amorphous films at elevated temperatures induced crystallization. Annealing temperatures ranged from 300°C to 900°C with the shortest annealing time being 2 hours. Films annealed between 300°C and 800°C transformed to needle-like hexagonal $MoSi_2$ crystallites. Partial phase transformation of the $MoSi_2$ from hexagonal to tetragonal structures occurred in the films annealed at 800°C. Anneals at 900°C gave rise to the formation of thermodynamically stable tetragonal $MoSi_2$ with equiaxed granular morphology.

Bulk molybdenum silicide has good high temperature oxidation resistance. It forms a protective, adherent, and coherent silica layer at high temperatures. Maximum oxidation rates actually occur at intermediate temperatures in the range of 375-550°C, where oxidation pesting can take place. 'Pest' behavior can be minimized by the addition of $MoGe_2$, which alters the viscosity and thermal expansion coefficient of the oxidation layer [72]. Pesting will be discussed in more detail in the next section. Bulk $MoSi_2$ has been alloyed with other high melting point silicides as a means of improving its mechanical properties [73]. It has been shown that solid solution alloying with WSi_2 improves high temperature mechanical properties [74]. Although the mechanical

properties can be improved by alloying, it is noteworthy that all other disilicides and trisilicides have an oxidation resistance inferior to $MoSi_2$.

$MoSi_2$ has been applied as high temperature coatings for refractory metals, and for carbon structural materials which require coatings for elevated temperature oxidizing conditions. The important factors for coatings of this type include oxidation resistance, thermal stability and strength, high temperature chemical compatibility between coating and substrate, and low thermal expansion coefficient mismatch between coating and substrate. One example is a $(M,W)(Si,Ge)_2$ coating for niobium [75]. The germanium additions improve cyclic oxidation resistance, while the tungsten additions improve high temperature coating strength. Niobium samples can survive 200 one-hour cycles at 1370°C in air and 60 one-hour cycles at 1540°C in air, due to the formation of a protective glassy film.

$MoSi_2$ is unique among the refractory silicides in that the volatilization of the molybdenum oxides species and formation of a continuous protective silica film is observed in air from temperatures as low as 600°C [76]. The ability of $MoSi_2$ to form and maintain a protective silica film over a wide temperature range led to an extensive research effort by researchers for coatings for protection of refractory metals, graphite, nickel and niobium alloys [75,77]

Oxidation Behaviour of $MoSi_2$

High temperature oxidation of $MoSi_2$ has been extensively studied. It is known that the excellent oxidation resistance of $MoSi_2$ is a result of the formation of a self passivating glassy silica (SiO_2) surface layer, which protects the substrate from further attack by oxygen. However, the protection deteriorates at temperatures above 1800°C when oxygen diffusion through the SiO_2 layer increases drastically, and the formation of volatile SiO becomes dominant through the reaction of SiO_2 with silicon. At low temperatures, within a specific temperature range (375°C-500°C), the oxidation of $MoSi_2$ leads to structural disintegration. This phenomenon was referred to as 'pesting' when it was first discovered by Fitzer in 1955 [78]. Since then pesting has been observed in other silicides, aluminides and berylimides. Between the temperatures of 500 - 550°C, a transition from nonselective oxidation to selective oxidation of silicon to form protective SiO_2 occurs.

Between the temperature range 375 - 500°C, $MoSi_2$ fails catastrophically due to a pest reaction [79]. Pest reaction of $MoSi_2$ gives rise to powdery products which totally disintegrate the structural integrity of the sample. Experimental results of hot pressed polycrystalline samples show that the pest reaction products of MoO_3 and SiO_2 form heterogeneously and in a loosely packed fashion. For a severely pested sample the pested region contains a mixture of MoO_3 whiskers (or platelets) and SiO_2 clusters. In polycrystalline samples, SiO_2 clusters initially form at cracks and interparticle boundaries, and protruding from these are MoO_3 whiskers. Also present are residual $MoSi_2$ particles in the pested volume. The residual $MoSi_2$ particles are coated with a thin layer of Si-Mo-O surface oxide and are considered to be in a metastable state that evolves into the thermodynamically stable products of MoO_3 and SiO_2.

The pest reaction is most vigorous at 500°C, and is characterized by a lengthy nucleation period followed by a relatively fast growth period. Arc melted polycrystals exhibited the same pest characteristics as hot pressed powder metallurgy samples. Single crystal samples also exhibit similar pest characteristics but at much slower rates than the polycrystalline counterparts. Although a thin Si-Mo-O surface oxide forms within a few hours, for single crystal samples, the initial stages of pesting do not begin until after 50 hours have elapsed. Disintegration of the single crystal sample occurrs at times greater than 1000 hours. Thin films of $MoSi_2$, 1.2 μm thick, also exhibit pest disintegration at 500°C for 5 to 20 hours, however, they begin to crack after a short period of 5 minutes of oxidation.

There are five oxides of molybdenum, but at standard pressure there exist two possible oxidation reactions, a high temperature and a low temperature reaction [80];

$$2MoSi_2(s) + 7O_2(g) = 2MoO_3(s) + 4SiO_2(s) \qquad \text{low temp} \qquad \ldots (1)$$

$$5MoSi_2(s) + 7O_2(g) = Mo_5Si_3(s) + 7SiO_2(s) \qquad \text{high temp} \qquad \ldots (2)$$

Both have negative free energies of reaction, but experimentally the presence of MoO_3 whiskers and SiO_2 clusters between 375 - 500°C indicate that Equation 1 is dominant at these temperatures. The temperature dependent oxide morphology was attributed to a) competing kinetics among interdiffusion rates of Mo, Si, and O, b) the nucleation/growth of stable MoO_3 and SiO_3, and c) the evaporation of MoO_3.

Figure 3-10 illustrates the evolution of the reaction products for single crystal $MoSi_2$ during various stages of volume diffusion as proposed by Chou and Nieh [81]. The inward diffusion of oxygen gives rise to a transient diffusion zone (Figure 3-10a) and a surface Si-Mo-O oxide layer (Figure 3-10b). MoO_3 evaporates leaving behind an SiO_2 layer with little or no molybdenum (designated as SiO_2(Mo), Figure 3-10c). As a result, substantial internal stresses develop in three different ways: 1) molar volume expansion by oxidation; 2) differential thermal expansion between the Si-Mo-O oxide and the $MoSi_2$ substrate, and 3) the vapour pressure caused by the volatilization of MoO_3. As the MoO_3 starts to evaporate, molybdenum is locally depleted from the surface layer. Blisters form in regions with lower molybdenum concentrations. Therefore, the evaporation of MoO_3 is believed to serve as the driving force for the initial nucleation of the blisters (Figure 3-10c). The major contributing sources for blister formation result from the other two types of stress generation, namely 1) the molar volume expansion by oxidation, and 2) the differential thermal expansion stresses. As oxidation continues, the blisters break open (Figure 3-10d). The thermodynamically stable MoO_3 and SiO_2 mixed oxides form, but these are loosely packed and offer poor oxidation protection to the $MoSi_2$ substrate (Figure 3-10e). Therefore, the oxidation of the $MoSi_2$ leads to gradual surface recession and complete disintegration of the sample at pest temperatures.

For polycrystalline samples, the pest of $MoSi_2$ also involves grain boundary diffusion of oxygen. It has been demonstrated that unpested areas show the formation of a thin Si-Mo-O surface layer, with an interior that has already undergone pest reaction particularly at the grain boundaries. Therefore the inward diffusion of oxygen along grain boundaries is relatively fast. This leads to the internal formation of MoO_3 and SiO_2, and because the internal stresses are substantial, cracking and disintegration occurs.

When comparing the single crystal pest reaction with the polycrystalline samples, the single crystalline $MoSi_2$ takes significantly longer to disintegrate. Therefore, interfaces and structural imperfections are believed to serve as favourable sites for pest reaction. Two major kinetic processes are involved in the pest of $MoSi_2$: volume diffusion of oxygen and grain boundary diffusion of oxygen. For single crystalline $MoSi_2$, volume diffusion is the only process that takes place. The initial transient Si-Mo-O oxide subsequently converts into loosely packed MoO_3 and SiO_2, that offer no surface protection and eventually lead to surface recession. In polycrystals, the

more rapid kinetic process of grain boundary diffusion also takes place, causing MoO_3 and SiO_2 to form at grain boundaries leading to much faster pesting rates.

From cyclic oxidation data in the temperature range of (400-600°C) Meschter [82] determined the activation energy of the pest reaction of polycrystalline $MoSi_2$ to be about 116 kJ/mol. High temperature (above 900°C) oxidation of $MoSi_2$ has an activation energy of about 335 kJ/mol [83]. Chou and Nieh [84,85] suggest these are in good agreement with their results. The rate limiting step for high temperature oxidation of $MoSi_2$ is the oxygen diffusion through the self-passivating silica layer. But in the case of the pest reaction which occurs primarily at low temperatures, polycrystalline samples exhibit grain-boundary/interface diffusion of oxygen as the primary contributing mechanism.

3.4 Borides, Nitrides, and Carbides

Most nitrides and carbides are metallic conductors with room-temperature resistivities (ρ) in the range of 7-250 $\mu\Omega$-cm. Most of the earlier carbide and nitride samples, used for electrical resistivity measurements, have been prepared by powder metallurgy techniques. Their high melting points and relatively slow diffusion rates make the preparation of fully dense compacts difficult. Also, other factors will affect the resistivity measurements. These include different nonmetal to metal ratios for supposedly the same reported composition (usually stoichiometric) and differing amounts of impurities, particularly other interstitial elements such as oxygen. Deviations from stoichiometry rapidly increase the resistivity in TaC_{1-x} and TiC_{1-x} [86,87,88]. There is an increase in resistivity with increasing carbon content. It is uncertain exactly what factors are responsible for these increases. Also impurities such as oxygen would be ionically charged in the lattice and would effectively scatter electrons. It is especially difficult to obtain group IV nonstoichiometric carbides and nitrides free from oxygen contamination, due to the tremendous chemical affinity of this group for oxygen. The presence of oxygen in TiC samples could be responsible for part of the increase in resistivity with stoichiometry deviations.

Transition metal carbides and nitrides have very high melting points. Several carbides and nitrides melt or decompose above 3000°C and TaC has one of the highest melting points known (~3980°C). The melting points of the carbides are generally

higher than those of the parent transition metal elements, whereas the melting or decomposition temperatures of many nitrides are comparable to those of the pure transition metal elements. Of the transition metals, group 6A elements have the highest melting points. For the carbides the maximum is in group 5A, and for the nitrides, group 4A metals have the highest decomposition temperatures. All the refractory nitrides and carbides are stable at room temperature, except for VC which is slowly attacked by air at room temperature. At high temperatures they oxidize readily to form oxides [89]. Both their chemical reactivity and thermodynamical properties are sensitive functions of the nonmetal to metal ratio. Table 3-3 gives the bulk properties of the refractory metal carbides and nitrides.

3.4.1 Empirical Data

Shappirio and Finnegan [93] have prepared and characterized thin films of two of the lowest resistivity diborides as tabulated by Nicolet, namely ZrB_2 and TiB_2. Thin films, up to 800 nm in thickness, were deposited by sputtering onto silicon, or thermal SiO_2 on silicon, and annealed in order to optimize the properties of the as deposited films. RBS and XRD data showed that the films contained up to 6 wt% O and 12 wt% O for ZrB_2 and TiB_2 respectively, but showed the as deposited ZrB_2 and TiB_2 films were stoichiometric. The properties of the thin film ZrB_2 and TiB_2 are given in Table 3-4 along with their bulk resistivities and bulk melting points. It was believed that improvements in film characteristics could be made through the use of: improved compound target materials of higher density and purity; co-sputtering from high purity metal and boron elemental targets; and the use of improved deposition techniques such as magnetron sputtering which, because of its higher potential deposition rates, should lead to reduced oxygen contamination.

ZrB_2 has also been studied by Motojima et al. [90]. It is a representative refractory compound having characteristics such as a high melting point, extreme hardness, high chemical stability against corrosion and good oxidation stability [91,92]. ZrB_2, deposited by chemical vapour deposition (CVD), was used as a coating on copper plates, because CVD deposition makes for a dense and adherent coating on metal substrates [93]. The ZrB_2 layers were deposited on copper by CVD using a gas mixture of $ZrCl_4$-BCl_3-H_2-Ar at temperatures in the range of 700-900°C. Tests were done on corrosion stability in acid solutions and for oxidation stability of the ZrB_2 coated copper

plate. The stability to oxidation of the coated plate was estimated from mass gain experiments in an air atmosphere. The effect of the thickness of the ZrB_2 layer on the mass gain for one hour of oxidation time is shown in Table 3-5, along with bare copper for comparison.

In another study on ZrB_2 thin films, the oxidation characteristics of the film have been observed [94]. The annealed resistivities were measured to be as low as 25-30$\mu\Omega$-cm. Oxidation characteristics of ZrB_2 were studied and it was shown that two distinct oxidation regimes exist. One regime, operating at temperatures at or below 625°C, produces thin tarnish like oxide layers less than 100nm thick. In contrast, the oxides developed on ZrB_2 at temperatures greater than 625°C are significantly different. Such oxides attained thicknesses greater than 1 μm when exposed to dry O_2 for 60 minutes. These oxides were analyzed and found to be ZrO_2, which is the stable phase below 880°C. This behaviour is very similar to that observed in the oxidation of ZrN [95]. The data collected indicate that both thin and thick oxides develop with a parabolic dependence on oxidation time and are therefore diffusion limited. However the parabolic rate constants are different for short and long oxidations at any given temperature. These results were consistent with three other studies, [91,96,97] on the oxidation of ZrB_2 at temperatures higher than that used by Shappiro et al. [94]. The oxidation of ZrB_2 in each of these studies was shown to be a parabolic diffusion-limited process proceeding stoichiometrically by the reaction

$$ZrB_2 + \frac{5}{2}O_2 = ZrO_2 + B_2O_3$$

where B_2O_3 is a liquid at temperatures higher than 450°C and ZrO_2 is compact and fine grained, and has a high resistivity between 600°C and 700°C. Dry oxidation is somewhat complicated by the formation of liquid Bi_2O_3 which migrates to the oxidized surface and forms a discontinuous film on it.

Many studies have been done to test the diffusion barrier characteristics between silicon and aluminum. Multilayer stacks are deposited onto the substrates by either CVD, magnetron sputtering or reactive sputtering. Metallizations are usually tested at temperatures below 650°C in forming gas, an inert ambient, nitrogen and/or in a vacuum. TaN and TiN have been tested and have been proven to be effective barriers between aluminum and silicon in an inert atmosphere at 550°C [98-101].

The performance of cosputtered $W_{75}C_{25}$ thin films as diffusion barriers between Si substrates and metallic overlayers of silver, gold, or aluminum was investigated by Yang et al. [102]. It was found that the WC layer prevents metallurgical interdiffusion and reaction between gold or silver overlayers and the silicon substrate up to 700°C and between an aluminum overlayer and silicon up to 450°C. The heat treatment was carried out at pressures below $3x10^{-7}$ torr for 30 min. Above these temperatures intermetallic compounds formed.

TiN and ZrN were tested as diffusion barriers [103] between aluminum and silicon at 550°C for 30 minutes. Again these samples were annealed in a vacuum. They were successful in acting as low resistivity diffusion barriers between aluminum and silicon. Both were found to prevent intermixing during heat treatments up to 550°C for 30 minutes.

Other nitrides, carbides and borides have been tested under similar conditions, for VLSI applications. They have good diffusion barrier characteristics at medium temperatures in a vacuum, while maintaining low resistivity values. However, there have been little or no oxidation tests done on thin films at high temperatures. Borides and carbides may have some of desired diffusion barrier properties necessary, but insufficient data was available to make a complete analysis. For this reason, silicides were chosen.

3.5 The Selection Process

After dismissing the nitrides, carbides, and borides, it was decided that silicide materials would be tried. The review of the silicides used in VLSI technology revealed a number of conclusions that helped in the selection of a diffusion barrier material. 1) All research into the oxidation of thin film silicides has been done on the silicon richest silicides. Nicolet and Lau [104] state that the temperatures required for their oxidation, during VLSI processing (about the same temperature of interest here), are elevated so that the silicon richest are of primary concern. This is in part because without exception silicon rich silicides have a more negative heat of formation per metal atom. This would explain the observed higher stability of the disilicides. 2) The transition metal silicides have the highest melting points and the lowest resistivities. Of

these the refractory metals have the highest melting points. This then narrows the search to silicon rich refractory metal silicides.

Melting points and resistivities of these nine compounds were given in Table 3-1. $CrSi_2$ has a high resistivity (~600 μΩ-cm) and a low melting point, while $TiSi_2$, $ZrSi_2$, and VSi_2 have relatively low melting points. Also, Zr and Ti oxides have more negative heats of formation than SiO_2 and possibly could form metal oxides readily. Based on previous arguments from above, $HfSi_2$ and WSi_2 would not be good barriers because Hf oxide has the most negative heat of formation per oxygen atom of the refractory metals and it has been shown that $HfSi_2$ decomposes to form a metal oxide. It has been shown that WSi_2 pests at elevated temperatures. This leaves $NbSi_2$, $TaSi_2$, and $MoSi_2$ as the three best candidates for diffusion barriers. Of these three, $MoSi_2$ was chosen as the material for this study.

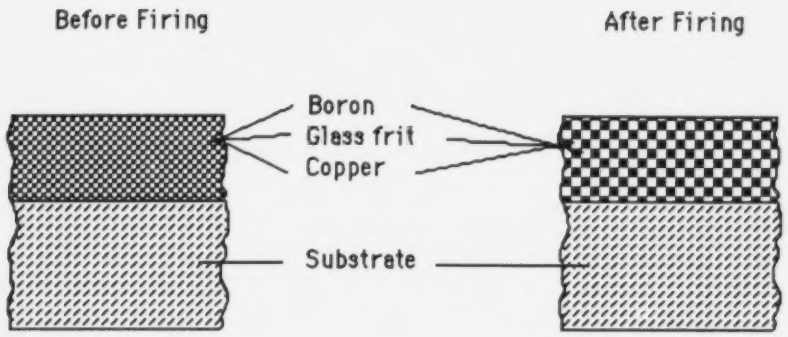

Figure 3-1: First generation thick film air fired copper conductor paste. Boron powder is incorporated into the copper paste [105].

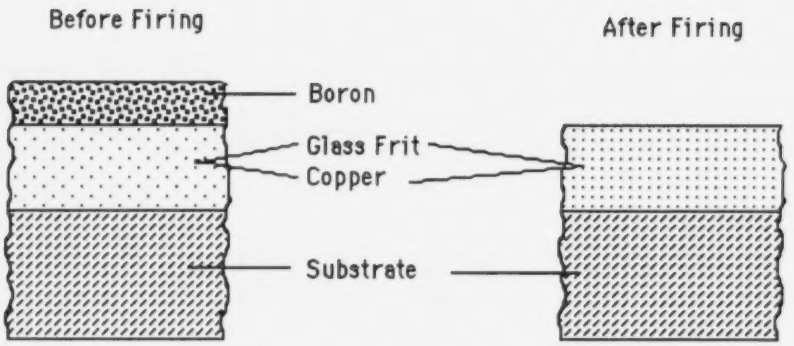

Figure 3-2: Second generation thick film air fired copper conductor paste. Boron powder is appled to the surface of the copper paste [105].

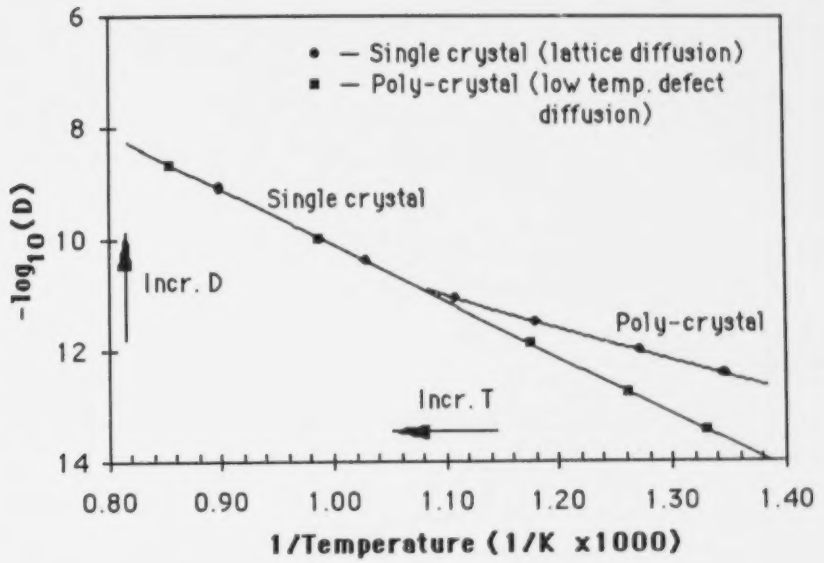

Figure 3-3: Arrhenius plot of tracer diffusion values for silver in silver single crystal and polycrystalline samples [106].

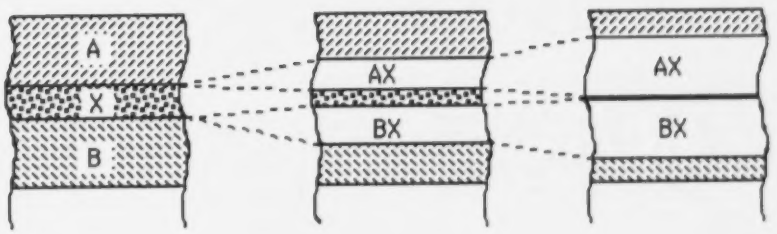

Figure 3-4: Sacrificial barrier. The diffusion barrier, X, forms compounds with layers A and/or B. If the reaction of the barrier layer with A and B are fully characterized and laterally uniform, the point at which the layer X will be fully consumed can be predicted. As long as this point is not reached, a separation of A and B is in fact accomplished [107].

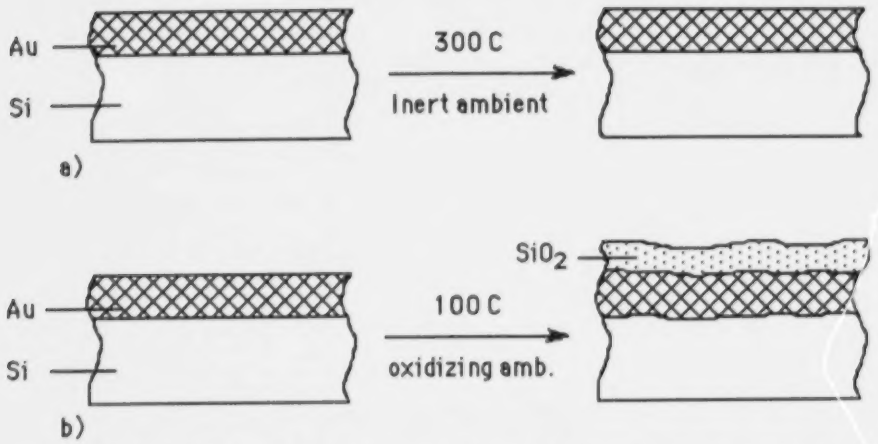

Figure 3-5: The presence of a sink can affect the stability of thin films. a) A thin film of gold deposited on a silicon wafer is quite stable when annealed in an inert ambient but, b) it does not withstand even moderate annealing in air [107].

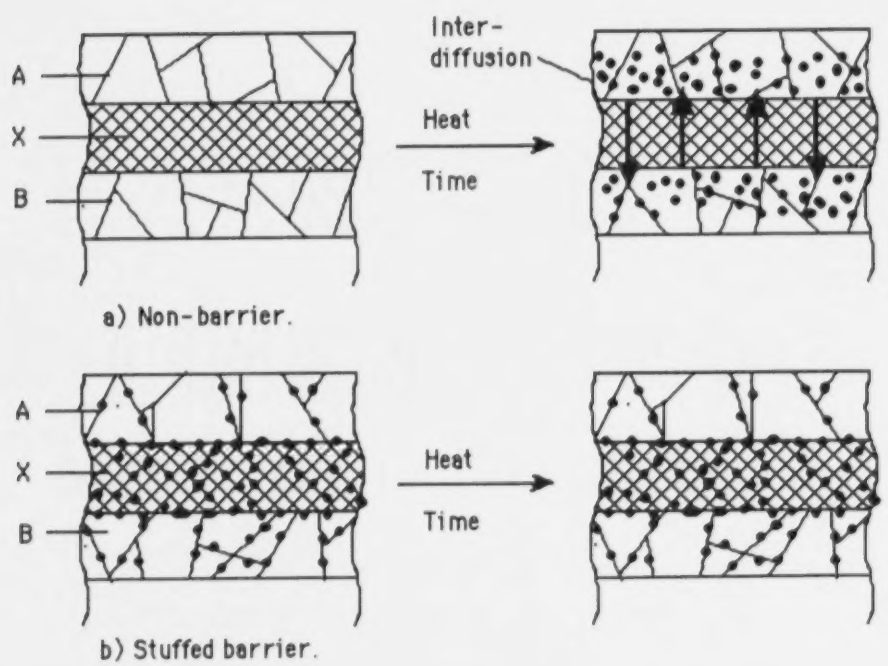

Figure 3-6: a) The non-barrier fails because of defects which act as fast diffusion paths. Material 'B' and 'A' form a solid solution. b) Impurities may "plug" these fast diffusion paths, thus creating a useful diffusion barrier [107].

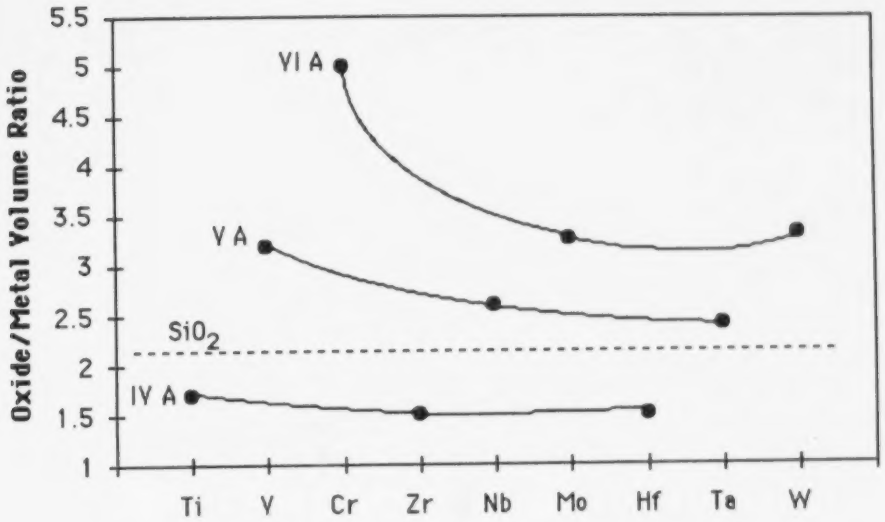

Figure 3-7: The oxide to metal volume ratio for various oxides of groups 4A to 6A elements [50].

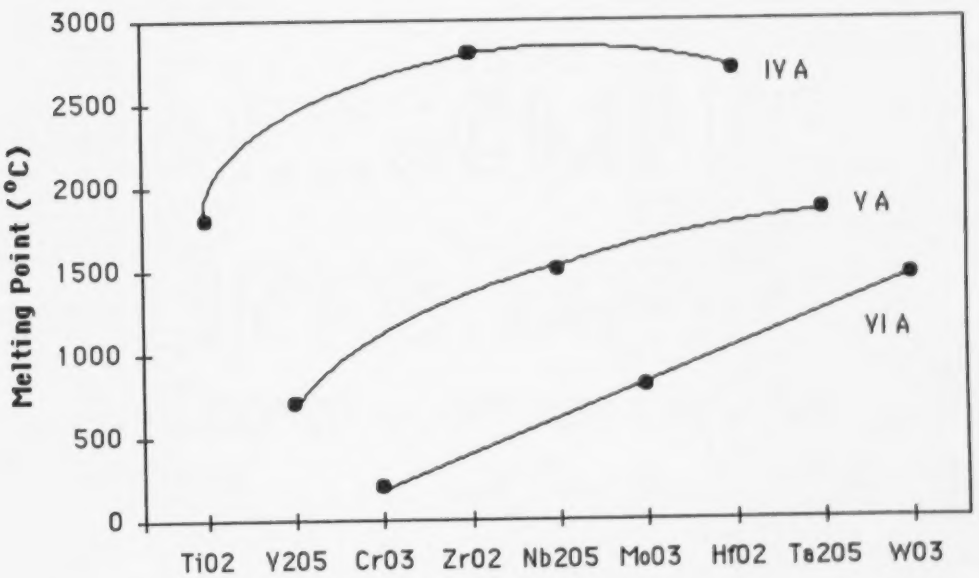

Figure 3-8: A plot of the melting points of the oxides of group 4A, 5A and 6A elements [50].

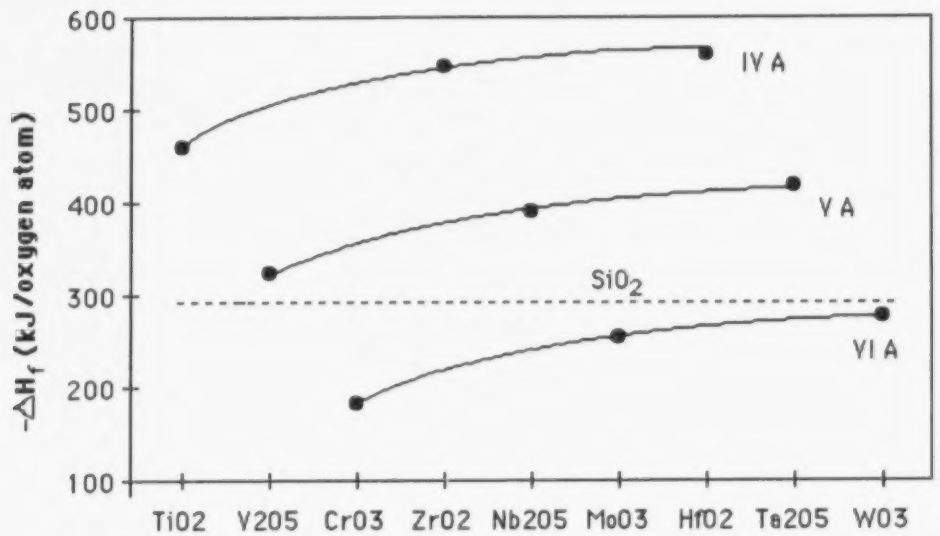

Figure 3-9: The heats of formation (ΔH_f) per oxygen atom of various oxides of groups 4A to 6A elements [50].

Table 3-1: Properties of refractory metal silicides and their oxides.

	Melting Point(°C) [108,104]	Resistivity (μΩ-cm) [104]	$-\Delta H_{f,O}$ (kcal/O atom) [104,110]	$-\Delta H_{f,m}$ (kJ/metal atom) [104,110]
TiSi2	1540	13,25		134
TiO2			460	917
ZrSi2	1700	35-40		226
ZrO2			548	1097
HfSi2	1800	45-50		226
HfO2			561	1122
VSi2	1670	50-55		310
V2O5			322	800
NbSi2	1950	50		138
Nb2O5			389	967
TaSi2	2200	35-55		117
Ta2O5			419	1047
CrSi2	1550	~600		121
CrO3			188	573
MoSi2	1980	21, 100		117
MoO3			251	753
WSi2	2165	12,70		92
WO3			276	841
Cu_2O			276	85
CuO			172	157
SiO_2			159	

Table 3-2: Kinetics of SiO_2 growth by thermal annealing of silicide films in a dry oxidizing ambient [49].

Silicide film	Substrate	Kinetics x=thickness t=time	Rate Constants B/A(cm/sec) B(cm^2/sec)	Temp. Range (°C)	Activation Energy (eV)
- -	Si(xtl)	$X^2+Ax=B(t+\tau)$	$B/A=1.97\times10^{-9}$ $B=3.25\times10^{-14}$	650-1200	1.24
$CoSi_2$	Si(100)	$X^2=Bt$	$B=3.09\times10^{-14}$	650-1100	1.39
$NiSi_2$	Si(poly) SiO_2	$X^2=Bt$	$B=1.11\times10^{-14}$	700-900	1.5
$TiSi_2$	Si(poly)	No Oxidation	- -	700-1100	1.51
$MoSi_2$	SiO_2	$X^2+Ax=B(t+\tau)$	$B/A=2.8\times10^{-9}$ $B=1.9\times10^{-14}$	900-1100	1.6

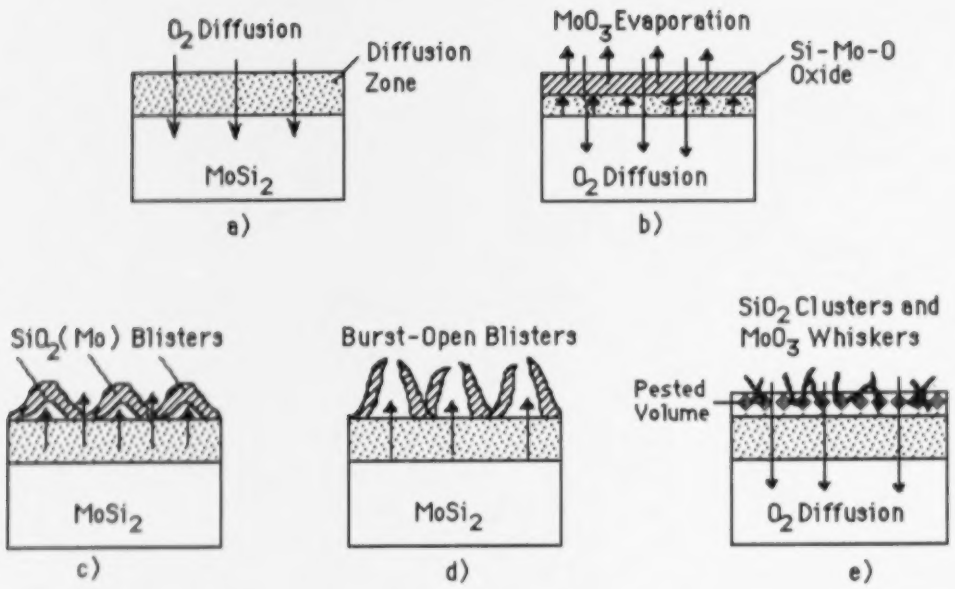

Figure 3-10: Schematic drawing showing the various steps of the pesting reaction occurring in single crystal $MoSi_2$ [81].

Table 3-3: Bulk properties of the transition metal carbides and nitrides.

	Bulk Melting Point(°C) [89,111]	Bulk RT - ρ (μΩ-cm) [89,111]
Ti	1677	54
TiC	3067	51-188
TiN	2949	25-54
Zr	1852	44
ZrC	3420	42-50
ZrN	2982	7-37
Hf	2222	32
HfC	3928	37-45
HfN	3387	33
V	1917	20
VC	2648	60-65
VN	2177	85
Nb	2487	16
NbC	3600	35-51
NbN	2204	44-90
Ta	2997	13
TaC	3983	20-42
TaN	3093	128
Cr	1900	13
Cr3C2	1810	- -
Cr2N	~1500	- -
Mo	2610	6
MoC	2600	- -
MoN	<800	- -
W	3380	5
WC	2776	22
WN	<800	- -

Table 3-4 Resistivity and melting points of thin film ZrB_2 and TiB_2.

	[37]Bulk $\rho(\mu\Omega\text{-cm})$	[93]Thin Film annealed $\rho(\mu\Omega\text{-cm})$	[112]Melting Point (°C)
ZrB_2	7-38	75	3245
TiB_2	9-28	150	2980

Table 3-5: The effect of varying thichnesses of ZrB_2 layers on the mass gain of a ZrB_2 coated copper plate exposed in air at elevated temperatures for 1 hour. [90].

Temperature (°C)	ZrB_2 coating thickness (μm)	Mass gain for ZrB_2 (mg/cm^2)	Mass gain for plain Cu (mg/cm^2)
800	2	4.5	~7-9
	4	3.7	
	8	0.5	
700	1.8	0.8	~4-5
	2.4	0.8	
	5.0	0.8	

CHAPTER 4

EXPERIMENTAL PROCEDURES

4.1 Substrates and Depositions

Several different substrates were used. Electrolytic tough pitch (ETP) copper, with less than 0.05% oxygen content purchased from a local materials supplier, was used to conduct preliminary tests by depositing films onto its surface. The ETP copper came in a sheet measuring 60 cm x 60 cm x 0.625 mm. Smaller sample sizes were sectioned off using a shearing machine as necessary. Substrate surfaces were cleaned of organics and native oxides before depositions were carried out. There were several different cleaning methods tried for removing any oxides from the surface of the copper, which are summarized in Table 4-1. The ETP copper was sectioned and polished on successively finer grade paper from 400 grit to 600 grit, then 6.00μm diamond and 0.30μm alumina. Films were deposited on heated and unheated substrates. Finally, some samples had copper sputtered onto their surface in an attempt to smooth out the roughness. The ETP copper was also used in an oxidation control study, to measure the oxide growth of pure copper under the same conditions as the test samples.

Other substrates used were thin film grade alumina (Al_2O_3) and silicon (Si). The alumina substrates (ADS-996) which were purchased from Coors Ceramic Company, Electronic Division, were polished on one side and laser scribed into 6.35mm (0.25 inch) squares from the back. Coors' specifications give the average grain size, as determined by the intercept method, to be <1.2 μm, with a surface finish of <75 nm (<3 μin) center line average (CLA). Silicon substrates had SiO_2 grown either by plasma enhanced-chemical vapour deposition (PE-CVD) or by a wet oxidation method. For the PE-CVD method, SiO_2 was grown on one side only; for the wet oxidation method, SiO_2 was grown on two sides. Wet oxidation was carried out by bubbling nitrogen, as the carrier gas, at 20 psi through boiling water into a furnace. A temperature setting of 1100°C for 2.5 to 3 hours was used. The cleaning method used for the silicon and

alumina included a strong oxidizer, i.e., a pirana etch, which was 3 parts by volume sulfuric acid and 1 part hydrogen peroxide.

The different substrates were used to facilitate characterization, depending on the type of analysis needed. Alumina substrates were used for the thermal gravimetric analysis (TGA) to avoid any oxidization mass gain from the substrate. Since thin film grade alumina substrates are relatively rough compared to polished silicon, adhesion was enhanced by the mechanical bonding between the copper and the substrate. The silicon substrates were used to facilitate transmission electron microscopy (TEM) sample preparation. Other analysis techniques were carried out on appropriate substrates and will be presented later in the Results and Discussion chapter.

Films were deposited at the Alberta Microelectronic Centre (AMC). Nominal thicknesses for films deposited on ETP copper, alumina, and silicon are given in Tables 4-2, 4-3 and 4-4 respectively. Silver and molybdenum films were deposited by electron beam evaporation. Typical electron beam evaporation conditions were 6 nm/s deposition rate, 10 mA current, and a $2x10^{-7}$ torr base pressure for silver, and 0.17 nm/s deposition rate, 145 mA current, and a $2x10^{-7}$ torr base pressure for molybdenum.

Both copper and $MoSi_2$ were deposited using magnetron sputtering. The deposition conditions were 8 mtorr Ar, 20.5 sccm Ar flow, 800W power, and 1.71A current for copper; and 8 mtorr Ar, 20.5 sccm Ar flow, 100W power, and 1.14A current for $MoSi_2$. Both were done with a base pressure of $1x10^{-6}$ torr. Samples were oscillated through 9^{o} and 2 min/rev during deposition for increased uniformity of the films. All layers were deposited in situ, without breaking vacuum.

4.2 Annealing Procedure

The copper substrate samples were annealed in air in a Lindberg box furnace at 600°C, 700°C, and 800°C. They were inserted into the center of the furnace next to the thermocouple for 10 minutes and were taken out directly, or allowed to furnace cool with the door open.

All other samples, which were on silicon or alumina substrates, were annealed in air in a Radiant Technology Corporation (RTC) infrared (IR) furnace Model Cu-900. The IR furnace had four independently controllable heating zones with an air cooling section directly following the last zone. The IR furnace is typically used for firing thick film pastes. A typical thick film paste firing profile is shown in Figure 4-1. Our firing profile deviated from this profile in order to gain better quantifiable peak times for our kinetic data collection. A typical firing profile used for our test samples is given in Figure 4-2. Four temperatures, 600°C, 700°C, 800°C, and 850°C, each with three to four different peak times of 2, 5, 8, 10 and/or 15 minutes were used. The belt speed was varied accordingly to attain minimum ramp and appropriate peak times. ETP copper was annealed in the RTC-IR furnace as a control under the same time temperature profiles as the silicon and alumina substrate samples. All samples were placed in the middle of the belt and the profiles of each run recorded.

4.3 X-Ray Diffraction (XRD)

Samples were analyzed using an X-ray diffractometer with Cu-Kα radiation. Two machines were utilized, the first was an older model consisting of a Rigaku Denki D-F3 generator and a Philips PW1380 goniometer connected to a chart recorder. The second was a Siemens D-5000 XRD diffractometer with a Peltier silicon detector connected to a 386-DX IBM-PC. Raw XRD data from the Siemens machine was converted to ASCII files and plotted with the aid of spreadsheets, Quattro-Pro for IBM Windows, or Excel for Macintosh. Peak intensities and the corresponding two-theta values were compared to JCPDS Power Diffraction Files [113] for identification of phases. Any phase changes and/or growth of phases were monitored for the various annealing times and temperatures.

4.4 Light Microscopy

Light microscopy work was done using a Zeiss Ultraphot II light microscope, with a Hitachi solid state colour video camera, and a Nikon Epi-phot optical microscope. Low magnification micrographs of the surfaces of some of the sample films were recorded before and after annealing. Samples were prepared using a cold mount Leco epoxide with a curing time of 4 hours or with a hot mount resin that cured in 30 minutes at 55°C.

Polishing was carried out on successively finer grit paper, from 320 SiC to 600 SiC grit with final polishing done with 0.05 μm alumina. Cross-sections of annealed pure copper were prepared for some of the extreme times and temperatures in order to measure the relatively thick oxide layers that had formed.

4.5 Atomic Force Microscopy (AFM)

Atomic force microscopy (AFM) was carried out before and after annealing. A TopoMetrix Corp. TMX2000 AFM was used to analyze the surface of the films. Scans of 25 μm or less were done with a relative force of ~0.1 nN and a scan rate of 6 -10 Hz. Line scans of the surface were used to identify and quantify local roughness, topographical information, and pinholes. The AFM was essentially used as a very accurate profilometer, while imaging the surface topography at the same time.

4.6 Scanning Electron Microscopy (SEM)

Scanning electron microscopy samples were prepared in a similar fashion as light microscopy samples above. In addition though, a thin coating of carbon was applied to the surfaces by flash evaporation to avoid charging of the sample in the SEM. Two SEM's were used: a Hitachi S-2700 scanning electron microscope, with a LINK eXL energy dispersive X- Ray analyzer using an ultra-thin window and a lithium drifted Si detector, and a JEOL-6300F field emission SEM, with a Noran energy dispersive X-ray (EDX) analyzer. Surfaces and cross-sections were prepared. EDX spectra were collected from surfaces of as deposited and annealed samples. Polaroid photos and video prints were taken.

4.7 Transmission Electron Microscopy (TEM)

Both plan view and cross-sectional samples were prepared for transmission electron microscopy. All cross-sections for TEM were made from metallizations that were deposited on silicon. Three TEM's were used: a 200kV JEOL 2010 TEM with a Noran ultra thin window, Ge X-ray detector, a 125kV Hitachi H-7000 TEM, and a 100KV Philips EM-300.

Cross-sectional TEM samples were made in the following manner:

1. Two 6.5mm x 1.5mm pieces were cut from a sample and glued with the film surfaces facing each other.
2. Plain silicon slabs of the same size were then glued on either side of the sample to achieve a stack thickness of about 4 mm perpendicular to the epoxy plane, (Figure 4-3a). The epoxy was applied in such a fashion as to prevent any bubbles from forming. The stack was gently squeezed in a vise and the epoxy was cured in a furnace at approximately 100°C for 8-12 minutes.
3. A 2.3mm diameter cylinder was cut from the stack using a Gatan ultrasonic disc cutter, with the film interface in the middle of the cylinder. This was then glued into a tube with an inside diameter of 2.4mm and an outside diameter of 3.0mm.
4. The assembly was then mechanically thinned to ~150μm using 320 and 400 grit SiC sand paper.
5. One side was polished on a Gatan dimpling machine to a mirror finish. Then a spherical section was thinned on the other side until a very small hole appeared. Again it was polished to a mirror finish. This created a thin central region with the film interface at the bottom center of the sphere (Figure 4-3b).
6. The final thinning was done with a Gatan Duo Mill 600TMP Ion Mill. The sample was kept cold with liquid nitrogen under a base pressure of $<10^{-5}$ torr. Two Ar^+ ion guns were used to sputter the sample at an incident angle of 13° to the horizontal, while the sample was rotated. An accelerating voltage of 4 kV and an ion gun current of 0.5 mA per gun were used for 0.5 to 2.0 hours until there was a thin region ~100nm thick at the film interface.

EDX spectra were collected for the various cross-sectional layers along with convergent beam electron diffraction (CBED) and selected area diffraction (SAD) patterns for phase identification where possible. Oxide thicknesses were measured from TEM micrographs and oxide kinetics were determined.

4.8 Thermal Gravimetric Analysis

In addition to quantifying the kinetics by cross-sectional thickness measurements through TEM and SEM images, thermal gravimetric analysis (TGA) was also used. A Shimadzu TGA-50H was used with a furnace size of ~125mL and a reported sensitivity of ~10 μg. Gas flow rates through the furnace were 50mL/min, with extra

dry air and ultra high purity Ar (99.995%) as the working gases. Al_2O_3/Cu/$MoSi_2$(200nm), Al_2O_3/Cu/$MoSi_2$(100nm) and SiO_2/Si(75μm)/SiO_2/Cu/$MoSi_2$(200nm) samples were analyzed. Alumina substrates were used instead of CVD oxidized silicon because any oxidation due to silicon would make the oxygen uptake for the copper erroneously high. The alumina was thinned from 625μm to ~100μm to reduce the total mass of the sample, so that expected oxygen mass gain was <0.4%. This reduced the overall mass from an initial 100mg to ~17mg. Samples were ramped to peak temperature in Ar gas with a flow rate of 50mL/min at 50°C/min. To allow the microbalance to stabilize from any noise induced by convection currents and buoyancy inside the furnace, the sample was held at peak temperature for an additional 15-20 minutes. Once equilibrium was reached the gas inside the furnace was switched from argon to air and the mass gain was monitored until complete oxidation occurred.

Table 4-1: Various cleaning procedures for copper substrates.

DESIGNATION	CLEANING PROCEDURE
Standard (Std)	Ultrasonic bath in acetone followed by de-ionized water rinse.
A	Nitric acid/H_2O for 1 minute.
B	Nitric/H_2O for 2 minutes.
C	No Cleaning

Table 4-2: Preliminary tests using copper substrates[1].

Cu(ETP)/Ag(1000)	
Cu(ETP)/Mo(100)/Ag(1000)	-no substrate heating.
Cu(ETP)/Mo(100)/Ag(1000) Cu(ETP)/Mo(200)/Ag(1000)	-substrate heating (200°C).
Cu(ETP)/Cu^{sput}(2000)/Mo(200)/Ag(500)	
Cu(ETP)/Cu^{sput}(5000)/$MoSi_2^{sput}$(150)/Ag(1000)	

1 All films were deposited by electron beam evaporation exept where indicated by sput (sputter deposit).
2 Various substrate cleanings were tried.
3 Substrates used were electroytic tough pitch copper (ETP) 99.5% pure.
4 Numbers in brackets are nanometers.

Table 4-3: Main test samples for alumina substrates[1].

Al_2O_3/Cu(2000)/$MoSi_2$(100)
Al_2O_3/Cu(2000)/$MoSi_2$(200)

1 All films were sputtered deposited.
2 Numbers in brackets are nanometers.

Table 4-4: Main test samples using silicon substrates[1].

[2]$Si/SiO_2/Cu(2000)/MoSi_2(100)$
[2]$Si/SiO_2/Cu(2000)/MoSi_2(120)$
[2]$Si/SiO_2/Cu(2000)/MoSi_2(200)$
[3]$SiO_2/Si(75)/SiO_2/Cu(2000)/MoSi_2(200)$ (TGA analysis)
[3]$SiO_2/Si/SiO_2/Cu(2000)/MoSi_2(400)$

1 All films were sputtered deposited.
2 SiO_2 (~500 nm) was grown on one surface by CVD.
3 SiO_2 (~500 nm) was grown on both surfaces by wet oxidation.
4 Numbers in brackets are nanometers.

Table 4-5: Firing schedule for the tests on alumina and silicon.

$Al_2O_3/Cu(2000)/MoSi_2(100nm)$ and $Si/SiO_2/Cu(2000)/MoSi_2(100)$		$Al_2O_3/Cu(2000)/MoSi_2(200)$ and $Si/SiO_2/Cu(2000)/MoSi_2(200)$		$SiO_2/Si/SiO_2/Cu(2000)/MoSi_2(400)$	
Peak Temp. (°C)	Nominal Time (min)	Peak Temp. (°C)	Nominal Time (min)	Peak Temp. (°C)	Nominal Time (min)
600	2 5 10	600	2 5 10	600	2 5 10 15
700	2 5 10 15	700	2 5 10 15	700	2 5 10 15
800	2 5 10	800	2 5 10 15	800	2 5 10 15
850	2 5 8 10	850	2 5 8 10	850	2 5 8 10

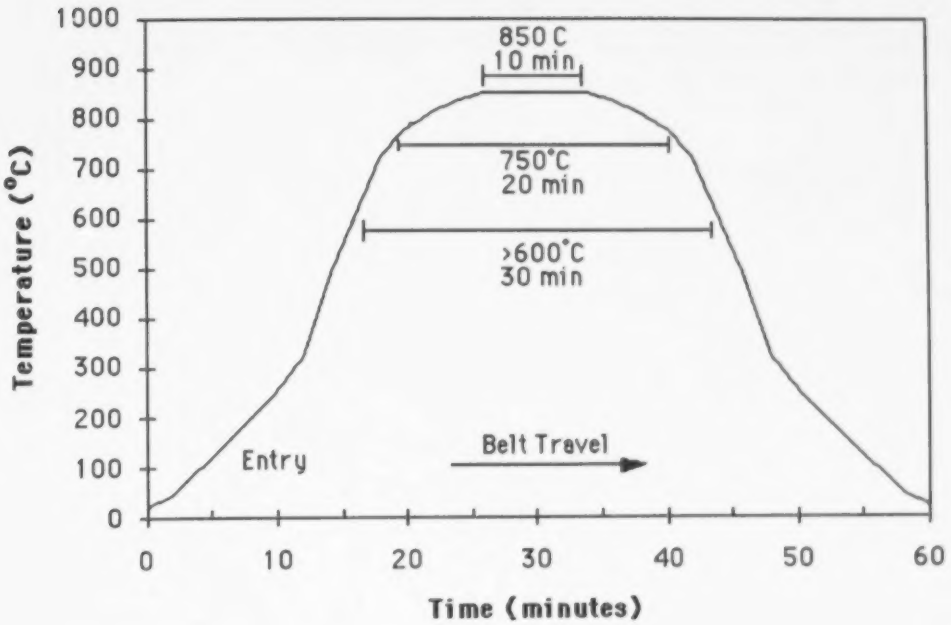

Figure 4-1: Typical thick film firing profile [114].

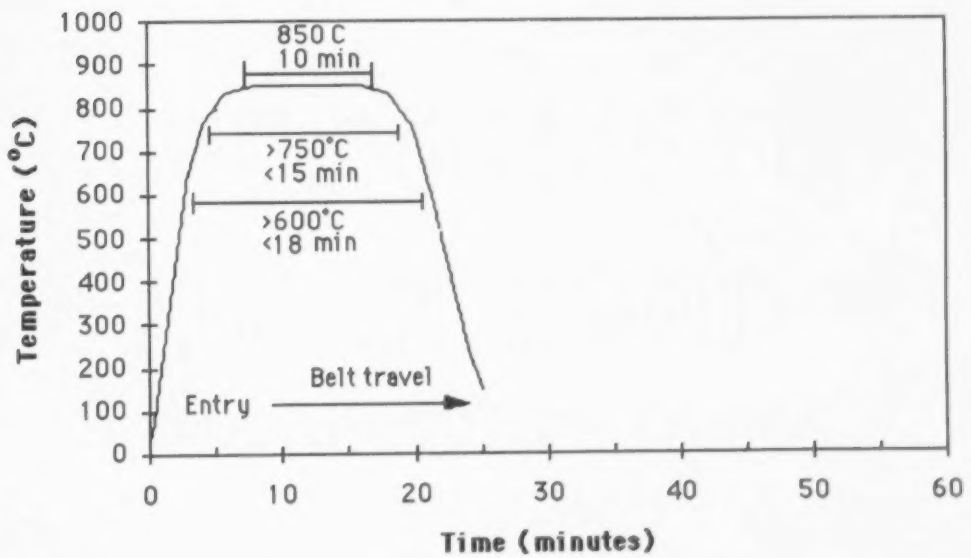

Figure 4-2: Typical modified firing profile for test samples using an IR furnace.

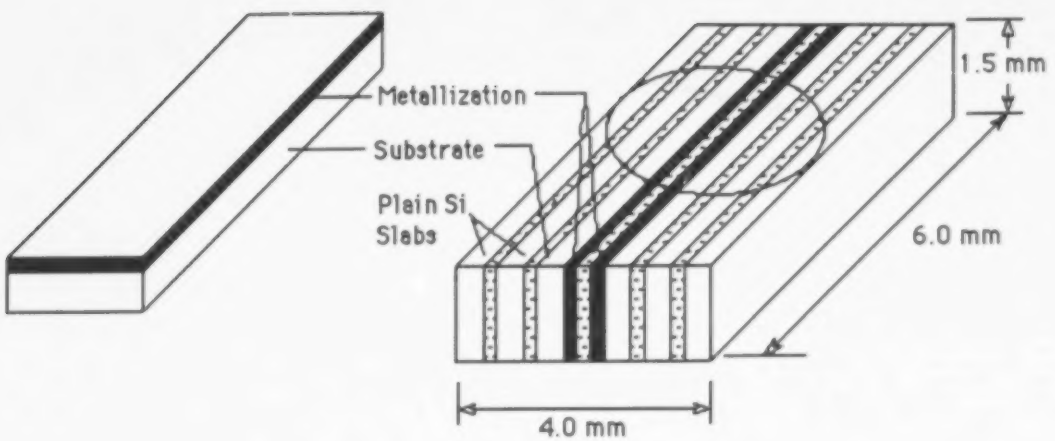

Figure 4-3a: Schematic drawing showing various steps in cross-section TEM sample preparation.

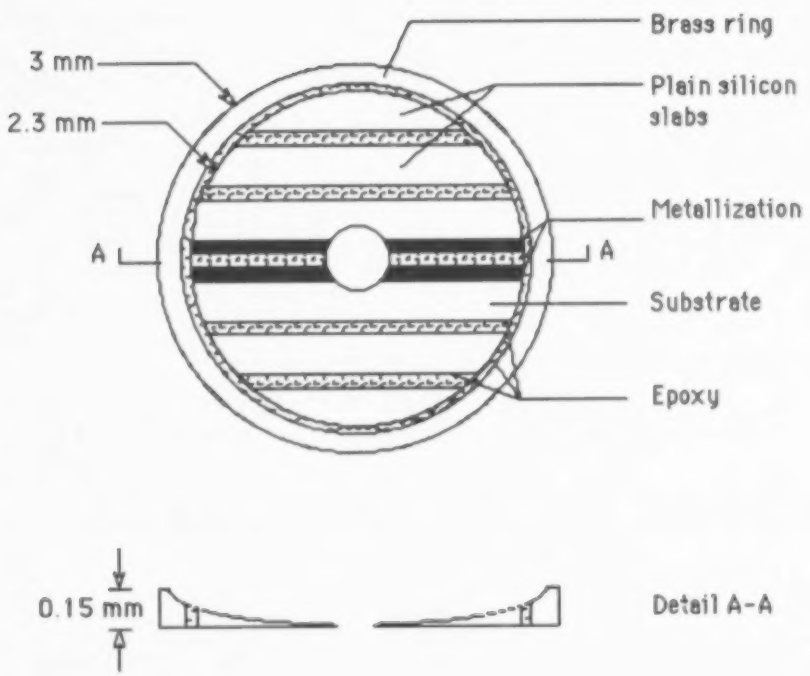

Figure 4-3b: Schematic of cross-section TEM sample after dimpling and polishing.

Chapter 5

Results and Discussion

5.1 Oxidation of Copper

Although kinetic data for the oxidation of copper was available in the literature, an oxidation study of copper was completed using similar furnace profiles as the samples with diffusion barrier coatings. Thus a direct comparison of bare copper could be made against samples coated with the $MoSi_2$ diffusion barrier. A belt furnace was used to model thick film firing profiles. However, the profiles were modified somewhat in order to better quantify the kinetics of oxidation (this was discussed in Chapter 4, Experimental Procedures). Also, since the annealing times were relatively short, calculations were carried out to determine what effect the ramping had on the data obtained. The time at 90%, of the peak temperature was used to test for the effect of the ramp (Figure 5-1). Figure 5-2 shows a typical annealing profile as recorded by a thermocouple placed beside the sample during annealing. This thermocouple was used to monitor the temperature so that the belt speed could be adjusted accordingly. The belt speed was adjusted while the sample was in the furnace so the ramp time could be kept the same, from sample to sample, while the peak time varied.

Both Cu_2O and CuO oxides formed on the surface of copper with Cu_2O forming adjacent to metallic copper, i.e, $Cu/Cu_2O/CuO$. Figure 5-3 is a typical optical micrograph taken from 800°C for a nominal time of 15 minutes. The dark gap between the copper and the Cu_2O is a sample preparation artifact; it is a space between the two layers where the oxide separated from the copper, and not because oxide was removed. The percent of CuO varied from 5% to 10% at 600°C, 2% to 5% at 700°C, and nil to 2% above 800°C. Thickness measurements were made on the oxide and comparisons were made with literature values. A plot of thickness squared vs time, for the oxidation of bare copper at 850°C, is given in Figure 5-4. The thickness squared is plotted for 100% and 90% peak temperatures. The slope of the 100% line is greater than the 90%

line; this trend is typical for all the annealing temperatures. The surface oxide was inspected by eye after annealing. It remained intact as a continuous planar sheet, for the 850°C and 800°C samples, but did not adhere to the surface of the metallic copper. The ratio of the linear coefficients of thermal expansion between copper and Cu_2O is 4.32, which is high enough for oxide separation to occur during cooling from elevated temperatures. The oxide for the 700°C and 600°C anneals, and particularly for the shorter annealing times, was flaky and generally did not consist of a planar sheet. However, there were areas where the oxide remained intact. These areas were subsequently used for oxide thickness measurements. The oxide at lower temperatures was thinner and structurally weaker than the oxides that formed at the higher temperatures, thus causing it to spall to a greater extent.

Figure 5-5 and Table 5-1 summarize the results of the copper oxidation experiment. Figure 5-5 graphically illustrates the oxide thickness growth rates at the four temperatures. The oxide growth fits parabolic growth behaviour for bare copper at 600, 700, 800, and 850°C. A minimum of 50 measurements were taken for each data point, the standard deviation for each point is less than the size of the data marker, and the coefficient of determination (r^2), for each line, ranges from 0.968 to 0.995. Table 5-1 compares literature values of parabolic rate constants with experimental rate constants. The literature values are given for the total oxide present. The experimental values are given for the Cu_2O only, but these values are conservative since they underestimate the total oxide thickness. CuO was not present in the quantities that were expected (this will be discussed later) and may have spalled off the Cu_2O; therefore, only Cu_2O was quantified. The amount of copper consumed was also calculated from the experimental thickness data assuming a compact and planar Cu_2O oxide and again these are conservative values. This data will be used later to directly compare with the diffusion barrier samples. The thickness and amount of copper consumed for 15 minutes is tabulated. Figure 5-6 shows an Arrhenius plot of the data in Figure 5-5. The apparent activation energy is Q_{app} = 83.6 kJ/mol. Similarly, the coefficient of determination shows there is a good fit to the data.

To determine what effect the ramp had on the values obtained for the rate constants, a correction was made to compensate for additional oxide growth during the ramp. The time at 90% of the peak temperature was arbitrarily chosen; this effectively had increased the actual peak time. It also shifted the curve to the right and reduced the y-intercept (Figure 5-4). For all temperatures the slope was reduced, but not by more

than 8%. Additionally, 80%, 70%, and 60% lines were used to recalculate the rate constant for 700°C. None varied by more than 10% from the 100% value. This result is not surprising since the ramps for all samples were similar, and thus had a similar effect at all times.

The study of copper oxidation over the past 70 years illustrates a number of points. Factors which can influence the results of oxidation include the pretreatment of samples, method of analysis, and experimental conditions. A collection of oxidation curves from many different authors shows that there is agreement between different investigators at high temperatures, but this agreement becomes progressively poorer as the temperature decreases. In studies that have been done using gravimetric methods that measure mass uptake of oxygen, conversions to actual oxide thicknesses rests on the assumptions that the film is compact and planar and the relative ratios of Cu_2O and CuO are quantifiable for a given temperature. It has long been accepted that thick oxide scales on copper are composed of an inner layer of Cu_2O and an outer one of CuO. This is in agreement with the theory of composite oxide layers developed by Wagner [4,115] and Valensi [7]. However, empirical data collected by various authors for the percentage of CuO oxide varies. There is progressively increasing disagreement regarding relative ratios of Cu_2O and CuO below 800°C. At 600°C the percentage range of CuO is 15% to 55%, for 700°C, 5% to 30%, and for 800°C, nil to 15% [116]. At temperatures greater than 800°C CuO is prone to porosity and is not considered to contribute to the growth rate of the oxide scale. Below 800°C the CuO content of the scale increases with decreasing temperature. Below ~250°C, Cu_2O is the only oxide formed during the earlier stages of the reaction, and even when CuO does eventually appear, it does not become predominant [116].

From the experimental results, the CuO oxide thickness varied as a percentage of the total oxide thickness but only because the relative Cu_2O thickness changed. The CuO layer was about 2μm to 4μm thick for all samples. CuO may have spalled from the surface of Cu_2O, leaving behind a thin residual layer. Another possible explanation for lower CuO thicknesses is found from electron diffraction work [117,118], which indicates that the composition of the oxide layer is a function of time during the earlier stages of the reaction, but it appears to become constant with prolonged oxidation [6,119]. Cruzan and Miley [120] and Bouillon [121] found that no CuO was formed below a critical film thickness. The values reported for this critical thickness are in poor agreement (0.06μm at 240°C[120] and 0.26μm at 250°C[121]), possibly

because of different systematic errors in the methods of determination. After Cu_2O forms on the surface of copper it has been shown that, at 150°C and 500°C [122], no CuO is observed until a coherent film has been formed.

From Table 5-1 it is noted that the experimental rate constant values are higher than the data taken from the literature in all cases, but are in close agreement at 800°C and 850°C. Though there is some discrepency between the data, the barrier samples have been annealed under the same firing profiles as the bare copper. Also, since the thickness measurements have been made on Cu_2O oxide only, they are conservative. A direct comparison between the bare copper samples and diffusion barrier samples will be made later.

5.2 Diffusion Barriers on Copper Substrates (Preliminary Work)

The initial effort to create an air firable metallization involved depositing a diffusion barrier between a copper substrate and a silver layer. The outer silver layer was deposited to parallel the final process where a coating of silver might prove to assist the sintering process of thick film pastes. Also, 14 at% copper is soluble in silver at the eutectic temperature of 779°C. Silver can potentially dissolve some of the copper before it oxidizes at the surface for a Substrate/Cu/Barrier/Ag planar metallization system. Given a 1μm thick silver layer, 86.6μg of copper could be dissolved into a unit area of silver (square cm). As the atoms of copper diffuse through the diffusion barrier, they would disolve into the silver layer before forming an oxide on the surface of the silver. Stated another way, 1μm of silver could theoretically prevent an equivalent of 130nm of CuO from forming. To evaluate the prospective materials, metal layers of silver and the diffusion barrier were deposited on copper substrates. This sort of configuration facilitated characterization and was also less expensive than processing actual copper composite powders. The diffusion barrier selected was $MoSi_2$. Molybdenum was also used to continue some previous work done by Sherritt. The reasons for selecting $MoSi_2$ as a barrier were outlined in Chapter 3, but the key requirements can be summarized as follows: the barrier material had to resist oxidation, prevent the oxidation of copper, and have a low resistivity.

Analysis of the as deposited samples by XRD and SEM X-ray energy dispersive analysis had detected no oxides, or other reaction products. The detection limit of these

analysis techniques might not have been sensitive enough to detect minute amounts of oxygen or oxide. The adhesion character of the films was qualitatively evaluated according to whether the film delaminated with a cotton swab rub (poor) or with scotch tape (fair). Adhesion of evaporated silver films was poor. The molybdenum film would peel off in places when scotch tape was used (fair), and $MoSi_2$ did not peel off with scotch tape (>fair). It can be surmised that the adhesion of the $MoSi_2$ was better because it was deposited using a sputtering technique. Sputtered particles have a higher particle incident energy, ~10-40eV, compared to 0.2eV for evaporation, thus atoms are implanted into the substrate to a greater extent than evaporation. Appendix B gives a brief discussion of some of the factors which affect film adhesion.

Various cleaning procedures were performed (as discussed in Chapter 4) and substrate heating was tried (to remove any water vapour that might be on the surface of the substrate) to improve adhesion of the deposited films. Neither of these methods showed any improvement over a standard ultrasonic acetone bath followed by a rinse in deionized water.

Copper duplex scales (Cu_2O and CuO) were found on the surfaces of all annealed samples. Cu_2O was adjacent to the copper substrate while CuO formed the outer layer. The copper oxide was brittle and spalling occurred for many of the samples. Figures 5-7 and 5-8 show typical duplex oxide morphology for the barrier samples. The SEM backscattered electron micrographs show Cu/$MoSi_2$(150)/Ag(1000) and Cu/Mo(200nm)/Ag(1000nm) annealed at 700°C for 10 minutes and 800°C for 10 minutes respectively. The backscattered electron images show the higher average atomic number compounds as brighter than lower ones. Thus in order of brightest to darkest there is silver, copper, Cu_2O, and CuO. Silver was found to be dispersed in the CuO oxide for all cases, while the location of the barrier layer was uncertain with respect to the oxides. The oxide layers appeared to grow uninhibited after breaking the structural integrity of the $MoSi_2$ and Mo barrier films. The ratio of thermal expansion coefficients for Cu:$MoSi_2$ is 2.1:1 and Cu:Mo is 3.7:1. This could have led to induced stresses at elevated temperatures causing the barrier film to crack.

The oxidation resistances of the diffusion barrier samples were essentially no better than the bare copper samples. By using copper substrates it is believed that the roughness of the surface contributed to the deterioration of the barrier film. If the barrier was discontinuous upon deposition and there were exposed areas of copper, then

oxide could have readily formed at these breaks in the film. Oxide forming at breaks could have caused the thin barrier layer (<200nm) to crack further, thus further exposing the underlying copper. The diffusion barrier would become ineffective once severe cracking occurred and oxidation would proceed as in the bare copper samples.

To address the roughness hypothesis, polished silicon and alumina substrates were used instead of copper and surface roughness measurements taken. It was further decided that because of the poor adhesion of silver, the metallization system would be simplified by eliminating silver and to test only the diffusion barrier on copper. Also, since previous work had shown molybdenum to be ineffective, further study was halted. Therefore, the next stage of the project was carried out on $Al_2O_3/Cu/MoSi_2$ and $Si/SiO_2/Cu/MoSi_2$ multilayers. Both copper and $MoSi_2$ were sputter deposited.

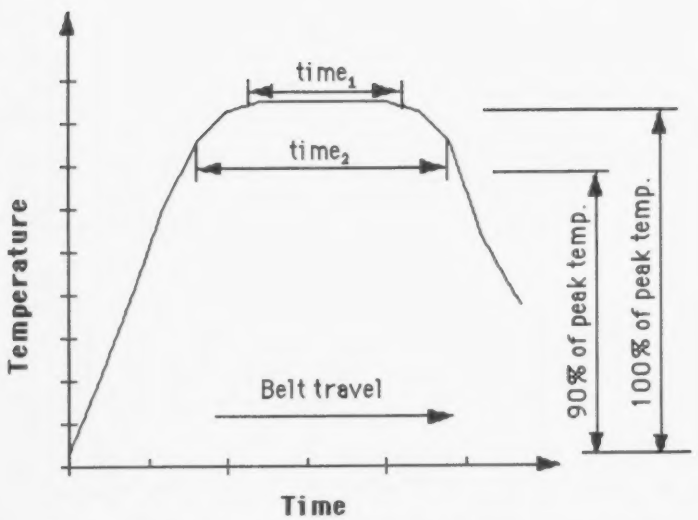

Figure 5-1: Illustration of the 100% and 90% line nomenclature. Not to scale.

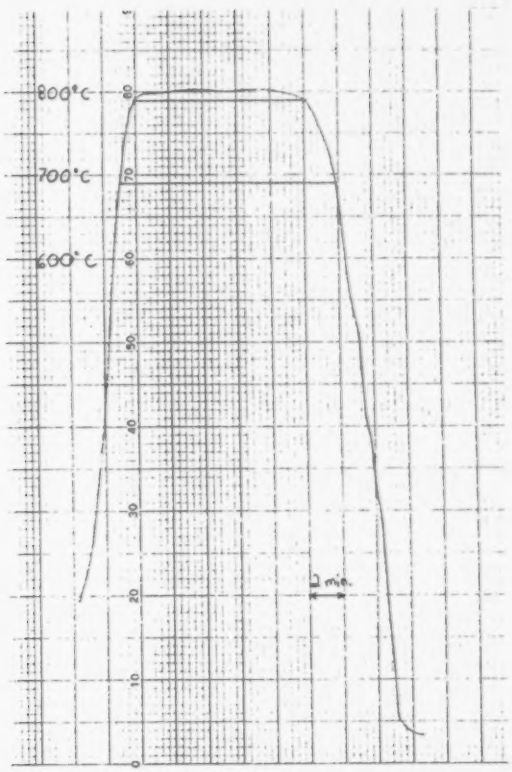

Figure 5-2: The typical firing profile shape. 800°C with 10 minutes peak time. Full scale is 1000°C, chart speed 30cm/hr.

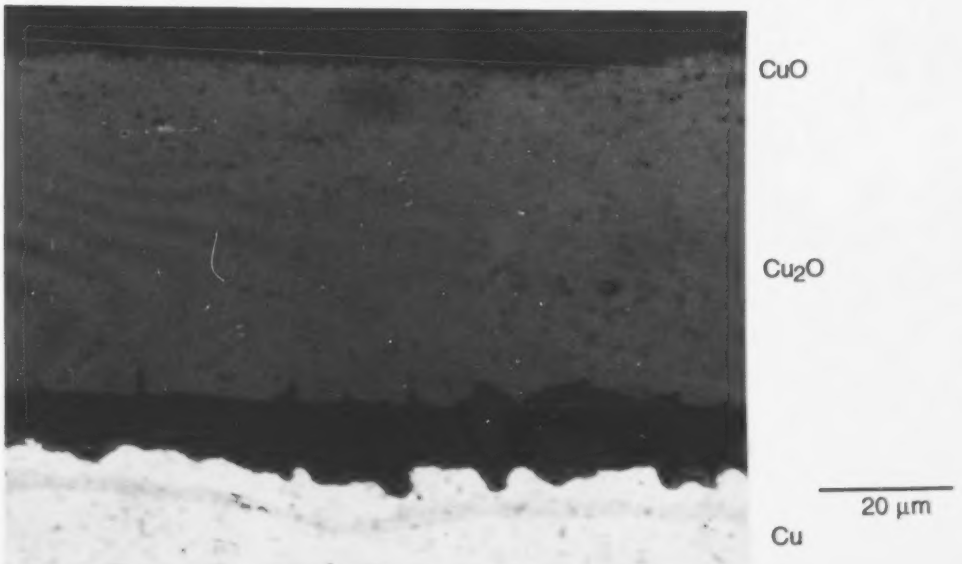

Figure 5-3: Optical micrograph of the oxide on bare copper. 800°C for 15 minutes.

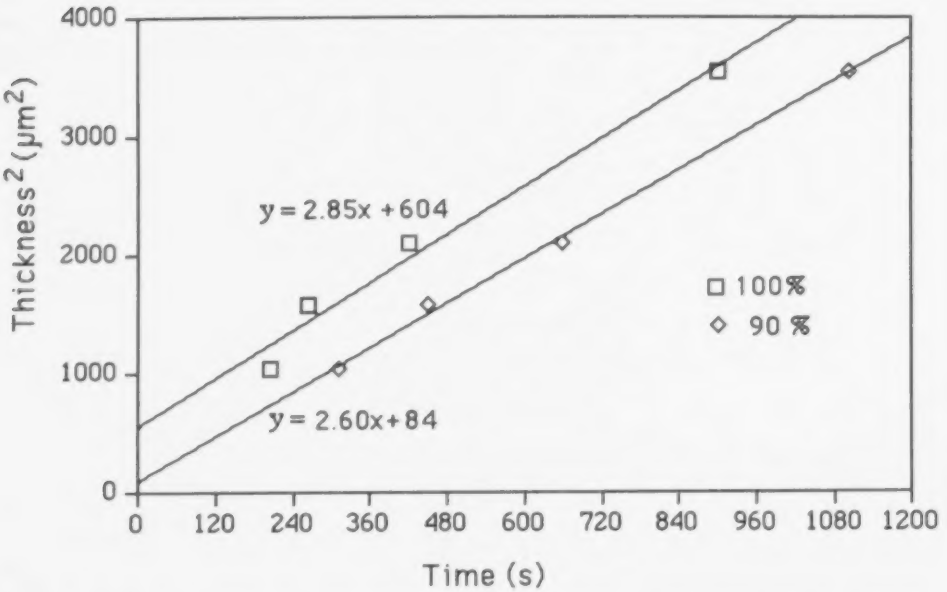

Figure 5-4: A plot of thickness squared vs. time for the oxidation of bare copper. 100% and 90% peak temperature data are shown for 850°C.

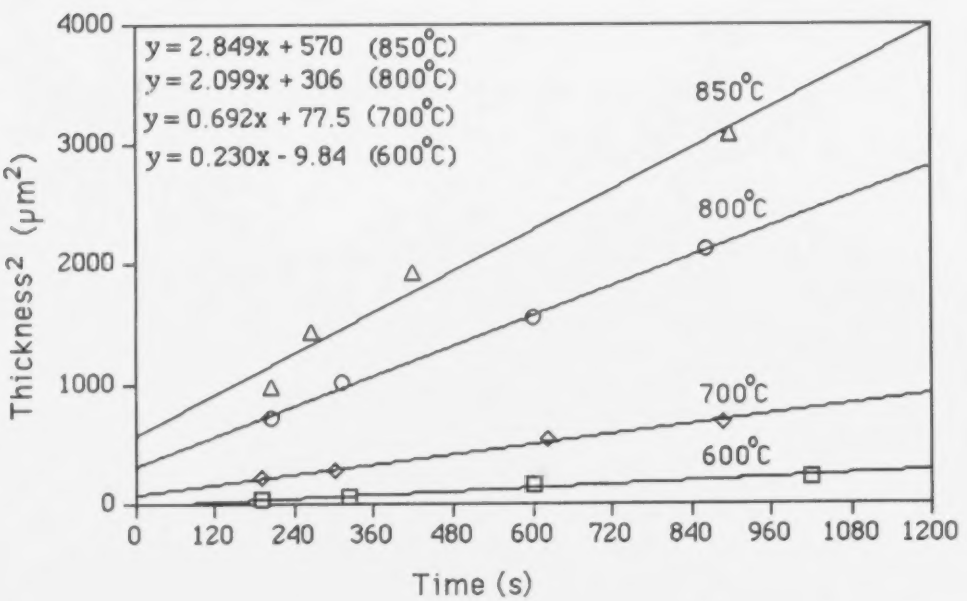

Figure 5-5: A plot of thickness squared vs. time for the oxidation of bare copper for 600, 700, 800, and 850°C. 100% peak temperature data are shown.

Table 5-1: A comparison of the parabolic rate constant of bare copper from the literature [11,31] and this experiment.

Temp (°C)	Literature $k_p(cm^2/s)$ $x10^{-8}$	Experimental 100% peak temp $k_p(cm^2/s)x10^{-8}$	r^2	Oxide thickness at 15min. (μm)	Copper consumed at 15 min (mg),(μm)
850	2.86-2.82	2.85	0.971	56.0	30.4,(34.1)
800	1.175-0.733	2.10	0.997	46.9	25.4,(28.6)
700	0.316-0.123	0.692	0.991	26.5	14.4,(16.2)
600	0.145-0.0153	0.230	0.969	14.1	7.60,(8.60)

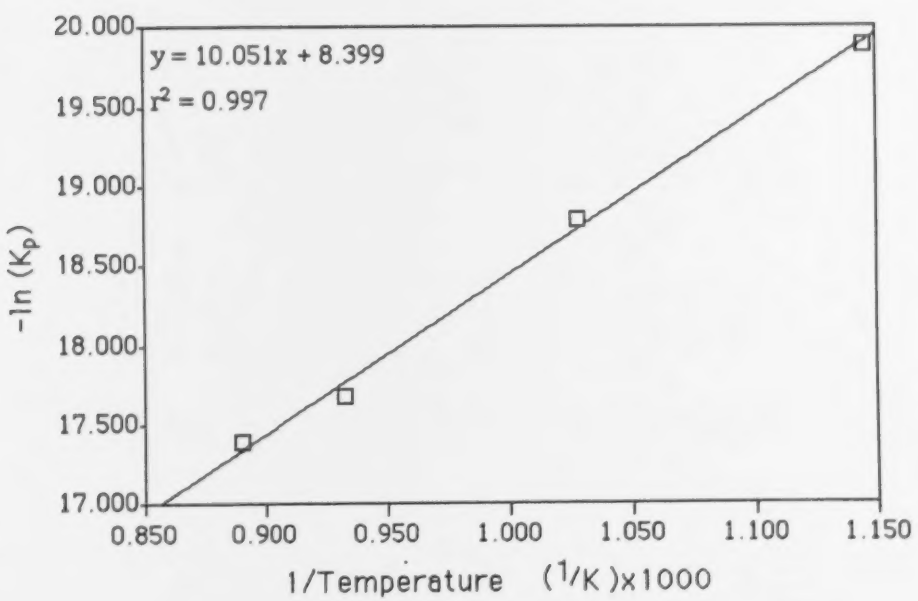

Figure 5-6: Arrhenius plot of the experimental rate constants. The slope is proportional to the effective activation energy of copper. Q_{app} = 83.6 kJ/mol.

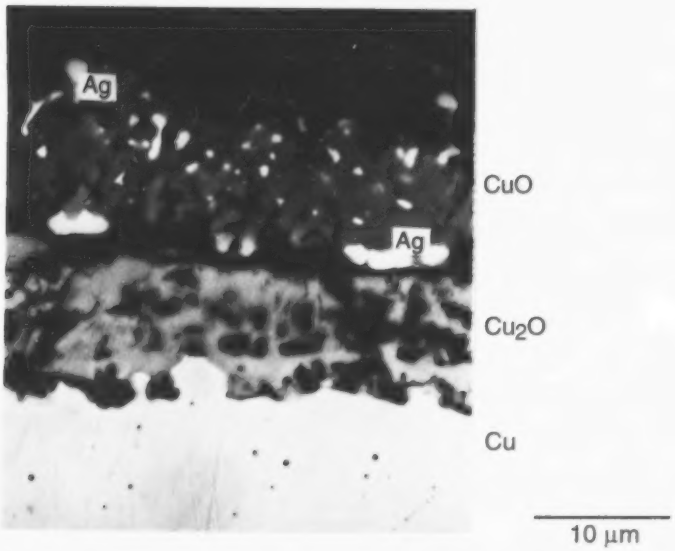

Figure 5-7: SEM backscattered electron image of sample Cu(Sub)/ Cu(5000nm)/$MoSi_2$(150nm)/Ag(1000nm). Annealed at 700°C for 10 min.

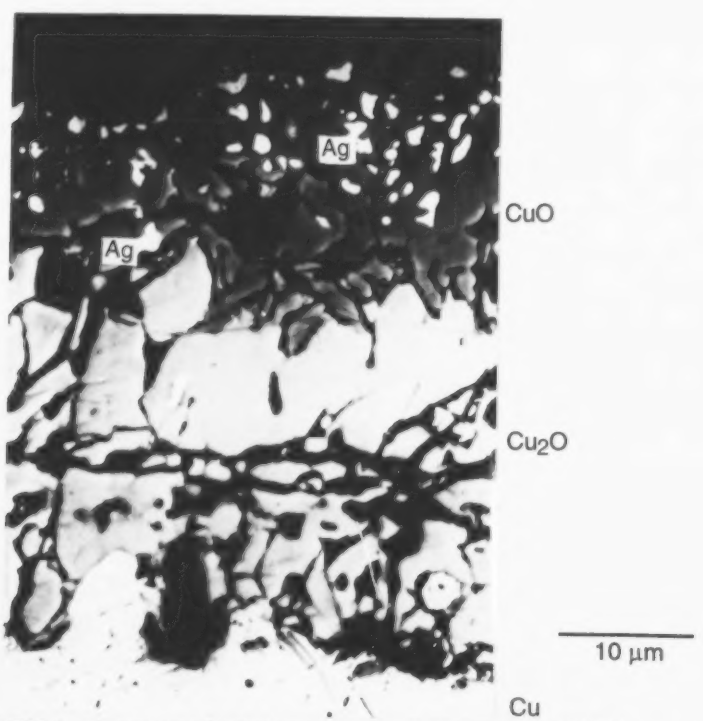

Figure 5-8: SEM backscattered electron image of sample Cu(Sub)/ Mo(200nm)/Ag(1000nm). The sample was annealed at 800°C for 10 min.

5.3 $MoSi_2$(200nm) Barrier Layer for Copper.

Multilayer metallizations on silicon and alumina substrates were investigated. Anneals in air at temperatures of 600°C, 700°C, 800°C, and 850°C were carried out. Thin film copper and $MoSi_2$ layers were deposited onto an oxidized substrate of silicon or alumina by magnetron sputtering. Sputtering the $MoSi_2$ using this technique forms an amorphous $MoSi_2$ layer on top of the copper. The different substrates were used to facilitate characterization depending on the type of analysis needed. Alumina substrates were used for thermal gravimetric analysis. Silicon subtrates were used to facilitate transmission electron microscopy sample preparation. Other techniques such as atomic force microscopy, scanning electron microscopy and X-ray diffraction were done on both substrate types. SiO_2 was grown on the surface of silicon because ~12 at% silicon dissolves in copper at 850°C.

5.3.1 Film Uniformity and Integrity (Surface Analysis)

Atomic force microscopy was used to determine the local roughness of the as deposited films for $MoSi_2$(100nm) and $MoSi_2$(200nm), on silicon and alumina. Figures 5.9a and 5.9b illustrate the difference between Al_2O_3/Cu/$MoSi_2$(100nm) and Si/Cu/$MoSi_2$(100nm) samples, respectively. It is assumed that the roughness of the substrate material has an effect on the roughness of the deposited films, i.e., the coarseness (or smoothness) of the substrate is translated to the film surface. The grey scale in the top left corner is normalized to the lowest and highest points in the AFM scan, this scale is only a coarse indication of overall roughness since a non-level surface may exaggerate the scale range. The scale, on the left side of the micrographs, ranges from 0-1466nm and 0-261nm for the 100nm films on alumina and silicon substrates respectively. This gives an initial indication that the films deposited on the alumina substrates are relatively rougher than the films deposited on the silicon substrates. Rougher sufaces with steep sides can produce shadowing effects and reduce a coating's uniformity and ultimately its usefulness. Line scans of Figure 5-9a (Al_2O_3/Cu/$MoSi_2$(100nm)) indicate that the depressions (dark areas) are 400nm to 600nm deep, indicating there might be breaks in film integrity, exposing the underlying copper. Lines scans from Figure 5-9b (Si/Cu/$MoSi_2$(100nm)) show variations slightly greater than 100nm, which also indicate the dark (1-3μm^2) areas are holes in the film, reducing the effectiveness of $MoSi_2$ as a diffusion barrier.

Figures 5-10a and 5-10b are AFM scans of as deposited Al_2O_3/Cu/$MoSi_2$(200nm) and Si/Cu/$MoSi_2$(200nm) samples respectively. The scales range from 0-1260nm and 0-223nm respectively. Again, the films on the silicon substrates are significantly smoother than those on the alumina substrates. Line scans of Figure 5-10a (Al_2O_3/Cu/$MoSi_2$(200nm)) also show depressions that are 400nm to 600nm deep. The line scans of Figure 5-10b (Si/Cu/$MoSi_2$(200nm)) sample show a variation of <100nm from peak to peak. This is one half of the deposited film thickness indicating no breaks in the film. The AFM scans from Figures 5-9 and 5-10 are representative of the overall surfaces of the as deposited films. Optical micrographs were taken from the same samples as the AFM scans, but at a lower magnification (not shown). They confirm the general trends from the AFM line scans, i.e., the films on the alumina substrates are rougher than those deposited on the silicon substrates, and the thicker $MoSi_2$ films show better film continuity than the thinner films. By continuity it is meant that the films show fewer pin holes or breaks in the surfaces.

Coors' specifications for ADS-996 alumina gives a surface finish of ~75nm (Ra value) as fired for the polished side. An Ra value is determined from a centre line which is calculated such that the areas above and below this line are equal. The heights above and below the centre line are then averaged to quantify the Ra number. Ra values for the as received alumina and the grown SiO_2 on silicon were measured using the AFM. Typical Ra values for alumina and SiO_2 on silicon were 160nm and 12nm respectively. The oxidized silicon is one order of magnitude smoother than the alumina. The improved smoothness of silicon over alumina is obvious when one considers the grain sizes of each. The silicon wafers being used were single crystal and therefore have no grain boundaries and are polished to a mirror finish. The alumina substrates were a sintered compact with a grain size of ~1.2μm. Polishing of the surface may have made the roughness worse in some areas because of grain pullouts, i.e., regions with steep edges perpendicular to the surface causing shadowing effects. Therefore it is expected that the best film uniformity and continuity would be obtained from the smoother silicon substrates. On the other hand, copper adhesion to the surface of alumina could be expected to be better due to mechanical bonding with the rougher surface. Copper does not adhere well to SiO_2 and since the surface is very smooth, adhesion can be expected to be relatively poor.

Figure 5-11a and 5-11b are SEM secondary electron images of plan view samples of Cu/$MoSi_2$(200nm) on alumina and silicon respectively. From XRD and TEM analysis (detailed later), it is shown that the $MoSi_2$ is amorphous upon deposition. The amorphous $MoSi_2$ tends to agglomerate on the surface during depostion. This is more noticeable on the samples deposited on silicon and can be seen as bright circles in Figure 5-11b, the larger hillocks measuring 0.3μm in diameter. In Figure 5-11a, the $MoSi_2$ film conforms with dimensions roughly of the same order as the underlying grainsize of the alumina substrate (~1.2μm). It forms a relatively rough surface possibly exposing the underlying copper in places. Comparison of these two SEM images with the AFM scans in Figure 5-10a and 5-10b, which are the same samples, shows there is a very good topographical correlation.

Figure 5-12a-d shows a series of secondary electron SEM images for a nominal time of 10 minutes at 600°C, 700°C, 800°C and 850°C taken from Al_2O_3/Cu/ $MoSi_2$(200nm) samples. An oxygen peak was present from the EDX analysis of the surface in Figure 5-12a (600°C for 10 minutes). At this stage copper has diffused through the $MoSi_2$ layer to the surface and has formed a thin oxide coating. This image suggests a structure similar to the as deposited structure in Figure 5-11a, indicating the oxide is very thin. In Figure 5-12b (10 minutes at 700°C), the oxide has formed a needle-like 3-dimensional network over the entire surface. At 800°C for 10 minutes, (Figure 5-12c), the oxide is denser and compact. In the last sample, annealed at 850°C for 10 minutes (Figure 5-12d), a dense oxide has formed on the surface with a particle size of ~2 μm to ~3μm.

Figure 5-13a-d shows a series of secondary electron SEM images for a nominal time of 10 minutes at 600°C, 700°C, 800°C and 850°C taken from Si/Cu/ $MoSi_2$(200nm) samples. This series is similar to the films deposited on alumina in Figure 5-12. EDX spectra taken from the surface of the sample annealed at 600°C for 10 minutes in Figure 5-13a indicates oxygen is present. As with the alumina sample for the same time and temperature, the underlying as deposited $MoSi_2$ structure is still visible, thus any oxide that has formed is very thin. For the sample annealed at 700°C for 10 minutes, (Figure 5-13b), EDX analysis showed copper oxide present over the entire surface. The oxide is quite porous and the initial stages of oxidation formed a 3-dimensional network on top of the $MoSi_2$ layer. The next sample is Figure 5-13c (800°C for 10 minutes), which shows a 3-dimensional oxide network that has become more dense. At 850°C for 10 minutes (Figure 5-13d) the oxide has formed a dense

uniform coating over the entire surface with a particle size of ~4μm to ~5μm. Oxide growth kinetics and oxide thicknesses of pure copper will be discussed later, but it is noted here that at 600°C for 10 minutes, 2 microns of copper (the thickness of the layer used for these samples) would have completely reacted with oxygen to form a copper oxide duplex layer (i.e., Cu_2O and CuO), and this is not the case with the $MoSi_2$ barrier coated samples for either the films on alumina or silicon.

Further surface analysis of different times for several temperatures was completed for the Si/Cu/ $MoSi_2$(200nm) samples. A progression of oxide growth can be seen as the annealing time is increased for a given temperature, except for the samples annealed at 850°C. The surface morphology at 2 minutes was similar to the 10 minute sample at 850°C. Since the diffusion of copper through the $MoSi_2$ layer is exponentially dependent on annealing temperature, significantly more oxide had formed on the surface at the 850°C temperature. During the initial stages of oxide growth the grain size increased as the oxide thickness increased.

5.3.2 X-ray Diffraction Analysis

X-ray diffraction was completed for the Cu/$MoSi_2$(200nm) samples for alumina and silicon substrates. Figures 5-14 and 5-15 show XRD spectra for 700°C and 800°C temperatures respectively, annealed for 2, 5, and 10 minutes, as well as the as deposited sample. "X" marks an alumina peak; others are labelled accordingly. The most intense peaks for copper and alumina both correspond to the same 2-theta position, at 43.3°. At 95.1° copper and alumina share another peak, and at 89.9° copper and CuO share a peak. Some peaks are off scale in a few spectra, but where this is the case the number beside the peak indicates its intensity. In Figure 5-14a, the as deposited spectrum shows peaks corresponding to copper and alumina only. This would indicate $MoSi_2$ is amorphous or is too thin to be detected. All intensity axes were reduced to 1000 counts full scale to bring up the small oxide peaks from the background. In Figure 5-14, there is a slight decrease in the copper peaks at 43.3° and 50.4° as the time increases. There are no copper oxide peaks until 700°C - 10 minutes, whereupon small CuO peaks are visible. Figure 5-15 shows XRD spectra of Al_2O_3/Cu/$MoSi_2$(200nm) annealed at 800°C. Copper peaks decrease as annealing time increases and CuO peaks increase with annealing time. The peaks at 43.3° for 800°C at 5 and 10 minutes have the same intensity, most likely corrosponding only to alumina. Similarly the other less

intense peaks shared between copper and alumina, and copper and CuO do not correspond to copper. It is noteworthy that there is no evidence of Cu_2O for any of these two series.

Figures 5-16 and 5-17 show XRD spectra for 700°C and 800°C respectively for the Si/Cu/$MoSi_2$(200nm) system. The as deposited Si/Cu/$MoSi_2$ (200nm) spectrum shows only peaks corresponding to copper. hkl planes corresponding to each peak are given in round brackets. There were no peaks for the $MoSi_2$ layer or the underlying silicon substrate. There is also a slight <111> preferred orientation in the direction perpendicular to the substrate for as deposited copper. In Figure 5-16, the intensity of copper does not show any trend. However, there are traces of CuO for all times. Figure 5-17 shows the spectra for 800°C. Copper peaks decrease in intensity with time and at 10 minutes there are no copper peaks present, whereas CuO increases with time. There is a small Cu_2O peak at 2 minutes, but this has disappeared for the other times, otherwise CuO is the only oxide present. A comparison of the XRD spectra between films annealed on alumina with those annealed on silicon substrates shows that the trends and even the intensities of CuO are similar for their corresponding times and temperatures. The two differences were the preferred <111> orientation of copper on silicon and the presence of the small Cu_2O peak for the Si/Cu/$MoSi_2$ sample annealed at 800°C for 2 minutes.

5.3.3 Oxide Phase Identification

The oxide that formed on the surface of the $MoSi_2$ was identified by XRD to be CuO with virtually no Cu_2O except for one small anomaly at 800°C for 2 minutes. From oxidation studies done on bare copper, it might be expected that Cu_2O would form with varying amounts of CuO depending on the temperature, but this was not the case for the coated copper samples. The driving force for copper to diffuse through $MoSi_2$ to the surface is the decrease in free energy from the formation of copper oxide. However, since there is a limited amount of copper on the surface, it is more favourable for one copper atom, instead of two, to pair with one oxygen atom, to form CuO. Dravnieks [123] has found that for the oxidation of copper in air, that CuO is nucleated first when the ratio of copper ions to oxygen supply at the outer film surface falls below a certain value. This finding is in agreement with the results for the $MoSi_2$ coated copper samples.

TEM-EDX analysis of the annealed samples showed that the layer on top of the $MoSi_2$ contained only copper. Figure 5-18 shows a TEM cross section of a Si/Cu/$MoSi_2$(200nm) sample annealed at 700°C for 10 minutes. The SAD pattern from the top layer, labelled CuO, was indexed as copper. This discrepancy is due to a reduction process that took place during TEM sample preparation. One of the steps of TEM sample preparation is ion milling. The sample is exposed to a vacuum of $<5x10^{-5}$ torr and an argon beam of 4kV energy is focused onto a thin ~0.1mm^2 area of the sample. An order of magnitude calculation was made for the radiation damage by ion milling based on calculations taken from Ivey and Piercy [124] (Appendix C). It can be shown that the Ar^+ beam can impart enough kinetic energy to CuO to reduce it to metallic copper. It can be seen in Figure 5-18b that the reduced CuO is porous, which may be the result of the reduction process and corresponding loss of oxygen. To test this hypothesis, plan view TEM samples were made and ion milled from one side only for one tenth of the time. Figures 5-19a and 5-19b show a bright and dark field image of CuO, which was typical for the sample. Figure 5-19c shows regions of Cu_2O present in the CuO matrix. The corresponding SAD ring patterns are given in Figures 5-19d and 5-19e respectively. Both patterns contain CuO which has an average grain size of ~250 nm. The aperture used did not enclose a large number of grains; therefore the CuO rings are not continuous. On the other hand, the Cu_2O rings in Figure 5-19e, are more continuous and correspond to the smaller grained Cu_2O. Other evidence for the reduction of CuO in a vacuum has been reported by Li and Mayer [125]. Reducing CuO in a vacuum of $2x10^{-7}$ torr at 550°C to 680°C leads to the formation of Cu_2O grains in a CuO matrix. Cu_2O grains grow in isolation and the morphology was found to be discontinuous, i.e., not all the CuO grains transform to Cu_2O simultaneously. They proposed that the discontinuous morphology of grain growth of Cu_2O is due to the migration of the Cu_2O-CuO phase boundary induced by oxygen diffusion along the moving phase boundary [124]. Also the reduction rate was found to be faster in thin film samples than bulk samples because of smaller grain sizes. The grain boundaries provide easy paths for oxygen out-diffusion resulting in a lower phase transformation temperatures in thin film samples. It is noteworthy that Cu_2O was detected at 700°C at 5 minutes but not in large amounts. There are two possible explanations for this. One is that even though the ion energy was reduced, locally there was sufficient energy to reduce some of the CuO to Cu_2O. The other explanation, which corroborates the XRD result, is that there are small amounts of Cu_2O forming in the CuO matrix. The amounts that form are close to the detection limit of the XRD analysis and do not show up consistently.

Cross-sectional TEM samples were made to identify the phases and the oxides present before and after the anneals. All TEM cross-sections were made from films deposited on thermally grown SiO_2 on silicon. Figure 5-20 shows a TEM bright field micrograph of an as deposited Si/Cu/$MoSi_2$(200nm) sample, and its corresponding SAD pattern and EDX spectrum from the $MoSi_2$ layer. The diffuse ring in Figure 5-20b indicates that the $MoSi_2$ is amorphous upon deposition. This agrees with the absence of $MoSi_2$ peaks in the as deposited XRD spectra. Figure 5-20c verifies that the layer contains only molybdenum and silicon. The $MoSi_2$ layer is continuous and is ~200nm thick. Although the entire copper cross-section cannot be seen in this micrograph, it is ~2μm in thickness, also matching its nominal value. A pinhole in the $MoSi_2$ is present at the bottom left corner of Figure 5-20a.

Figure 5-21a shows a TEM cross-section of Si/Cu/$MoSi_2$(200nm) annealed at 600°C for 5 minutes. Figures 5-21b, 5-21c, and 5-21d show corresponding EDX spectra taken from the oxide, the $MoSi_2$, and the copper within 100nm of the Cu/$MoSi_2$ interface, respectively. Small amounts of oxide with an average thickness of 35nm can be seen on the surface of the $MoSi_2$. The spectrum in Figure 5-21b taken from the oxide layer has only copper peaks present. The absence of oxygen is a result of the reduction of the oxide to metallic copper, which was discussed above. In Figure 5-21c, molybdenum and silicon are present as well as significant amounts of copper. Copper diffuses through the $MoSi_2$ layer to the surface to form CuO. A semiquantitative analysis of the peak intensities indicates that the silicon to molybdenum ratio is less than 2:1. Comparison of this spectrum with the as deposited spectrum (Figure 5-20c), clearly shows that the silicon to molybdenum ratios are not the same. Silicon from the $MoSi_2$ layer diffuses into the copper (12 at% silicon is soluble in copper at 850°C). In Figure 5-21d, there is a small amount of silicon present, at 1.6 keV, which accounts for the lost silicon in the previous spectrum. Additional peaks in the spectrum include carbon, which is a result of contamination during the analysis. Iron and chromium peaks also appear because sputtered material from the stainless steel cathode guns is deposited onto the sample during sample preparation.

Figure 5-22a shows a TEM cross-section of the Si/Cu/$MoSi_2$(200nm) sample annealed at 800°C for 2 minutes. Figure 5-22b, 5-22c, and 5-22d, are corresponding EDX spectra taken from the oxide layer, the $MoSi_2$, and the copper layer close to the Cu/$MoSi_2$ interface, respectively. For the sample annealed at 800°C for 2 minutes, the

oxide layer has grown to an average thickness of about 600nm. This series of EDX spectra are similar to the previous ones at 600°C. Oxygen peaks are missing from the spectrum taken from the CuO layer in Figure 5-22b. In Figure 5-22c, the amount of silicon in the $MoSi_2$ is less than stoichiometric because it is diffusing into the underlying copper. Copper peaks are present because of its diffusion to the surface. In Figure 5-22d, the spectrum collected from the copper layer close to the $MoSi_2$/Cu interface has a small silicon peak, accounting for the silicon from the $MoSi_2$ diffusing into the copper.

5.3.4 Kinetics of Oxidation

Oxidation kinetics were quantified by taking thickness measurements of the oxide that had grown on the surface of the $MoSi_2$ layer. A minimum of 20 measurements, and as many as 50, were taken at random locations along the oxide. An average value was calculated along with the standard deviation. Cross-sections were made for either the SEM or TEM depending on the oxide thickness. Since SEM samples are quicker and easier to prepare, whenever possible the SEM was employed. The practical resolution limitation for these samples was an oxide thickness that was greater than ~250nm. Thicknesses smaller than this could not be resolved with confidence. A comparison of a Si/Cu/$MoSi_2$(200nm) sample imaged in both the SEM and TEM is shown in Figures 5-23a and 5-23b, respectively. Thickness measurements from the respective oxides and $MoSi_2$ layers are in good agreement with each other. Samples prepared for the SEM undergo the same initial preparation as the TEM, but dimpling and ion milling are not necessary. Therefore, the oxide has not been reduced in SEM samples. This is reflected in the differences in the porosity of the two samples; the TEM sample is more porous.

Cross-sections annealed at 600°C, 700°C, 800°C, and 850°C were prepared. All samples showed a trend of increasing oxide thickness with time for a given temperature, except for the 850°C series which fluctuated between 3.4μm and 3.7μm. Figure 5-24 is an SEM secondary electron image of a Si/Cu/$MoSi_2$(200nm) sample annealed at 850°C for 5 minutes. It is representative of all the 850°C samples. The underlying copper is missing in places which suggests the oxide thickness stopped growing as the copper became depleted locally. Therefore no kinetic data was obtained for the samples annealed at 850°C. The same figure also indicates that $MoSi_2$ remained continuous even though it did not remain planar. The grain size of the oxide is in good

agreement with the plan view SEM image of the Figure 5-13d.

Kinetic data was calculated for the remaining three temperatures. Thickness measurements were taken and plotted as thickness squared vs. time. The slope of the best fit straight line for the parabolic plot gives the parabolic oxidation constant k_p. Figure 5-25 shows thickness squared vs. time graphs at 800°C, 700°C and 600°C. The raw data is given in Appendix D. The error bars for each point are indicated; otherwise they are contained within the size of the data marker. The coefficient of determination (r^2) is 0.968 for 800°C, 0.985 for 700°C, and 0.946 for 600°C. The x intercept, which is the incubation time during which the first copper atoms take to diffuse through the $MoSi_2$ to the surface, decreases as the temperature increases. The incubation time is 166 seconds for 600°C, 155 seconds for 700°C, and 132 seconds for 800°C. Figure 5-26 shows the data for thickness measurements plotted on a log scale along with the values for bare copper from this work. The left axis is thickness squared in nm^2 and taken from the parabolic plots. The right axis is the thickness in μm and can be used to visually compare the order of magnitude improvement of the coated samples over the bare copper samples. Figure 5-27 is an Arrhenius plot of the parabolic rate constants. The apparent activation energy for the oxidation process for copper coated with 200nm of $MoSi_2$ is 215kJ/mol, compared to 83.6kJ/mol for bare copper under the same annealing conditions.

The oxide that formed on the surface of the coated samples was entirely CuO, compared with bare copper which was almost entirely Cu_2O. Since the oxide that forms is different, another way of comparing the oxidation kinetics was by calculating the amount of copper consumed. The parabolic rate constants, activation energy, and the oxide thickness for 15 minutes are tabulated for the coated samples and for bare copper in Table 5-2. Also included is the amount of copper that was consumed for a time of 15 minutes for both types of samples. Since the densities of the two oxides differ by only 0.4 g/cm^3 there is not much difference when comparing the improvement by thicknesses or by amount of copper consumed. The improvement factor for the rate constant is related to the improvement factor for the thickness. Since the thickness is proportional to the rate constant squared, the improvement for the thickness is roughly the square root of the k_p value. Therefore the various improvement factors are related and can be converted from one to the other with the appropriate factors. When comparing the coated samples with bare copper, the improvement factor for the amount of copper consumed is quoted. The copper consumed is reduced by ~145 x at 600°C, ~50 x at 700°C, and ~35 x at 800°C for a 200nm coating of $MoSi_2$.

5.3.5 Thermal Gravimetric Analysis (TGA)

To quantify the kinetics of the oxdiation, thermal gravimetric anaylsis was attempted. This analysis technique proved to be problematic. Initially it was thought that samples could be ramped up to the peak temperature in an inert gas. Air would be introduced into the furnace chamber and the mass gain would be recorded as a function of time. The data could then be used to determine a rate constant for the oxidation and this would be compared to the thickness measurement data from the TEM analysis. This was not the case. Some unexpected problems arose while performing the TGA. TGA was carried out on films that were deposited onto alumina substrates. Square samples measuring 6.35mm x 625μm thick were tried, making the total weight of the sample >100mg. The TGA could not be tared and the sensitivity of the balance was a function of the total weight of the sample. Therefore, to come close to the theoretical sensitivity of ~10μg, a total mass <20mg was needed. It was decided to thin the alumina substrate to <100μm, which corresponds to a mass of ~17mg. A Gatan disk grinder was used. Once the sample was mounted on an adjustable stage with low melting point wax, it was accurately thinned on a diamond grinding wheel to within 10μm of the desired target thickness.

A fast 50^{o}/min ramp rate was used causing convection currents, labelled 'cc' in Figure 5-28, which initially introduced noise into the system. The noise dissipated quickly once the peak temperature was reached. A problem was observed from the TGA plot during the ramp up to peak temperature in argon. Archimedian buoyancy effects on the sample due to changes in the density of argon caused the balance to record a mass gain. This effect can be seen in Figures 5-28 labelled 'b' for buoyancy. Initially the gas change from the Ar to air was done as soon as the temperature reached the desired test temperature, but due to buoyancy and convection currents still in the furnace cylinder, erroneous readings were recorded (not shown here). Therefore a >20 minute delay was necessary at the peak temperature in Ar, to allow the balance to reach equilibrium.

Another problem was noted during the delay period, prior to gas exchange. The mass of the sample did not reach an equilibrium plateau as expected, indicating there was some oxygen uptake in the argon atmosphere. The preceding 20-30 minutes prior to the argon/air gas changeover was expected to have zero mass uptake. This was not the case; the slope increased with temperature during this period, which indicated the presence of oxygen, since the oxidation rate (the mass gain) is a function of temperature. This also

explains the behaviour in Figure 5-28d. All the copper had oxidized during the initial ramp up and wait period, so that there was zero mass gain (other than buoyancy effects) when the air was admitted to the system. Therefore, only electron microscope thickness measurements were used to quantify kinetics.

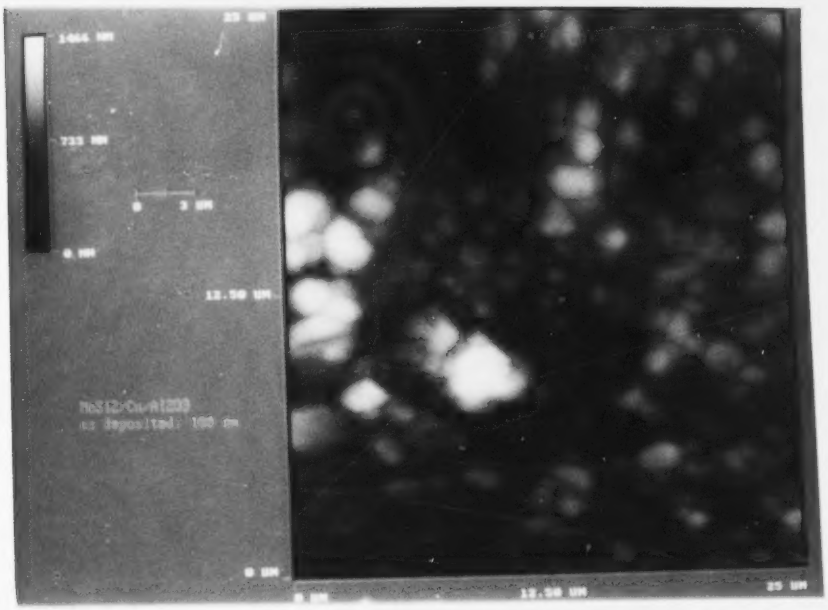

Figure 5-9a: AFM 25μm scan of Al_2O_2/Cu/$MoSi_2$(100nm) as deposited sample.

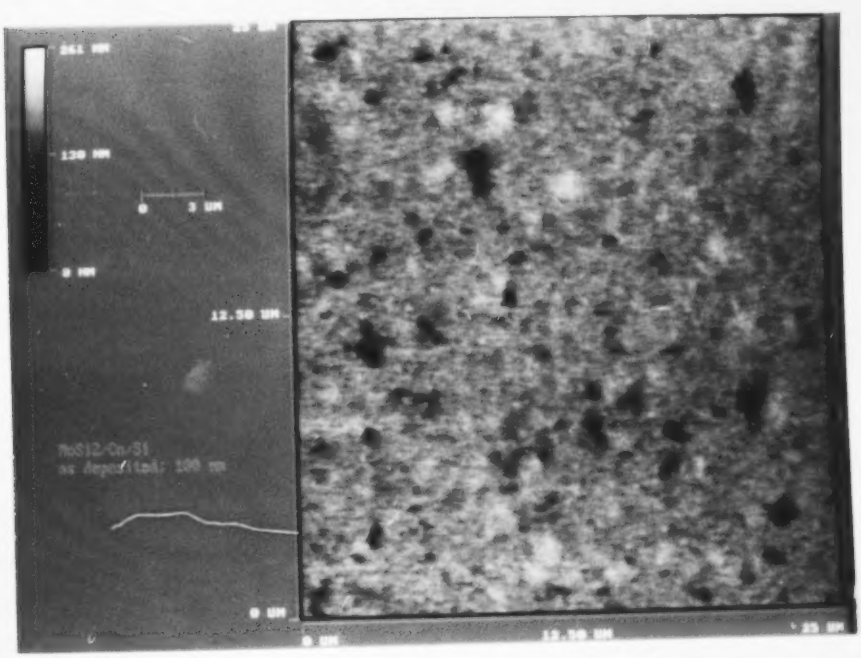

Figure 5-9b: AFM 25μm scan of Si/Cu/$MoSi_2$(100nm) as deposited sample.

Figure 5-10a: AFM 25μm scan of Al_2O_2/Cu/$MoSi_2$(200nm) as deposited sample.

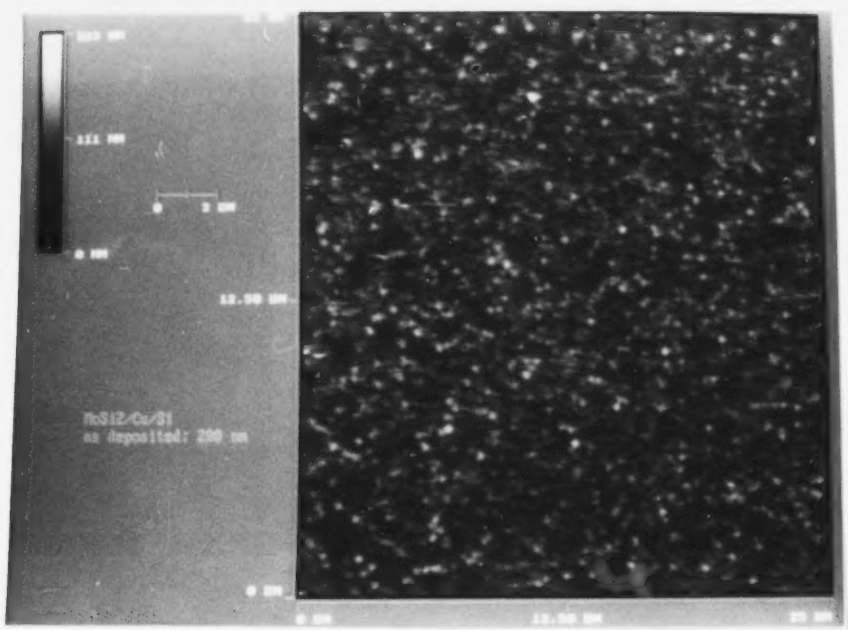

Figure 5-10b: AFM 25μm scan of Si/Cu/$MoSi_2$(200nm) as deposited sample.

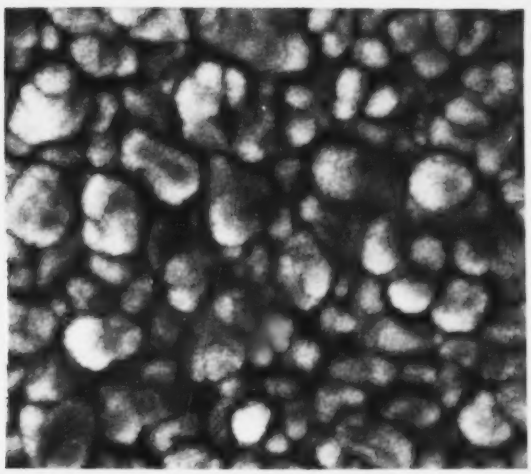

3 μm

Figure 5-11a: SEM secondary electron image of as deposited Al_2O_2/Cu/$MoSi_2$(200nm) sample.

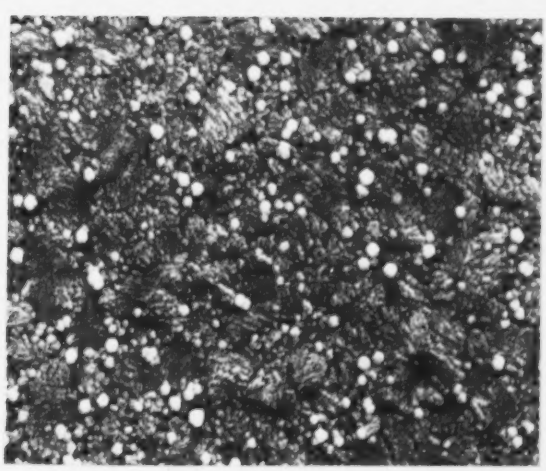

3 μm

Figure 5-11b: SEM secondary electron image of as deposited Si/Cu/$MoSi_2$(200nm)sample.

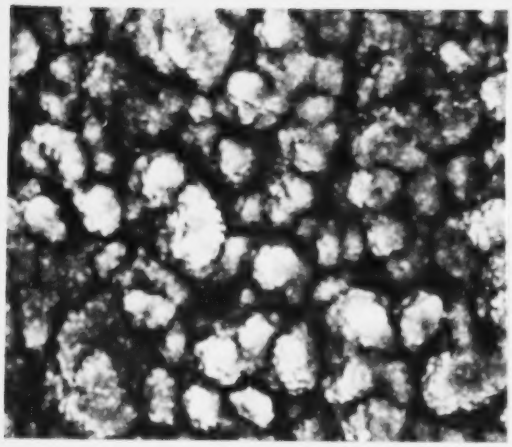

a) Annealed at 600°C for 10 min.

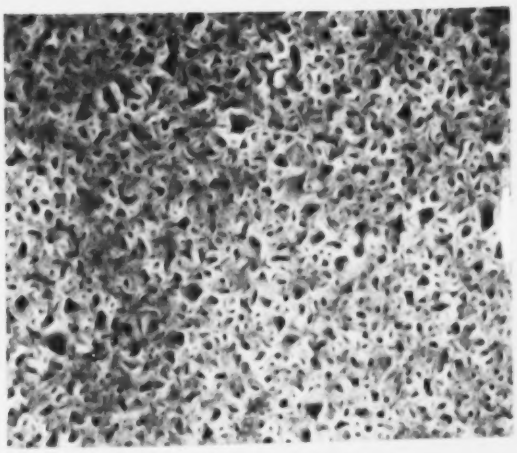

b) Annealed at 700°C for 10 min.

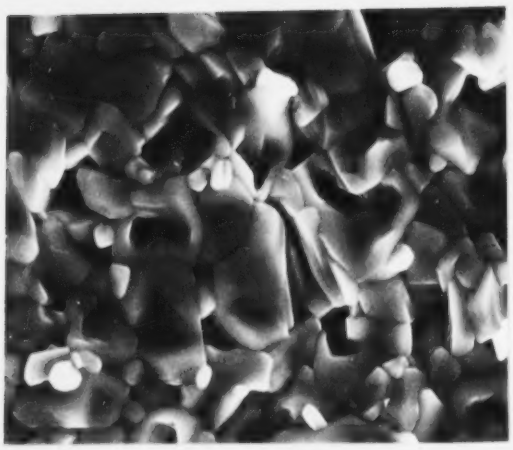

c) Annealed at 800°C for 10 min.

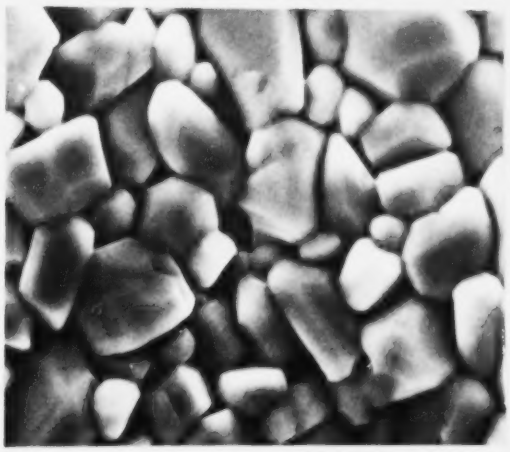

d) Annealed at 850°C for 10 min.

Figure 5-12: SEM secondary electron images of Al_2O_3/Cu/$MoSi_2$(200nm) samples.

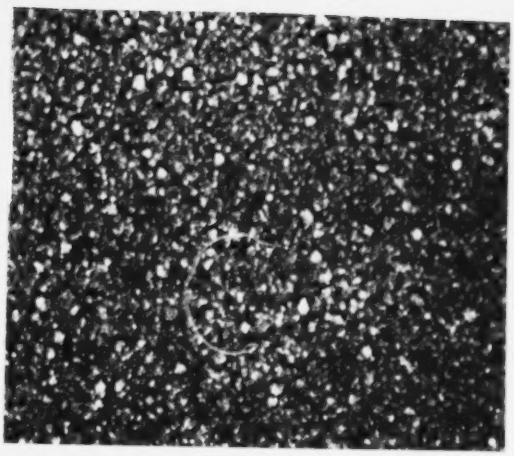

a) Annealed at 600°C for 10 min.

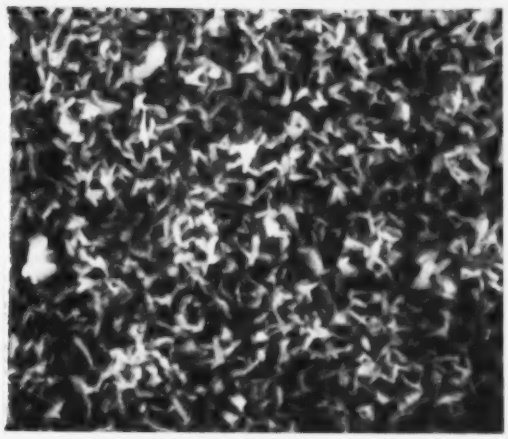

b) Annealed at 700°C for 10 min.

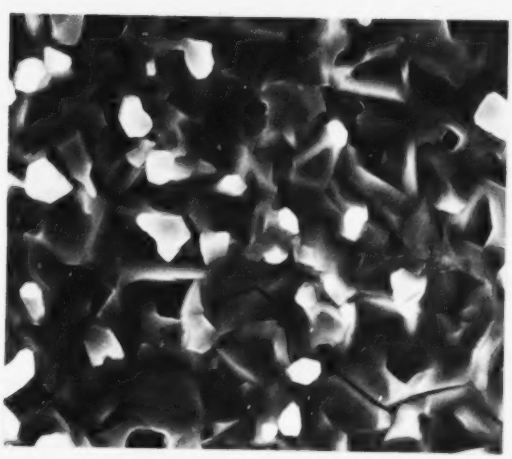

c) Annealed at 800°C for 10 min.

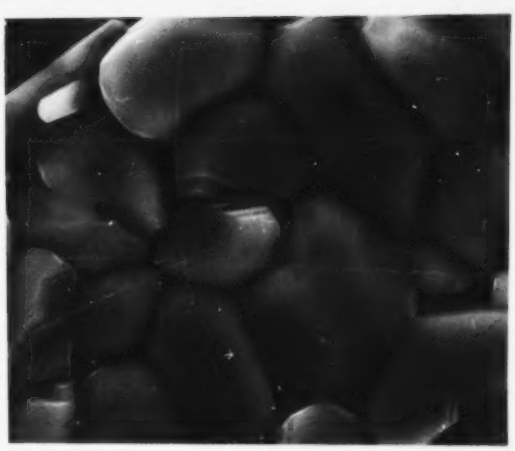

d) Annealed at 850°C for 10 min.

Figure 5-13: SEM secondary electron images of Si/Cu/$MoSi_2$(200nm) samples.

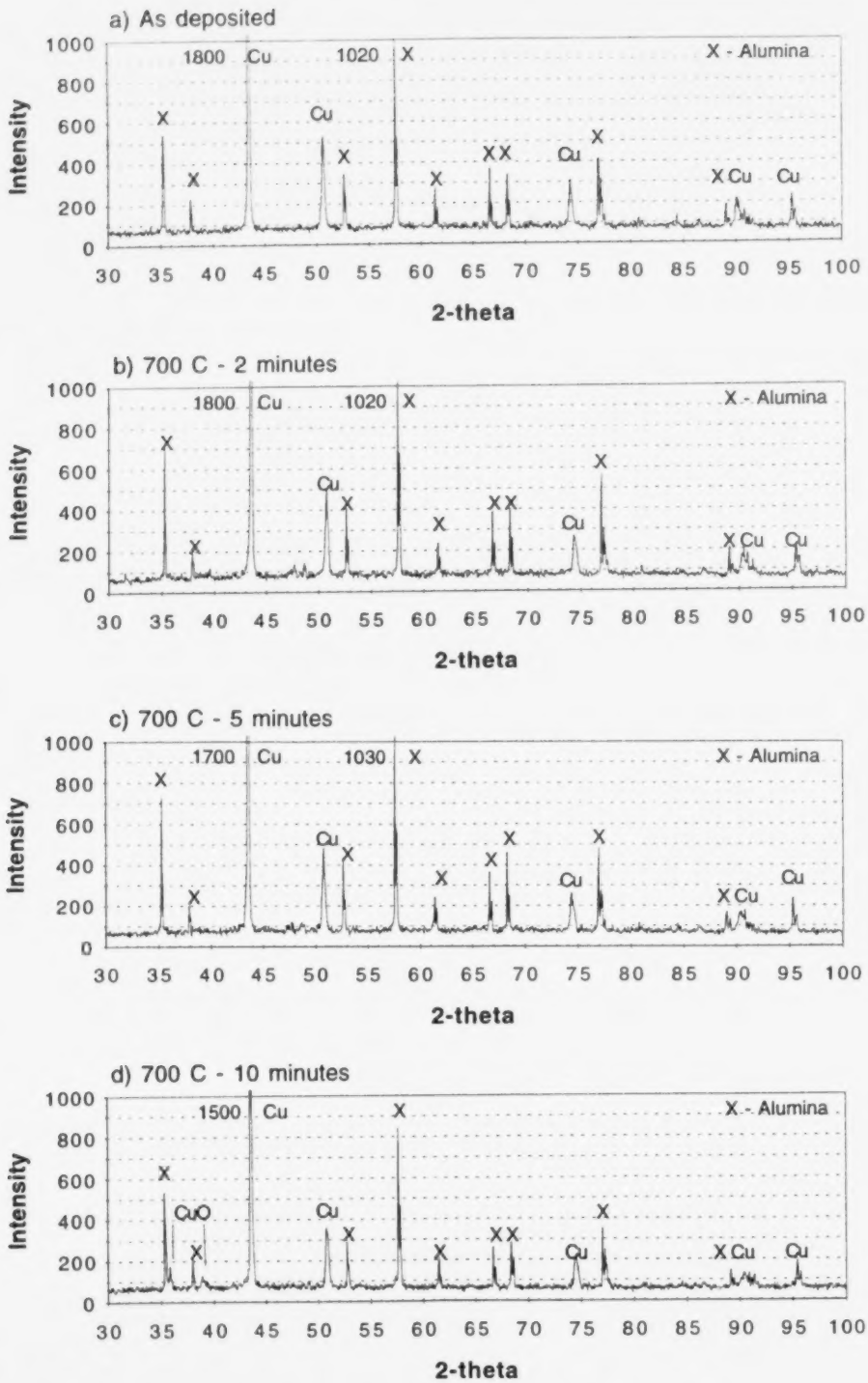

Figure 5-14: $Al_2O_3/Cu/MoSi_2$(200nm) XRD spectra for 700°C.

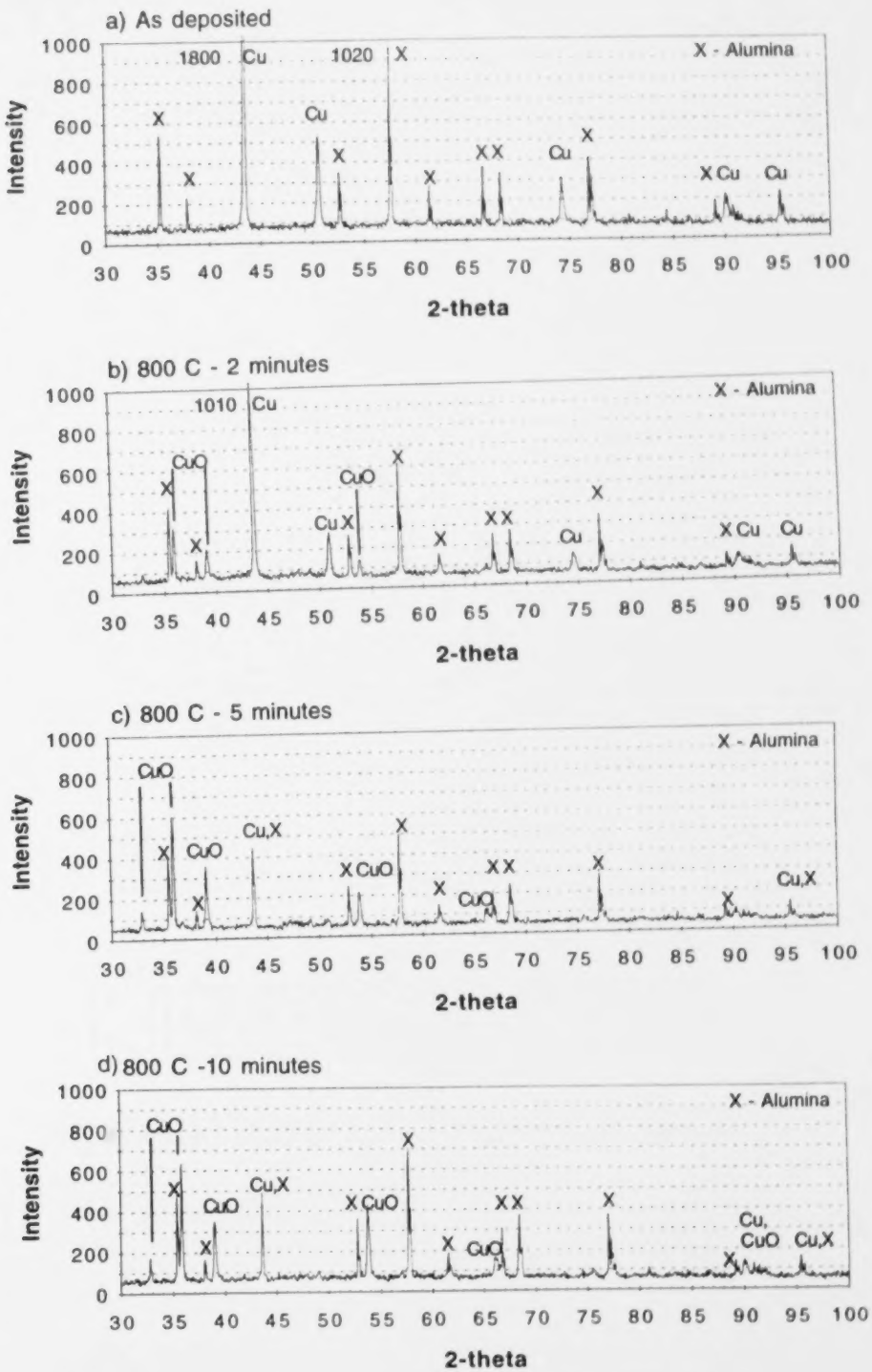

Figure 5-15: Al_2O_3/Cu/$MoSi_2$(200nm) XRD spectra for 800°C.

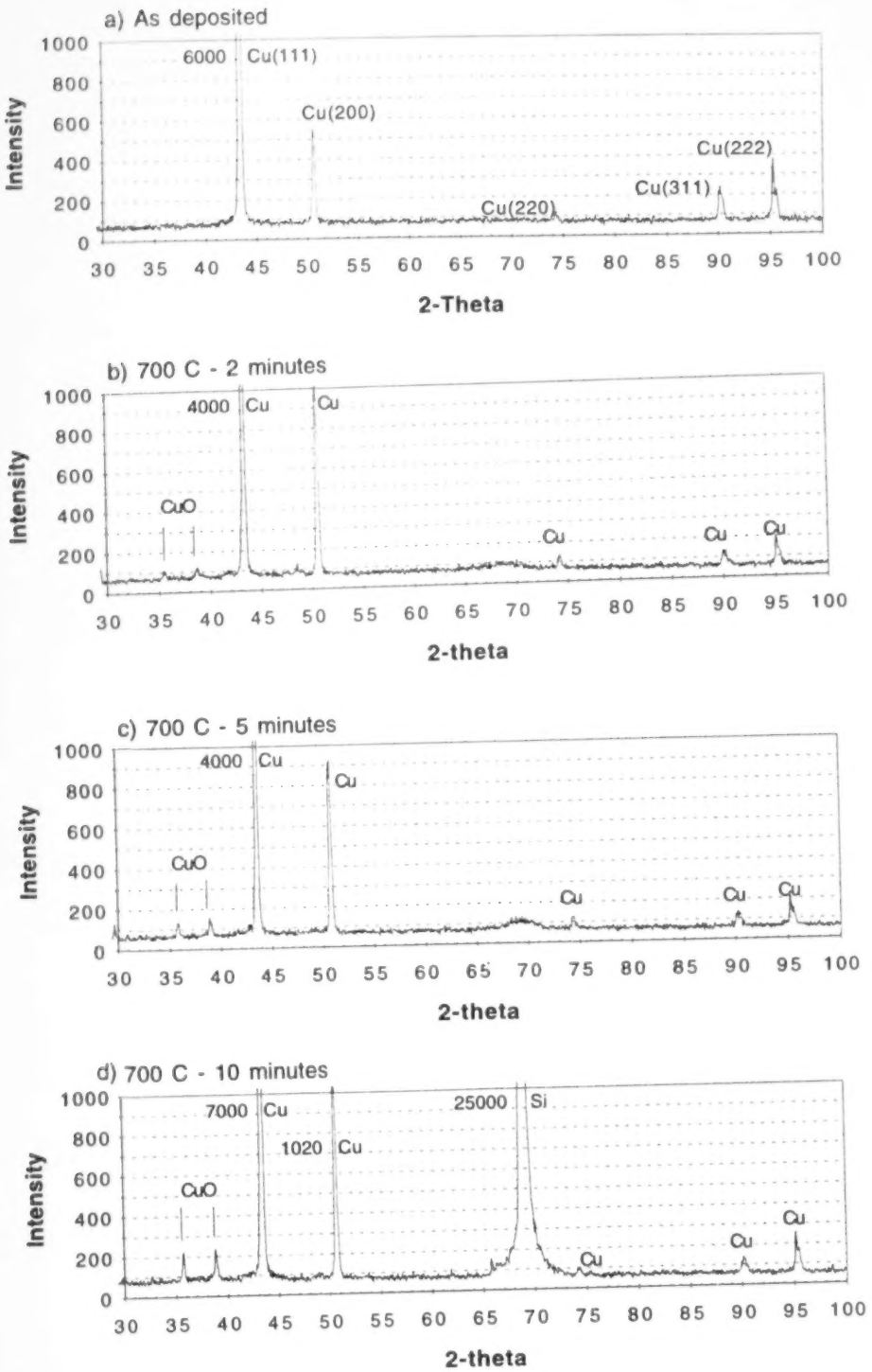

Figure 5-16: Si/Cu/$MoSi_2$(200nm) XRD spectra for 700°C.

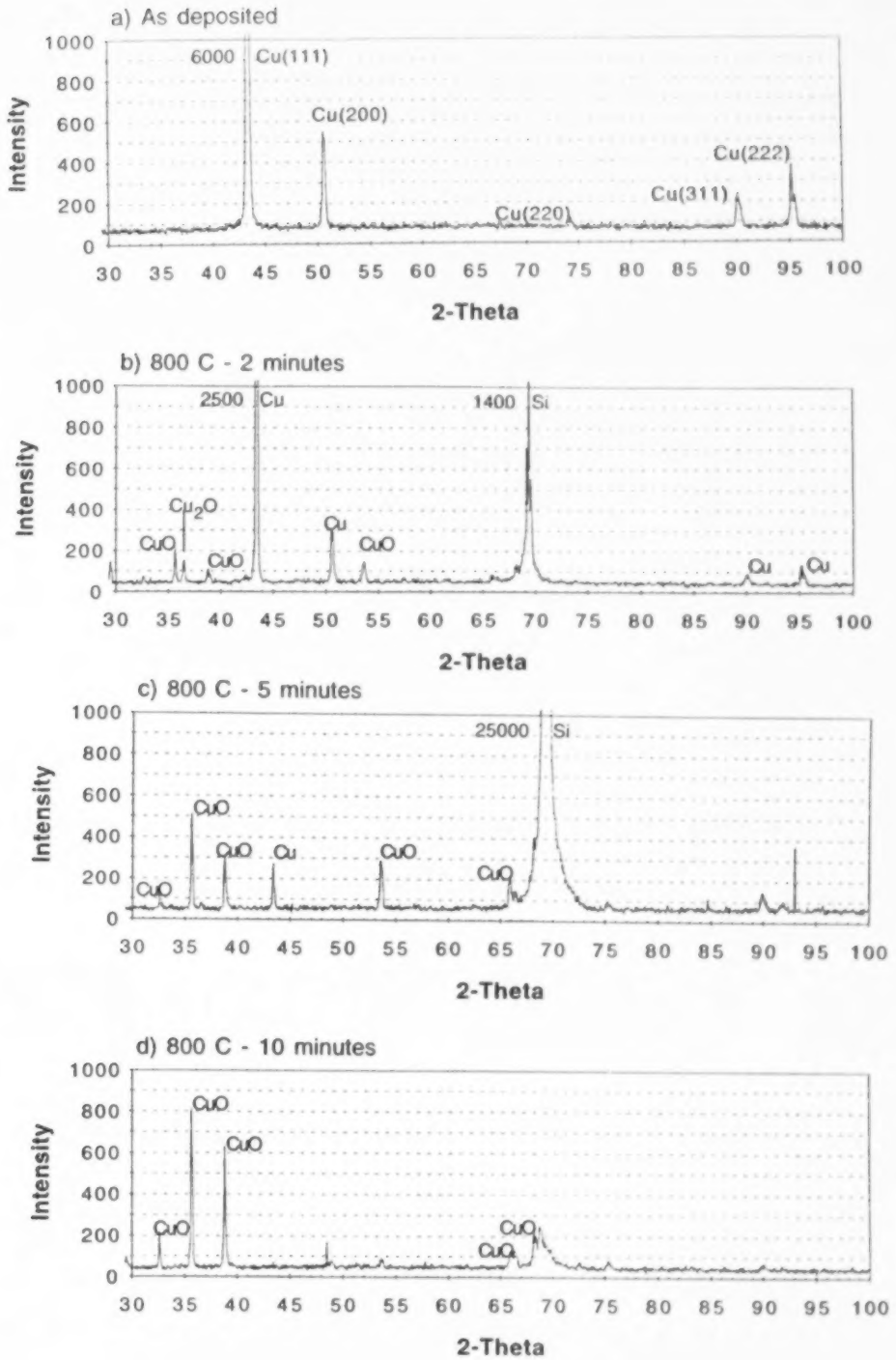

Figure 5-17: Si/Cu/$MoSi_2$(200nm) XRD spectra for 800°C.

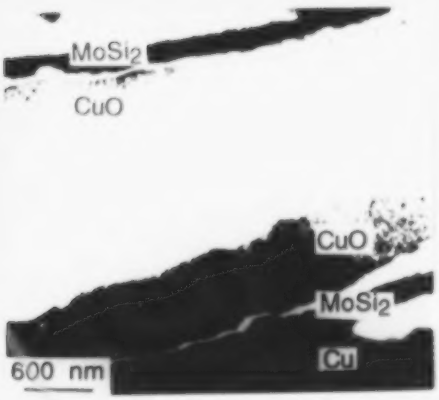

a) Bright field TEM cross section image.

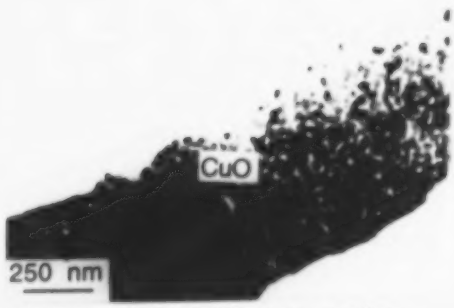

b) Bright field TEM cross section image of reduced CuO shown in a).

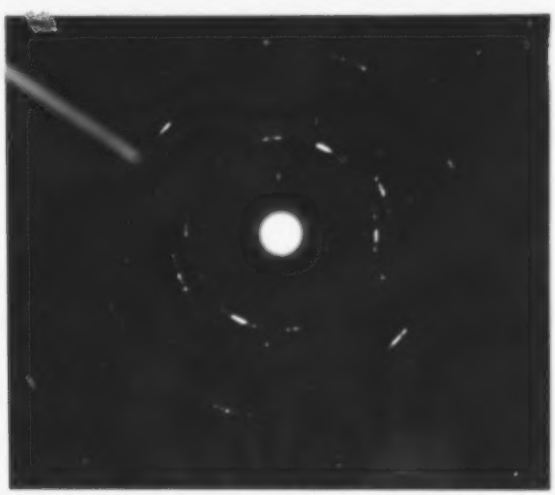

c) SAD pattern from the reduced CuO oxide layer.

Diameter (cm)	d=(2λL)/D (nm)	d-spacing Cu /hkl	d-spacing Cu_2O /hkl	d-spacing CuO hkl
2.44	0.244-weak	- -	0.246 / 111	0.252 / -111
2.83	0.211 - 1st	0.209 / 111	0.213 / 200	0.231 / 200
3.27	0.182 - 2nd	0.181 / 200	- -	0.187 / -202
3.95	0.149-weak	- -	0.151 / 220	0.151 / -113
4.68	0.127 - 3rd	0.128 / 220	0.129 / 311	0.126 / -222
5.48	0.109 - 4th	0.109 / 311	- -	- -
7.27	0.086	0.093 /400	- -	- -
7.50	0.08	0.083 / 420	- -	- -

d) Indexing of the SAD pattern in c). The rings match copper.

Figure 5-18: Si/Cu/$MoSi_2$(200nm) sample annealed at 700°C for 10 minutes.

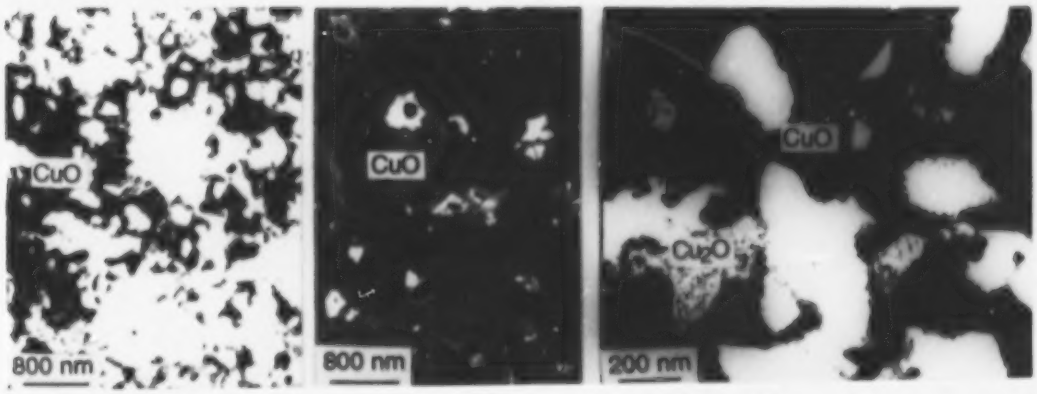

a) Bright field b) Dark field c) Bright field

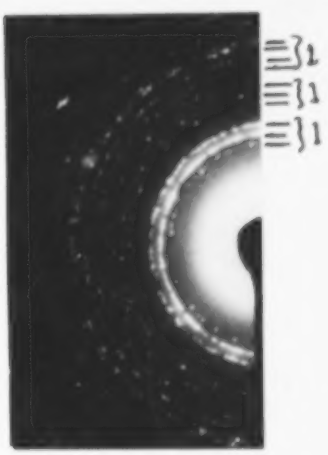

d) SAD pattern corresponding to a) and b).

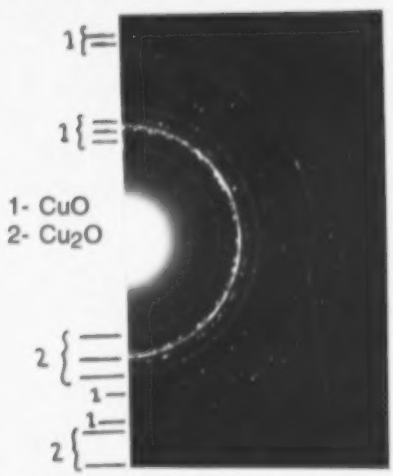

e) SAD pattern corresponding to c). CuO and Cu_2O are present.

d-spacing/Intensity (nm)	d- spacing CuO	d-spacing Cu_2O*
0.302 (4)*	- -	0.302 (9)
0.275	0.275 (8)	- -
0.253	0.252 (100)	- -
0.245 (1)*	- -	0.246 (100)
0.233	0.231 (100)	- -
0.213 (2)*	- -	0.213 (37)
0.187	0.187 (25)	- -
0.159	0.158 (12)	- -
0.151 (3)*	- -	0.151 (27)
0.143	0.142 (12)	- -
0.140	0.141 (14)	- -

f) Indexing of SAD patterns in d) and e). Asterisks indicate strong Cu_2O rings in e); all others are CuO present in both patterns.

Figure 5-19: Si/Cu/$MoSi_2$(200nm) sample annealed at 700°C for 5 minutes.

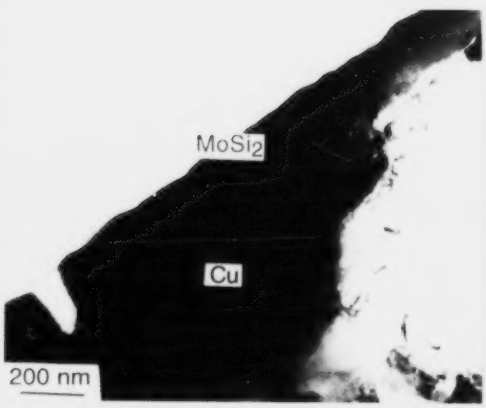

a) TEM bright field image.

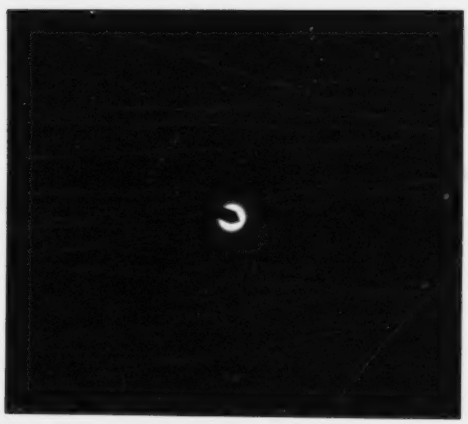

b) SAD pattern from the amorphous $MoSi_2$ layer.

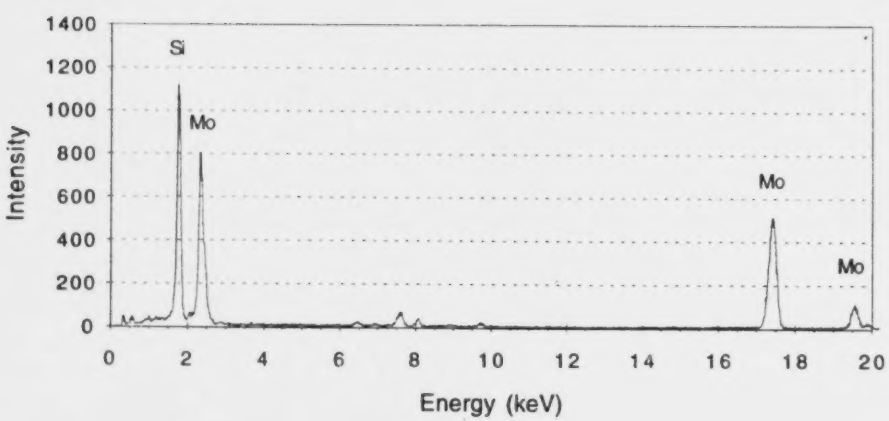

c) EDX spectrum from the amorphous $MoSi_2$ layer.

Figure 5-20: As deposited Si/Cu/$MoSi_2$(200nm) sample.

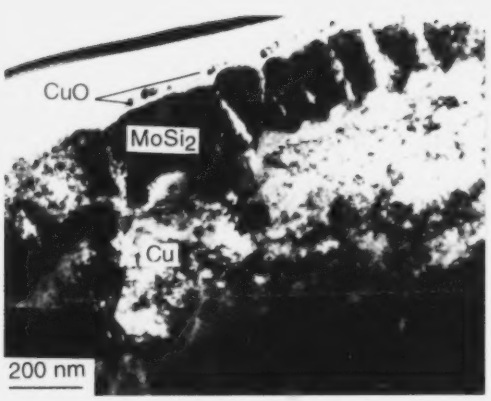

a) TEM bright field image.

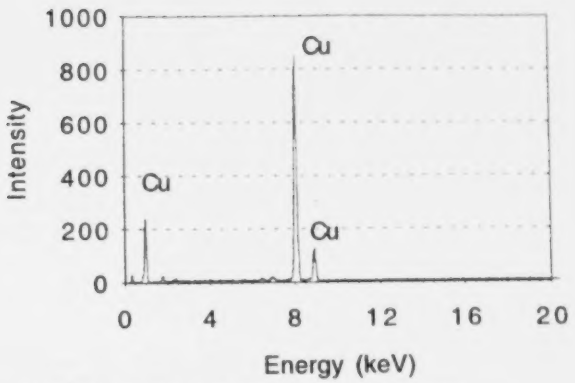

b) EDX spectrum taken from CuO layer.

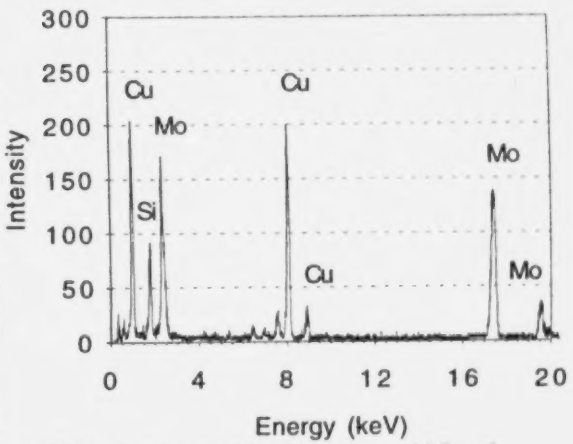

c) EDX spectrum taken from the middle of the $MoSi_2$ layer.

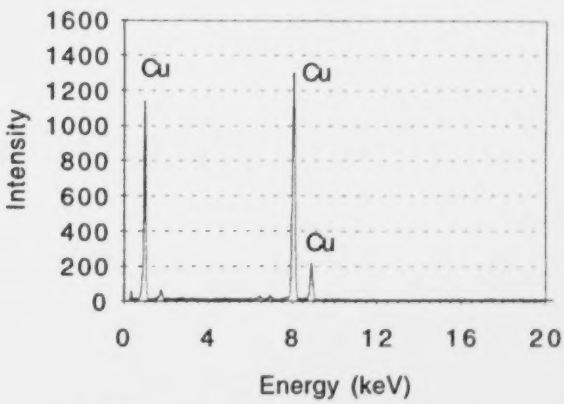

d) EDX spectrum taken from the copper layer close to the Cu/$MoSi_2$ interface.

Figure 5-21: Si/Cu/$MoSi_2$(200nm) sample annealed at 600°C for 5 minutes.

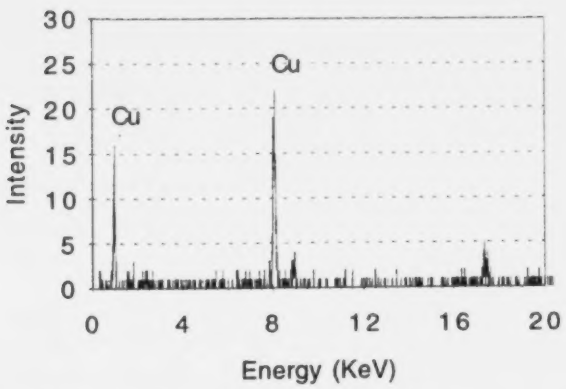

b) EDX spectrum taken from CuO layer.

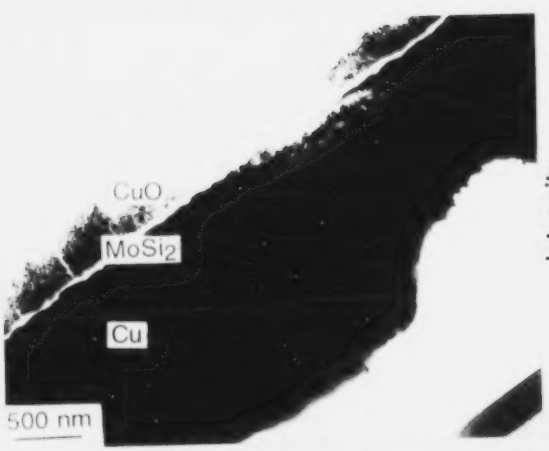

a) TEM bright field image.

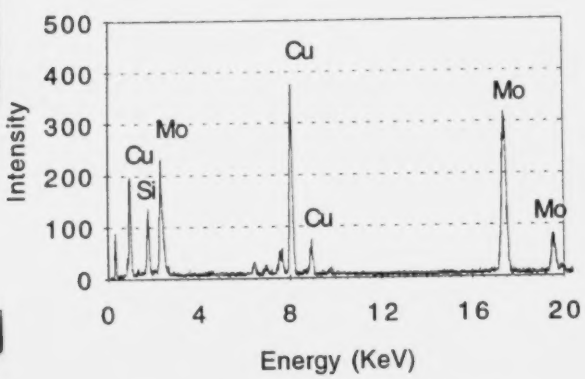

c) EDX spectrum taken from the middle of the $MoSi_2$ layer.

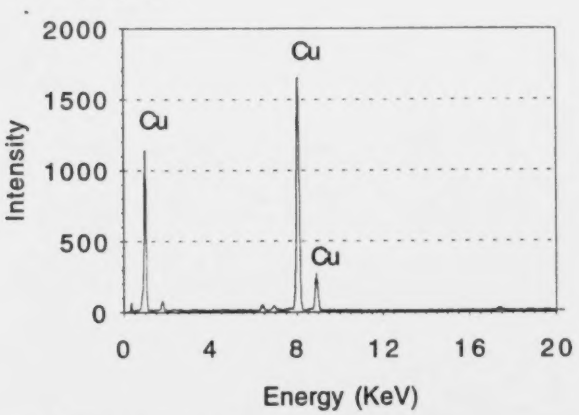

d) EDX spectrum taken from the copper layer close to the Cu/$MoSi_2$ interface.

Figure 5-22: Si/Cu/$MoSi_2$(200nm) sample annealed at 800°C for 2 minutes.

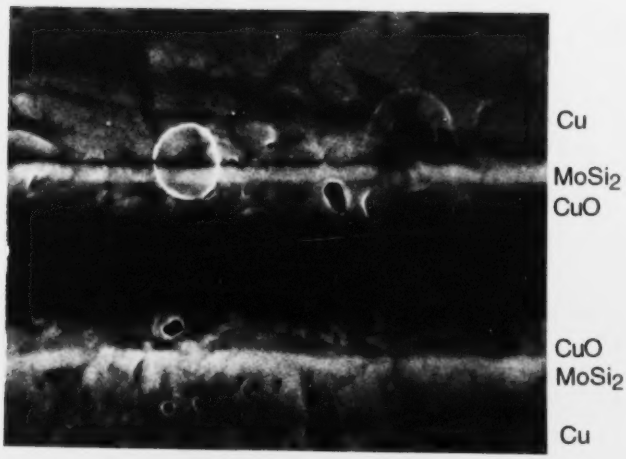

a) SEM secondary electron image.

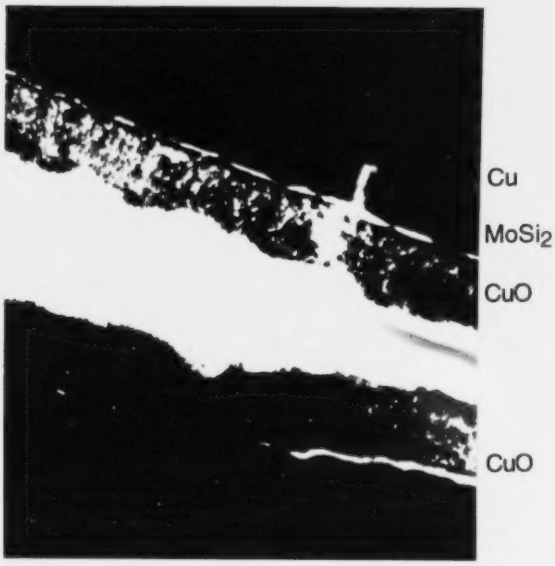

b) TEM bright field image.

Figure 5-23: A comparison of the same Si/Cu/$MoSi_2$(200nm) sample, annealed at 700°C for 10 minutes, imaged in the SEM (a) and TEM (b).

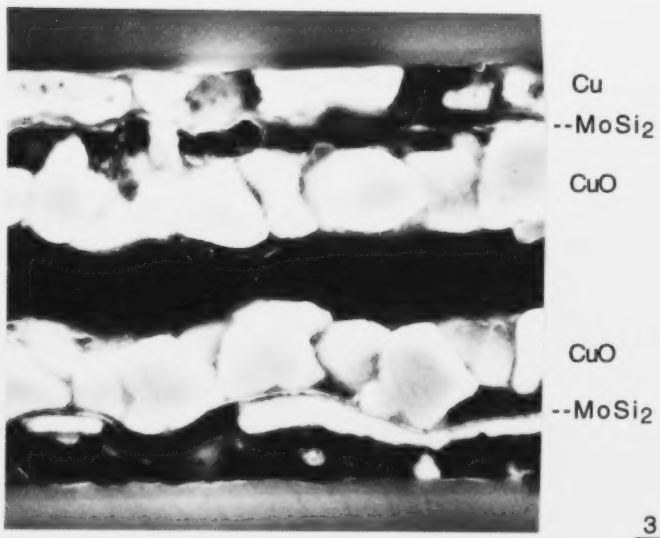

Figure 5-24: SEM secondary electron image of a Si/Cu/$MoSi_2$(200nm) sample annealed at 850°C for 5 minutes.

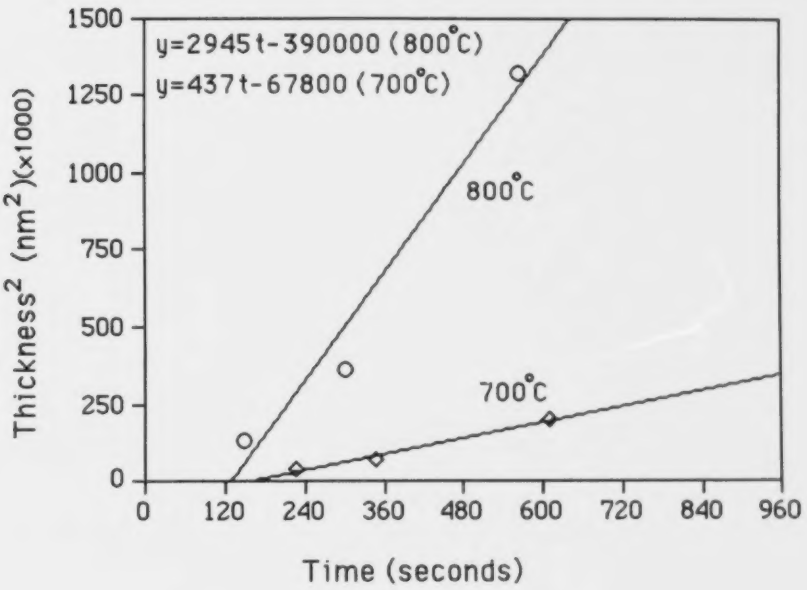

a) Plot of 800°C and 700°C kinetic data.

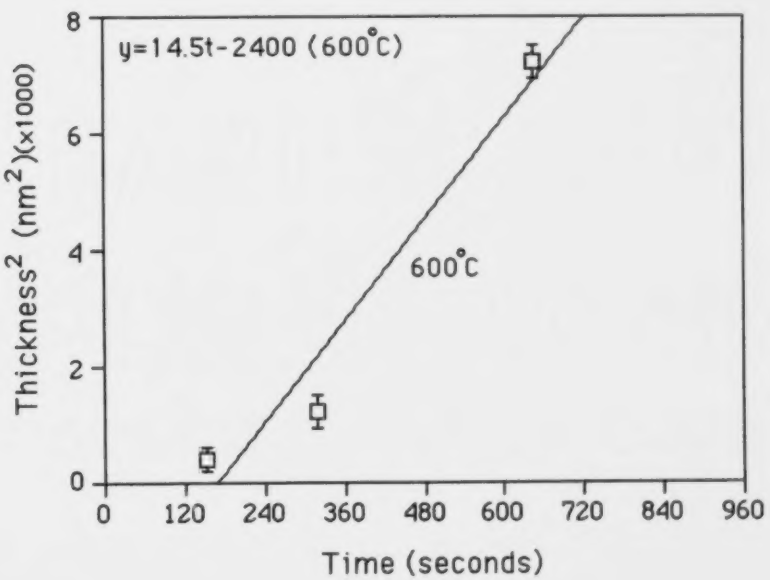

b) Plot of the 600°C kinetic data.

Figure 5-25: Kinetic plots for 600°C, 700°C, and 800°C for Si/Cu/$MoSi_2$(200nm) samples.

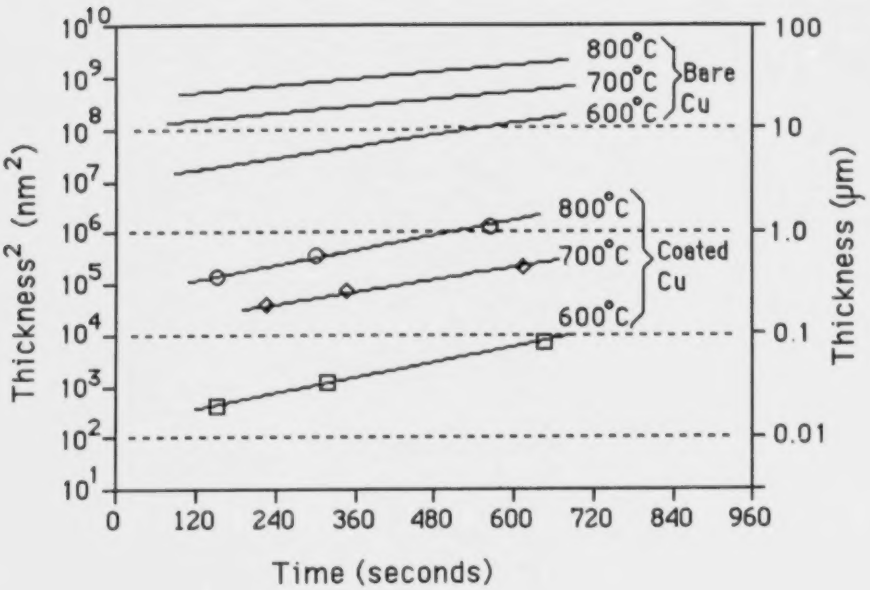

Figure 5-26: Log plot of the data from Figure 5-25.

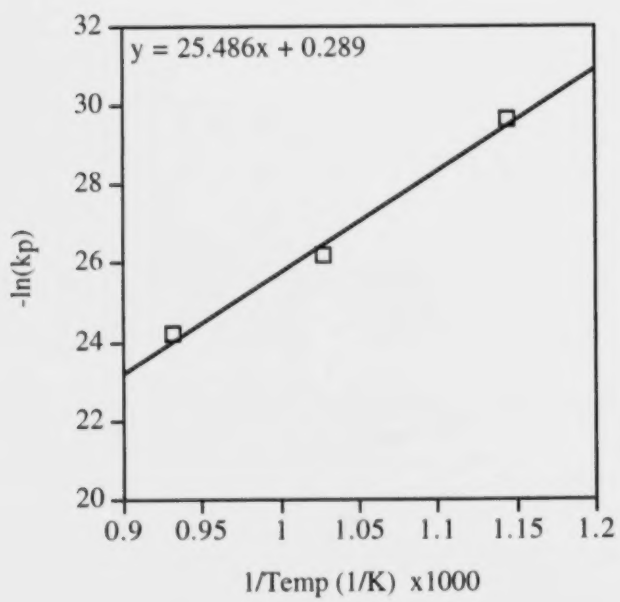

Figure 5-27: Arrhenius plot of the parabolic rate constants from Figure 5-25. The apparent activation energy is Q_{app} = 215 kJ/mol.

Table 5-2: A comparison of rate constants, apparent activation energy, oxide thickness at 15 minutes, and copper consumed at 15 minutes for bare copper and Si/Cu/$MoSi_2$(200nm).

		600°C	700°C	800°C
k_p (cm^2/s)	Cu/$MoSi_2$(200nm)	$1.45x10^{-13}$ (15800x)	$4.37x10^{-12}$ (1580x)	$2.95x10^{-11}$ (710x)
	Bare Copper	$2.30x10^{-9}$	$6.92x10^{-9}$	$2.10x10^{-8}$
Apparent Activation Energy	Cu/$MoSi_2$(200nm)	215 kJ/mol (2.6x)		
	Bare Copper	83.6 kJ/mol		
Oxide Thickness at 15 min.	Cu/$MoSi_2$(200nm)	103 nm (137x)	570 nm (46x)	1500 nm (31x)
	Bare Copper	14100 nm	26500 nm	46900 nm
Cu consumed at 15 min.	Cu/$MoSi_2$(200nm)	60 nm (143x)	330 nm (50x)	870 nm (33x)
	Bare Copper	8600 nm	16160 nm	28600 nm

*Round brackets indicate the improvement over bare copper.

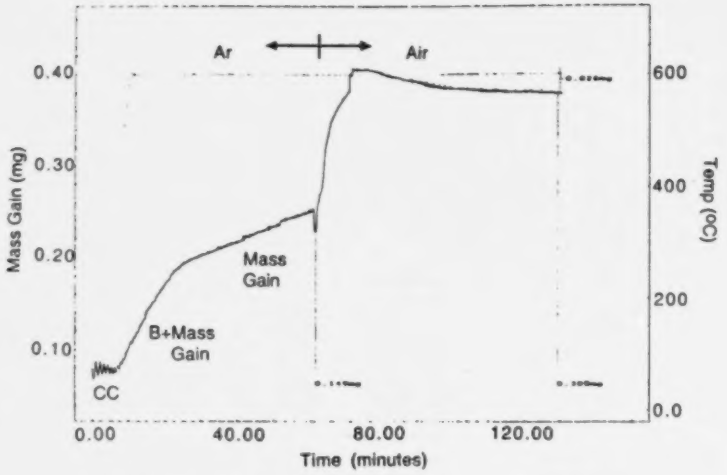

a) $Al_2O_3/Cu/MoSi_2$(200nm) sample for 600°C.

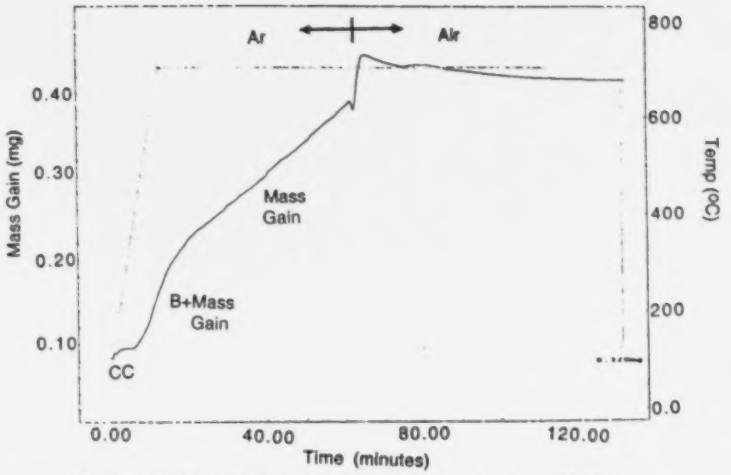

b) $Al_2O_3/Cu/MoSi_2$(200nm) sample for 700°C.

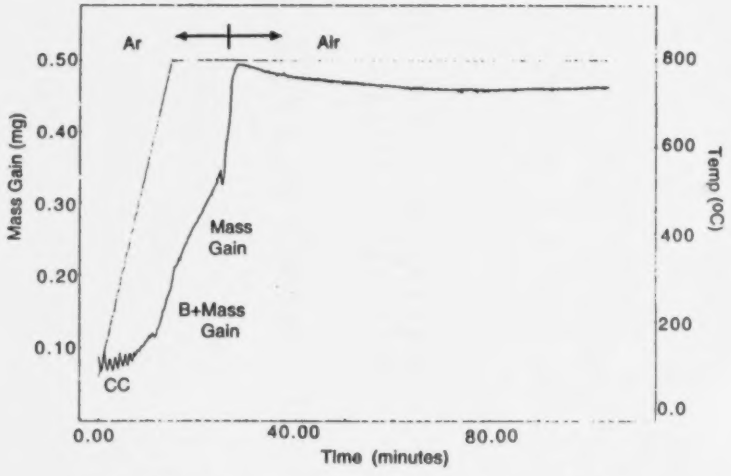

c) $Al_2O_3/Cu/MoSi_2$(200nm) sample for 800°C.

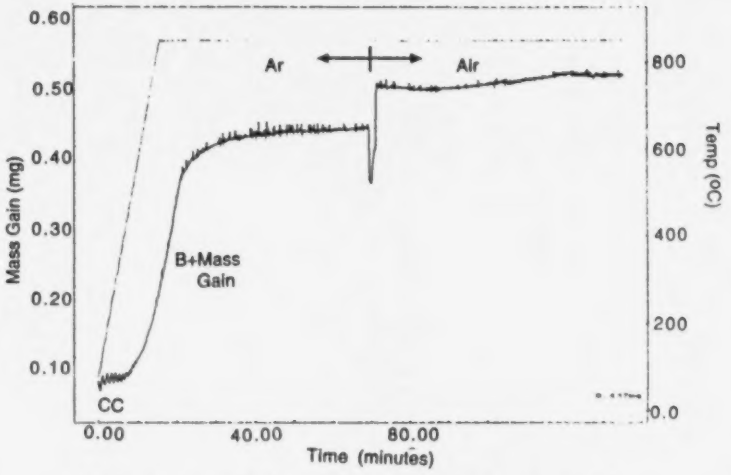

d) $Al_2O_3/Cu/MoSi_2$(200nm) sample for 850°C.

Figure 5.28: TGA plots for $Al_2O_3/Cu/MoSi_2$(200nm) samples. B - Buoyancy effects, CC - convection currents

5.4 $MoSi_2$(400nm) Barrier Layer for Copper

In this section the Si/Cu/$MoSi_2$(400nm) metallization system is analysed. Similar procedures were carried out for this system as for the $MoSi_2$(200nm) coated samples, except that only oxidized silicon substrates were used. Significantly better results were obtained for the $MoSi_2$(400nm) coating at the higher temperatures. This may be due to a different diffusion mechanism of copper through the $MoSi_2$ barrier, resulting from phase transformations and grain growth.

5.4.1 Film Integrity for the $MoSi_2$ (400nm) Coating

Peak to peak roughness values between Cu/$MoSi_2$(200nm) coatings on oxidized silicon vs. alumina showed a 4 to 6 times difference. This was due to the surface roughness of the substrate material, which was about an order of magnitude difference between silicon and the thin film grade alumina used. Therefore, all the Cu/$MoSi_2$(400nm) films were deposited on oxidized silicon to minimize the roughness effect (discussed below). Figure 5-29a shows an AFM 14μm scan of a Si/Cu/$MoSi_2$(400nm), as deposited sample with artificial shading from the right side. Shadowing effects bring out the hillock features. Figure 5-29b shows an AFM 14μm scan of the same sample from (a) in 3 dimensions. The z dimension is exaggerated and is not to scale with the x and y axes. AFM roughness values (R_a) for these films were <30nm with peak to peak variations of <100nm, which is similar to the $MoSi_2$(200nm) coatings. These values are in part due to agglomeration of the $MoSi_2$ on the surface. The dimensions of the larger hillocks, as measured by the AFM, are 0.4μm in diameter, slightly larger in size than the $MoSi_2$(200nm) coatings.

An SEM secondary electron plan view shown in Figure 5-30 is also of an as deposited Si/Cu/$MoSi_2$(400nm) sample. The morphology of this figure matches very well with the as deposited AFM scans. The largest hillocks also measure 0.4μm in diameter. Figures 5-29 and 5-30 are representative of the overall as deposited surfaces. The surface roughness may play a role in the effectiveness of the diffusion barrier. The same roughness will have less of an effect on thicker barriers (Figure 5-31). The minimal thickness of a 200nm thick barrier layer is only 150nm, with a peak to peak roughness of 100nm. If the nominal thickness is doubled to 400nm, the minimal thickness is 2.3 times thicker. Since diffusion through the layer is governed

by the parabolic rate law, increasing the minimal thickness by the fraction x will give an improvement of x^2, or $2.3^2 = 5.3$ times.

Figures 5-32a to d are SEM secondary electron images comparing $MoSi_2$(200nm) and $MoSi_2$(400nm) coated samples, at 600°C for 10 minutes and 850°C for 10 minutes. For the samples annealed at 600°C for 10 minutes there is not much difference in surface morphology between the two because the oxide thickness is very thin in both cases, (80nm for the $MoSi_2$(200nm) coating and <10nm for the $MoSi_2$(400nm) coating). The underlying coating is visible for both samples. However, there is a significant difference for the samples annealed at 850°C. The oxide on the $MoSi_2$(200nm) coating measures ~3.7μm thick with a grain size that varies from ~3μm to ~4μm, whereas for the $MoSi_2$(400nm) coating the oxide measures only ~230nm thick with similar grainsize.

5.4.2 X-ray Diffraction Analysis

X-ray diffraction was completed for Si/Cu/$MoSi_2$(400nm) samples annealed at 700°C and 800°C, which are shown in Figures 5-33 and 5-34 respectively. The copper and $MoSi_2$ show similar trends for the $MoSi_2$(400nm) as they did for the $MoSi_2$(200nm) spectra. No $MoSi_2$ peaks are present in the as deposited spectrum (Figure 5-33a) and copper shows a <111> preferred orientation in the direction perpendicular to the substrate. In Figure 5-33 (700°C) there is a slight variation in the intensities of the two strongest copper peaks at 43.8° and 50.4°, but there is no trend as the annealing time increases. A very small CuO peak is present at 5 minutes. Other peaks (spikes) at 61.6°, 66°, and 66.5° can be attributed to the silicon substrate. Also, the other small peaks match with the hexagonal $MoSi_2$ and the lower molybdenum silicide phase, Mo_5Si_3. Figure 5-35 shows the spectra for 800°C. Again, there is little change in the intensities of the two strongest copper peaks as the annealing time increases from 5 minutes to 15 minutes. This is in contrast with Figure 5-17, the $MoSi_2$(200nm) coating, where at 5 minutes copper peaks were very weak and at 10 minutes completely gone. At 800°C for 15 minutes the CuO peaks correspond to a thickness of ~260 nm. Also weak peaks for $MoSi_2$(hex) and Mo_5Si_3 phases are present.

5.4.3 $MoSi_2$ Phase Transformation and Grain Growth

An analysis of the $MoSi_2$ layer was necessary to better understand the kinetics of oxidation. Figure 5-35 shows TEM-EDX spectra from a Si/Cu/$MoSi_2$(400nm) sample annealed at 800°C for 2 minutes. The EDX spectrum in Figure 5-35b taken from the CuO layer shows copper peaks and a weak oxygen peak. If the oxide was reduced, it was not reduced completely. This is also indicated by the porosity of the oxide in Figure 5-35a. Comparing Figures 5-35a with 5-22a (Si/Cu/$MoSi_2$(200nm)), there is a noticeable difference in the porosity of the oxide layer and in the average thickness. This may be a result of room temperature ion milling for the $MoSi_2$(400nm) sample as opposed to cold stage ion milling for $MoSi_2$(200nm) samples. In Figure 5-35b, molybdenum and silicon peaks are present as well as copper. A semiquantitative analysis on the silicon-molybdenum ratios for $MoSi_2$(400nm) and $MoSi_2$(200nm) coatings was completed. The $MoSi_2$(400nm) coating contained ~45 at% silicon (due to loss of silicon to the underlying copper), which indicates the presence of both Mo_5Si_3 and $MoSi_2$. A rough calculation, using a standardless approach, indicates about ~80% Mo_5Si_3 and ~20% $MoSi_2$. The $MoSi_2$(200nm) coating contained ~30 at% silicon, which from the phase diagram corresponds to the two phase region between Mo_3Si and Mo_5Si_3. The above calculations are only approximate since standards were not used and values may vary by ±10%. The amount of silicon dissolved in the copper is significant, causing the silicide to transform to the lower phases, but as the $MoSi_2$ layer becomes thicker the effect is lessened. This is confirmed by comparing the amount of silicon in the copper layer from Figure 5-35d ($MoSi_2$(400nm) coating) with Figure 5-22d ($MoSi_2$(200nm) coating). A semiquantitative analysis gives the silicon content for the two samples to be very close. Since there is more silicon in the $MoSi_2$(400nm) coating, losing the same amount silicon has less of a diluting effect. From EDX analysis, the amount of silicon from the $MoSi_2$ layer that is lost to the copper layer is significant and will have to be addressed if $MoSi_2$ is to be a useful diffusion barrier for copper.

A number of diffusion barriers are already being used between copper and silicon for annealing in a vacuum. A 20nm Ta barrier, between copper and silicon, has good diffusion barrier properties from 320°C to 630°C, depending on processing conditions and oxygen contamination at the Ta/Cu interface [126]. Ta_2N layers were also found to have similar properties as Ta [127]. Other barriers such as Ni, Cr, Ti, W, and C layers are reliable from 350°C to 450°C. A TiB_2 alloy barrier made by LPCVD is stable in the Cu/TiB_2/Si system up to 750°C [128]. Amorphous layers without grain boundaries

demonstrate good barrier properties. Sputtered amorphous Ta-Si-N diffusion barriers reported by Kolawa et al. [129] maintain their integrity up to 900°C for 30 minutes in vacuum for the Cu/Ta-Si-N/$TiSi_2$/Si system.

Further analysis on the phase transformations of the $MoSi_2$ was completed using selected area diffraction patterns from plan view samples. $MoSi_2$ is amorphous when deposited. From literature data [71], the thin film phase transformations of $MoSi_2$ were characterized for the temperature range between 300°C to 900°C. The $MoSi_2$ metastable hexagonal phase was formed at 300°C and the transformation to the stable $MoSi_2$ tetragonal phase occurred at ~800°C. At 900°C only the tetragonal phase was present. Therefore, from the literature data and the above EDX analysis of the loss of silicon from the $MoSi_2$ layer, it is expected that the hexagonal $MoSi_2$ and the Mo_5Si_3 phases are present in the Si/Cu/$MoSi_2$(400nm) samples. This would also confirm the weak peaks from the XRD analysis. Figure 5-36 shows a comparison between $MoSi_2$(400nm) coated samples annealed at 600°C for 2 minutes and 850°C for 10 minutes. Dark field images and their corresponding SAD patterns are shown for the respective samples. The SAD patterns are indexed in Figure 5-36e. For the shortest annealing time and temperature (600°C for 2 minutes) the SAD pattern has a broad band indicating the $MoSi_2$ layer is still partly amorphous. The strong rings correspond to hexagonal $MoSi_2$ and a few of the weaker rings correspond to Mo_5Si_3. For the longest annealing time and temperature (850°C for 10 minutes) the diffuse ring is gone and the rings for hexagonal $MoSi_2$ are not as continuous. This loss in ring continuity is due to the grain growth that has occurred. There is additional indication for the presence of Mo_5Si_3 from extra rings not present in the 600°C - 2 minute pattern. Phase transformations are noted because they can have an effect on the mechanism of diffusion and ultimately the how well the barrier works.

The other point to note from the dark field images is the change in grain size. Grain growth of the molybdenum silicide layer will affect the diffusion rate for copper since defect diffusion is dominant at the temperatures being studied. Grain size measurements from the samples were 20nm±10nm for the 600°C - 2 minute sample and 60nm±35nm for the 850°C - 10 minute sample. A rough calculation assuming square grains and grain boundaries of 0.5nm shows the relative amount of grain boundary area decreases by the same amount the grain size increases, i.e., for a three fold increase in grain size the relative grain boundary area is reduced by 3 times, (for 60nm grains the relative grain boundary percentage is 2.45% of the total area). It is

expected that an increase in grain size will be beneficial to the diffusion barrier properties since there are fewer defect paths for copper to diffuse through. It is noted that the grain size measurements for the $MoSi_2$(200nm) coatings were <10nm for samples annealed at 600°C for 2 minutes and ranged from 10nm to 40nm at 850°C for 10 minutes. Grain sizes for the 200nm $MoSi_2$ coatings were smaller than for 400nm $MoSi_2$ coatings.

5.4.4 Kinetics of Oxidation

Oxidation kinetics were quantified by taking thickness measurements. Cross sections of all Si/Cu/$MoSi_2$(400nm) samples were made and imaged in either the SEM or the TEM, depending on the thickness of the oxide layer. Kinetic data was calculated for 600°C, 700°C, 800°C, and 850°C. Parabolic rate constants (k_p) were obtained by plotting the thickness squared vs. time in Figure 5-37. The raw data is given in Appendix D. Error bars for each point are indicated; otherwise they are contained within the size of the data marker. Coefficients of determination (r^2) are 0.904 for 850°C, 0.996 for 800°C, and 0.971 for 700°C. At 600°C only 15 minute and 10 minute data points were taken; there was no surface oxide below 10 minutes. Incubation times increased as the temperature decreased; they ranged from 109 seconds for 850°C to 578 seconds for 600°C. Figure 5-38 shows the thickness data plotted on a log scale along with the data for bare copper. There is a significant improvement for the $MoSi_2$(400nm) coated samples, even at 850°C. The data for the rate constants, oxide thickness at 15 minutes, and copper consumed at 15 minutes for bare copper and Si/Cu/$MoSi_2$(400nm) samples are tabulated in Table 5-3. The values in brackets indicate the improvement over bare copper. At 850°C there is a 200 times improvement over the amount of copper consumed compared to bare copper. This corresponds to a CuO layer ~300nm thick at 15 minutes. The improvement trend for the $MoSi_2$(400nm) coated samples increases as the temperature increases. This trend is opposite for the $MoSi_2$(200nm) coated samples. This is discussed further below.

Figure 5-39 shows Arrhenius plots of the kinetic data from Figure 5-37 ($MoSi_2$(400nm) coating) and Figure 5-25 ($MoSi_2$(200nm) coating). There are two ways to interpret the plot at present. Two curves ('a' and 'b') could be drawn, suggesting a change in the diffusion mechanism of copper through the barrier layer at about 700°C. If the two points for 600°C and 700°C (curve 'a') are joined to form a

straight line then the apparent activation energy is 220 kJ/mol, which is close to the 215 kJ/mol for the $MoSi_2$(200nm) coated samples. This result is not surprising since a thicker $MoSi_2$ diffusion barrier should shift the previous plot for 200nm $MoSi_2$ coating upwards, without a change in slope (providing the oxidation process is the same for both). Joining the other three data points (curve 'b') gives an apparent activation of 22 kJ/mol. The parabolic rate constants above 700°C are within an order of magnitude of each other, resulting in the shallow slope given by curve 'b'. Another way to interpret the data is through curve 'c', where all the data points are fitted to a single curve. The apparent activation energy in this case is 110 kJ/mol. The coefficient of determination is not particularly good (r^2= 0.860). A single line through the data points suggests the same oxidation mechanism for copper for all the temperatures of interest. To confidently determine if there is a change in the diffusion mechanism, more data points are needed. At least 3 additional temperatures, with 4 annealing times at each temperature, would be needed to further clarify the kinetics. Without the additional experimental data, it is difficult to interpret the current result.

A comparison between the $MoSi_2$(400nm) coating and the $MoSi_2$(200nm) coating, on the points of silicon loss, phase transformation, and grain growth, and their effects on the diffusion rates is necessary. From this study (though not comprehensive) of the $MoSi_2$ layer it was found that the $MoSi_2$ diffusion barrier sputter deposited onto the copper was amorphous. Upon annealing it had become partly crystalline at 600°C. This agrees with the literature, where $MoSi_2$ has been shown to crystallize as early as 300°C. From SAD patterns of $MoSi_2$(400nm) coatings the metastable, hexagonal form of $MoSi_2$ was shown to be present at 600°C. From the TEM analysis it was found that the loss of silicon, from the $MoSi_2$ layer into the copper, caused the $MoSi_2$ to transform to the lower silicides. The final composition of the barrier layer depends on the amount of silicon lost. From SAD patterns taken from the $MoSi_2$(400nm) coatings at 600°C, Mo_5Si_3 was also shown to be present. EDX analysis was in agreement with this result for the $MoSi_2$(400nm) coatings. EDX semiquantitative analysis also showed that the silicon lost from the $MoSi_2$(200nm) coatings was enough for the barrier layer to transform to Mo_3Si and Mo_5Si_3. Therefore, different phases are present for the two different $MoSi_2$ barrier thicknesses. The grain size for both thicknesses of coatings was <20nm for the shortest and lowest temperature anneal. However, the grain size grew to ~60nm ± 35nm for the highest temperature anneals for the 400nm coating, while the 200nm coating remained between 10 nm and 40 nm. This may partly explain the significant improvement of the 400nm $MoSi_2$ coating over the 200nm $MoSi_2$ coating at

high temperatures. A larger grain size corresponds to fewer grain boundaries or fewer short circuit paths for copper diffusion.

The phase transformations and the grain growth may explain the differences in trends for the two different $MoSi_2$ barrier layers. One interpretation of the apparent activation energy plot suggests a change in the diffusion mechanism for the $MoSi_2$(400nm) barrier. Also grain growth at higher temperatures reduces the number of defect paths for the copper to travel through, again slowing the diffusion rate. The excessive loss of silicon in the $MoSi_2$(200nm) coating may reduce the thinner barrier's effectiveness as the temperature increases. The grain size of the 200nm $MoSi_2$ did not increase as much as the 400nm coating which also accounts for its poorer performance at high temperatures. Significant amounts of copper are present in the $MoSi_2$ layer (for both coating thicknesses). To account for all the copper, a number of possibilities exist. Little is known about any ternary phases between copper, molybdenum, and silicon or the solubility of copper in molybdenum silicide. Copper is likely present in the grain boundaries of the $MoSi_2$ layer, as it diffuses to the surface to form copper oxide. There may also be dissolved copper in the lattice. Whatever the case, the presence of copper may be affecting the temperatures at which phase transformations occur in the $MoSi_2$. Further analysis of the presence of copper in $MoSi_2$ would be needed to make any confident conclusions.

Although the mechanism for the diffusion of copper through $MoSi_2$ is far from understood, the results are favourable. At 600°C for 15 minutes, for a 200nm $MoSi_2$ layer sputter deposited onto copper, ~100nm of CuO forms on the surface; and <35nm of oxide forms on a 400nm $MoSi_2$ layer. At 850°C, for a 400nm $MoSi_2$ layer sputter deposited onto copper, only ~300nm of CuO forms on the surface.

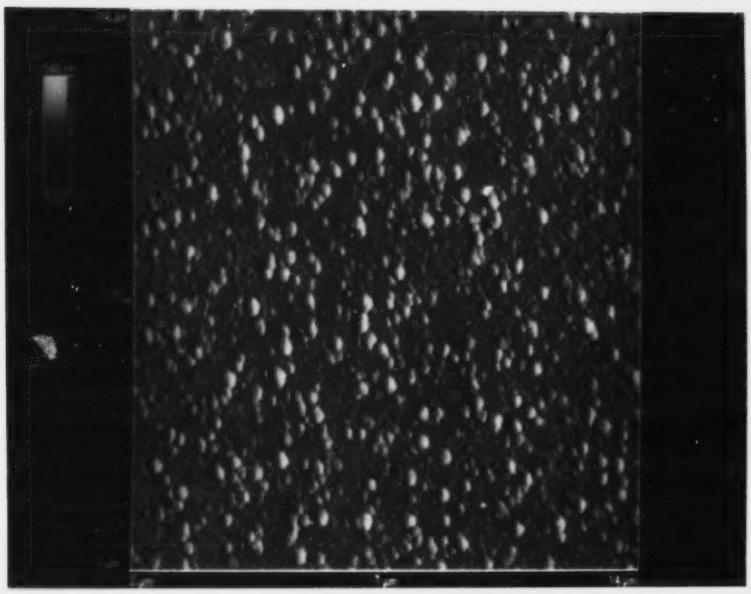

Figure 5-29a: AFM 14 μm scan of Si/Cu/$MoSi_2$(400nm) as deposited sample.

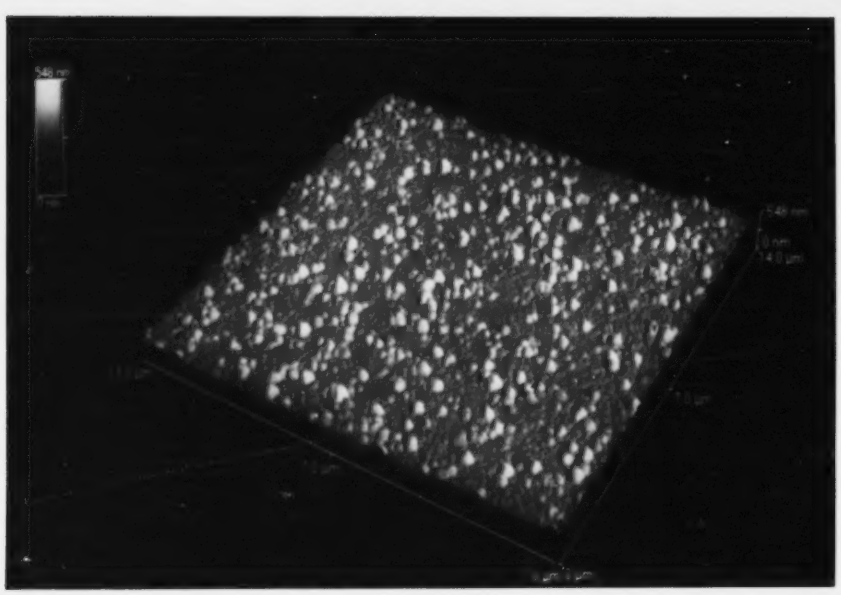

Figure 5-29b: AFM 14 μm scan (3-dimensional view) of Si/Cu/$MoSi_2$(400nm) as deposited sample.

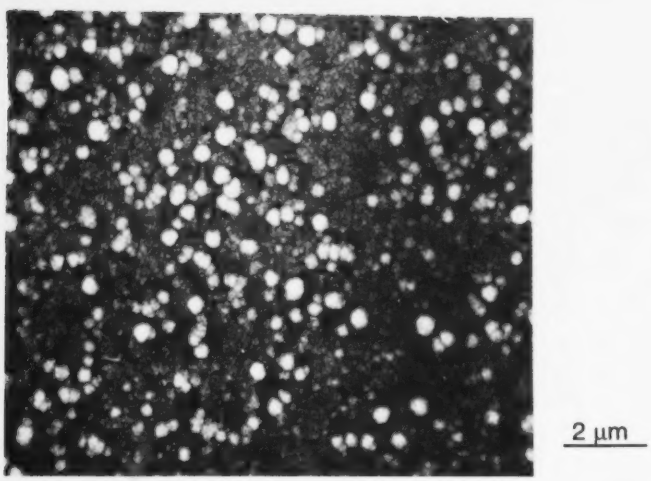

Figure 5-30: SEM secondary electron image plan view of Si/Cu/$MoSi_2$(400nm) as deposited sample.

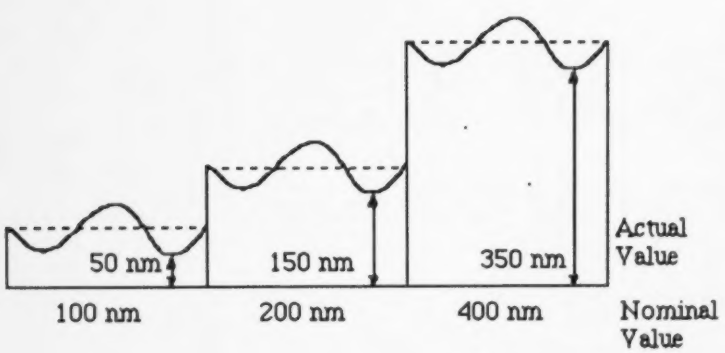

Figure 5-31: Effect of surface roughness on the usefulness of the diffusion barrier.

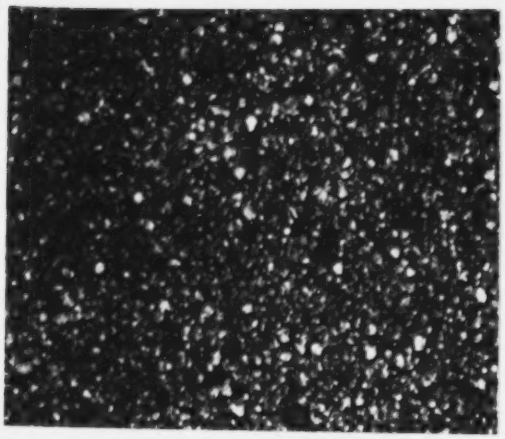

3 μm

a) Si/Cu/$MoSi_2$(200nm) sample annealed at 600°C for 10 minutes.

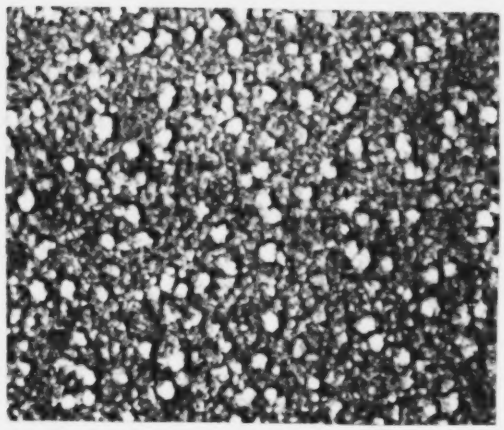

3 μm

b) Si/Cu/$MoSi_2$(400nm) sample annealed at 600°C for 10 minutes.

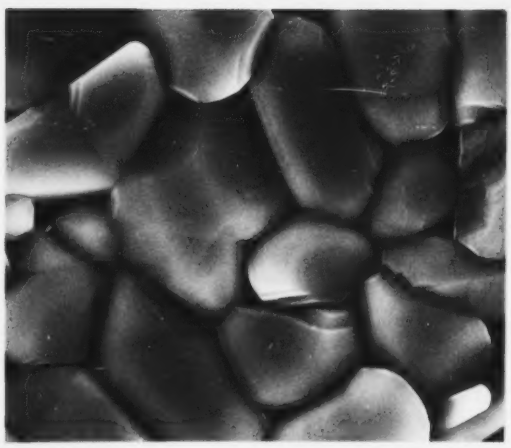

3 μm

c) Si/Cu/$MoSi_2$(200nm) sample annealed at 850°C for 10 minutes.

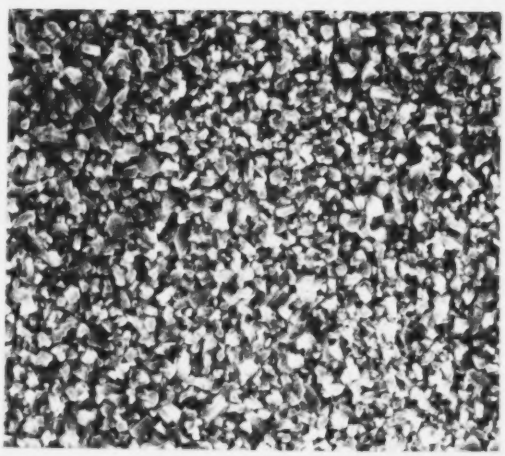

3 μm

b) Si/Cu/$MoSi_2$(400nm) sample annealed at 850°C for 10 minutes.

Figure 5-32: SEM secondary electron images comparing $MoSi_2$(200nm) and $MoSi_2$(400nm) coatings.

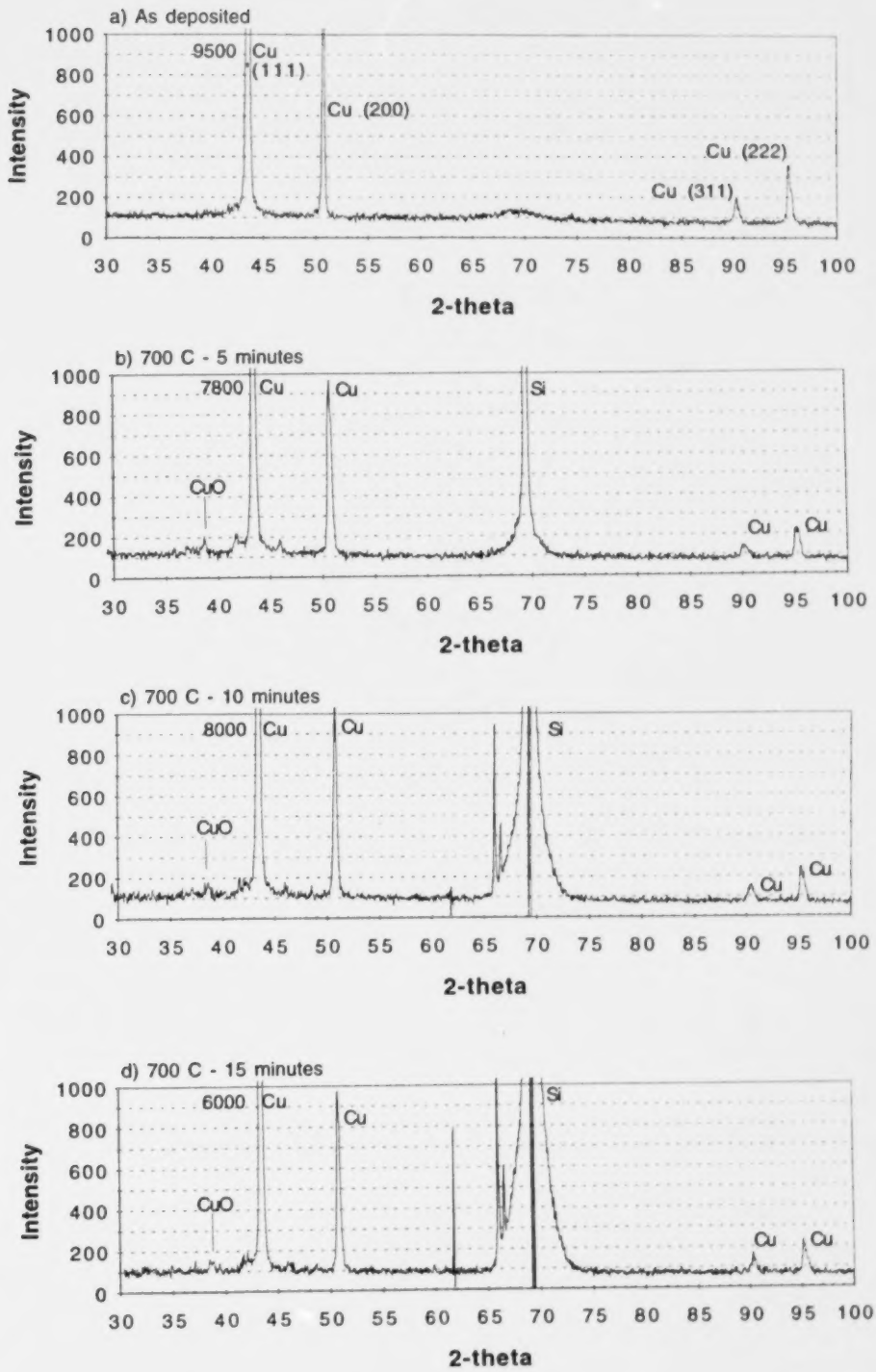

Figure 5-33: Si/Cu/$MoSi_2$(400nm) XRD spectra for 700°C.

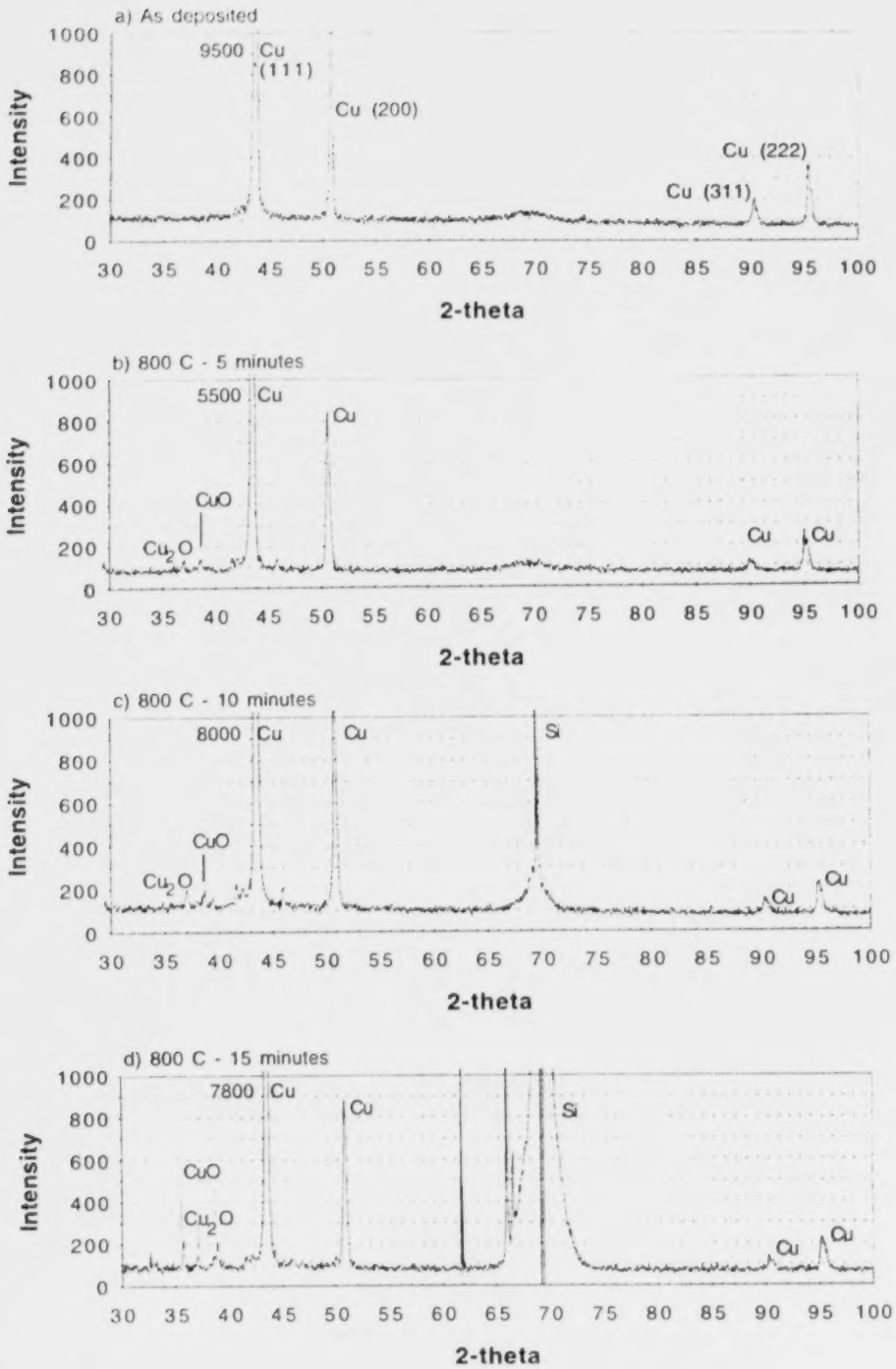

Figure 5-34: Si/Cu/$MoSi_2$(400nm) XRD spectra for 800°C.

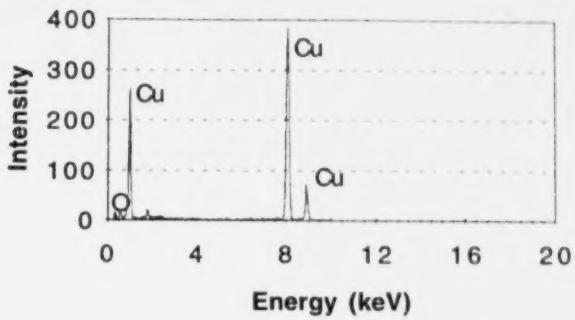

b) EDX spectrum taken from CuO layer.

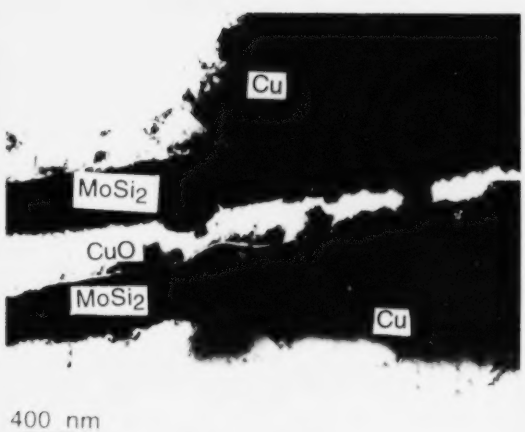

a) TEM bright field image.

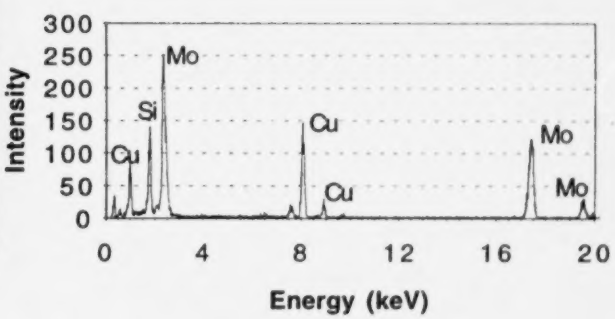

c) EDX spectrum taken from the middle of the $MoSi_2$ layer.

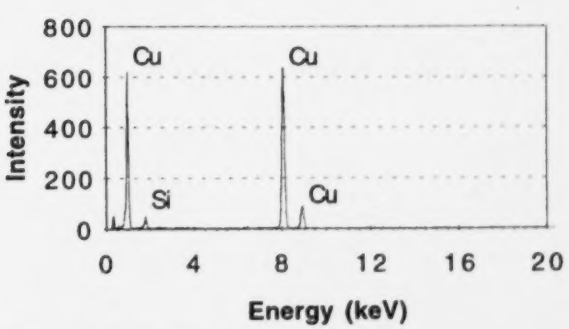

d) EDX spectrum taken from the copper layer close to the Cu/$MoSi_2$ interface.

Figure 5-35: Si/Cu/$MoSi_2$(200nm) sample annealed at 800°C for 2 minutes.

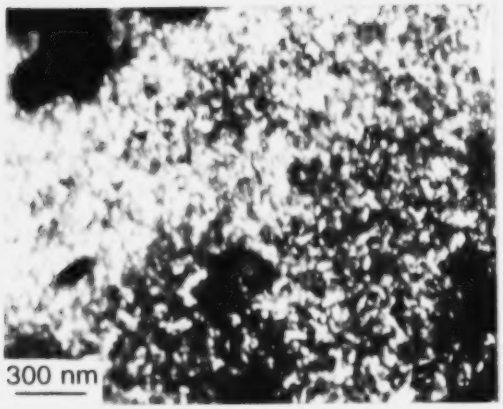

a)Dark field image of $MoSi_2$(400nm) annealed at 600°C for 2 minutes.

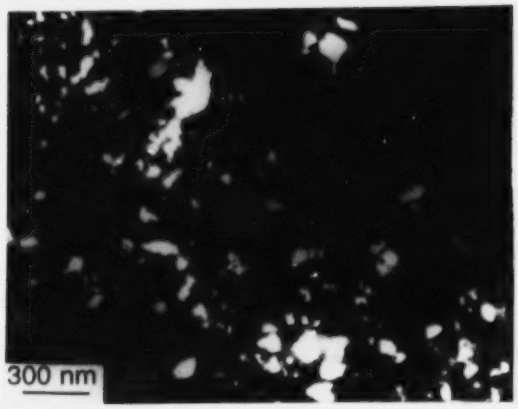

b) Dark field image of $MoSi_2$(400nm) annealed at 850°C for 10 minutes.

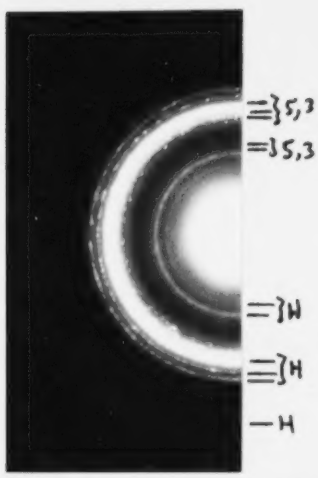

H - $MoSi_2$(Hex)
5,3 - Mo_5Si_3

c) SAD pattern corresponding to a).

d) SAD pattern corresponding to b).

d-spacing/Intensity	$MoSi_2$(hex)	Mo_5Si_3(tet)
0.394 med.	0.398 (10)	- -
0.344 med.	0.337 (50)	- -
0.327 weak	- -	0.324 (25)
0.302 weak	- -	0.305 (21)
0.245 med.	- -	0.245 (25)
0.218 1	0.217 (100)	0.219 (38)
0.212 2	- -	0.211 (100)
0.200 3	0.200 (16)	- -
0.188 4	0.188 (40)	- -
0.147 weak	0.147 (20)	- -
0.134 weak	0.133 (16)	- -

e) Table, indexing of SAD patterns from c) and d).

Figure 5-36: Comparison of the grain size and phases for Si/Cu/$MoSi_2$(400nm) samples.

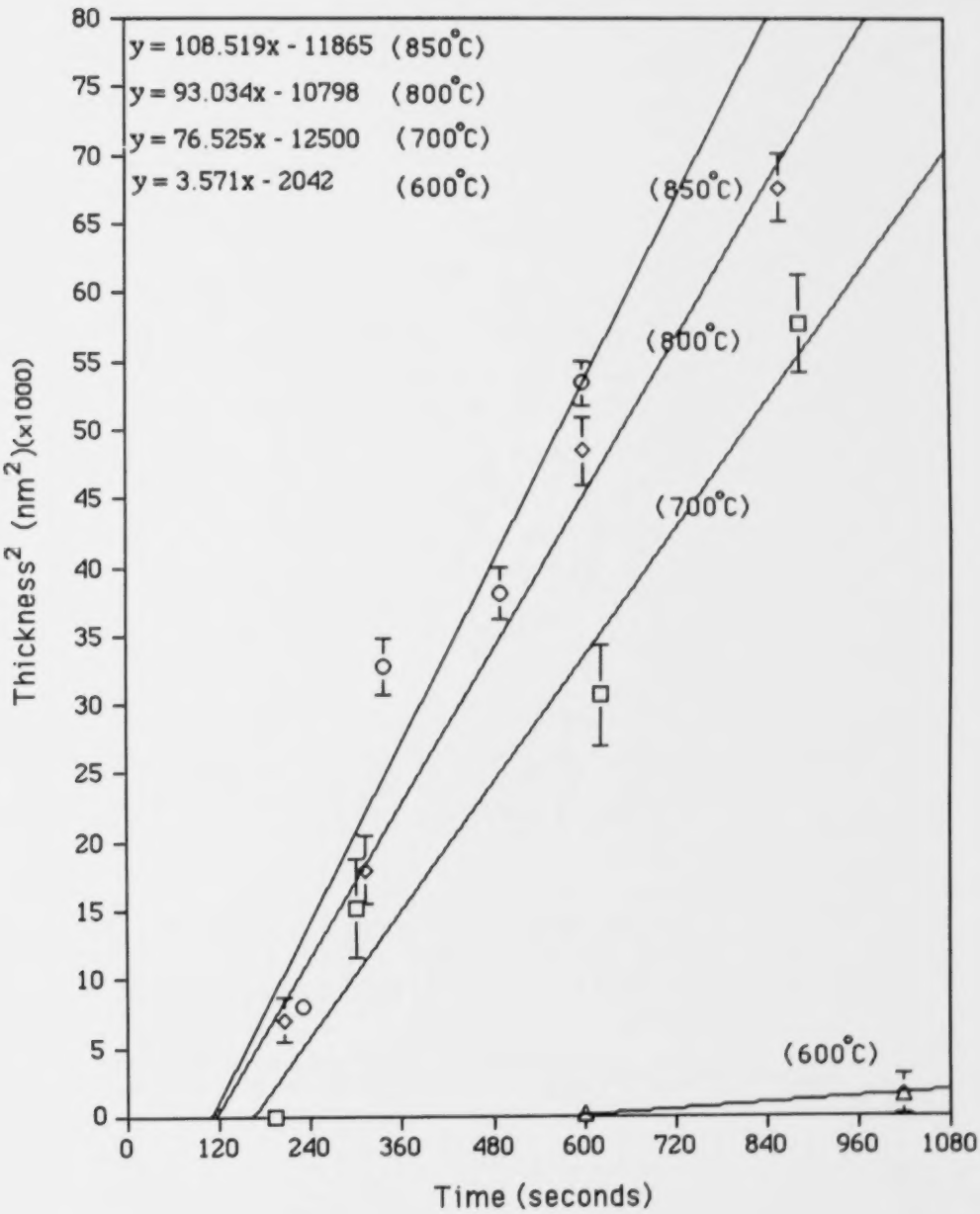

Figure 5-37: Kinetic plots for 600°C, 700°C, 800°C and 850°C data for Si/Cu/$MoSi_2$(400nm) samples.

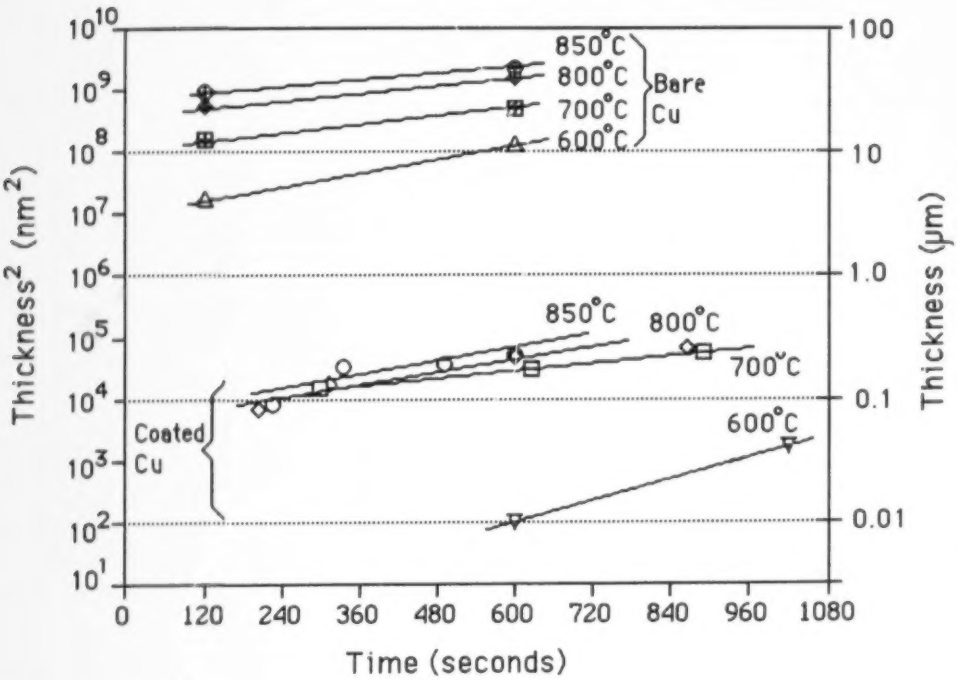

Figure 5-38: Log plot of the data from Figure 5-37.

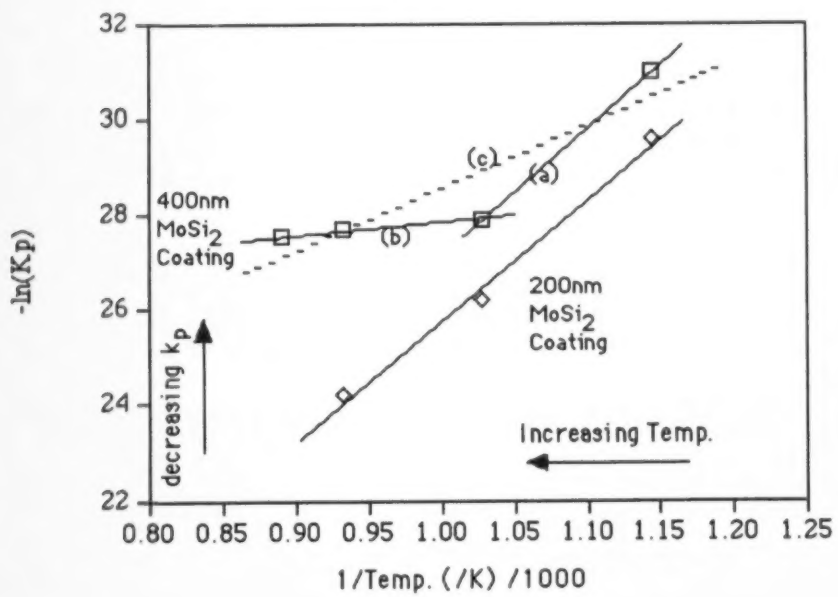

Figure 5-39: Arrhenius plot of the parabolic rate constants from Figure 5-37 ($MoSi_2$(400nm) coating) and Figure 5-25 ($MoSi_2$(200nm) coating).

Table 5-3: A comparison of rate constants, apparent activation energy, oxide thickness at 15 minutes, and copper consumed at 15 minutes for bare copper and Si/Cu/$MoSi_2$(400nm).

		600°C	700°C	800°C	850°C
k_p (cm^2/s)	Cu/$MoSi_2$ (400nm)	3.57×10^{-14} (64400x)	7.65×10^{-13} (9050x)	9.30×10^{-13} (22580x)	1.09×10^{-12} (26150x)
	Bare Copper	2.30×10^{-9}	6.92×10^{-9}	2.10×10^{-8}	2.85×10^{-8}
Apparent Activation Energy	Cu/$MoSi_2$ (400nm)	(a) 220 kJ/mol (b) 22 kJ/mol		(c) 110 kJ/mol	
	Bare Copper	83.6 kJ/mol			
Oxide Thickness at 15 min.	Cu/$MoSi_2$ (400nm)	34 nm (415x)	238 nm (111x)	270 nm (176x)	293 nm (191x)
	Bare Copper	14100 nm	26500 nm	46900 nm	56000 nm
Cu consumed at 15 min.	Cu/$MoSi_2$ (400nm)	20 nm (430x)	138 nm (117x)	157 nm (182x)	170 nm (200x)
	Bare Copper	8600 nm	16160 nm	28600 nm	34150 nm

*Round brackets indicate the improvement over bare copper.

Chapter 6

Conclusions and Recommendations

6.1 Conclusions

In this research, electron microscopy work has been used to study the effectiveness of a sputter deposited $MoSi_2$ diffusion barrier on copper. Substrate/Cu/$MoSi_2$ metallizations were annealed, in an air ambient, in the temperature range of 600°C to 850°C for times of 15 minutes or less. The main work was done on two coating thicknesses, namely $MoSi_2$(200nm) and $MoSi_2$(400nm). A number of conclusions can be made based on the experimental results.

1. Silicon from the $MoSi_2$ layer dissolves into the copper layer forming a Cu-Si solid solution.
2. The $MoSi_2$(200nm) coating transforms from as deposited amorphous structure to $MoSi_2$(hexagonal), Mo_5Si_3, and Mo_3Si structures at high temperatures.
3. The $MoSi_2$(400nm) coating transforms from as deposited amorphous structure to $MoSi_2$(hexagonal) and Mo_5Si_3 upon annealing at high temperatures.
4. $MoSi_2$ coatings reduce the amount of copper oxide formation on the surface of the metallization systems. The parabolic rate constants and oxide thicknesses at 15 minutes are given in Table 6-1 for both $MoSi_2$(200nm) and $MoSi_2$(400nm) coatings.

Table 6-1: Parabolic rate constants and oxide formation at 15 minutes for 200nm and 400nm $MoSi_2$ coatings on copper.

	Temperature (°C)	k_p (cm^2/s)	Oxide thickness at 15 minutes (nm)
$MoSi_2$(200nm) coating	600	1.45×10^{-13}	103
	700	4.37×10^{-12}	570
	800	2.95×10^{-11}	1500
	850	- -	>3700
$MoSi_2$(400nm) coating	600	3.57×10^{-14}	34
	700	7.65×10^{-13}	238
	800	9.11×10^{-13}	266
	850	1.09×10^{-12}	293

6.2 Recommendations

1. To fully understand the mechanism of copper diffusion through $MoSi_2$, further analysis is needed on the $MoSi_2$ layer to characterize its phase transformations. The transformation to the lower silicides is directly linked to the loss of silicon into the copper. Preventing the loss of silicon from the $MoSi_2$ to copper needs to be addressed. A number of barrier layers are in current use between copper and silicon, and are referenced in the main body of the text.

2. Since the grain size is linked to low temperature diffusion, a study on the control of the grain size of crystalline $MoSi_2$ which forms from the amorphous as deposited structure could improve the diffusion of copper through the layer.

3. Resistivity measurements of the metallization system would need to be completed to determine the usefulness of the system. The Cu-Si solid solution, which presently forms, is not desirable, since the silicon in the copper lattice acts as scattering sites for electrons increasing the electrical resistance.

4. If this system were to be designed for powder metallurgy samples, the effect of sintering needs to be studied. A silver layer on the $MoSi_2$ barrier may improve sintering and also act as a buffer layer, dissolving copper that diffuses through the diffusion barrier.

5. Refractory metal carbides, such as NbC or TaC, could be studied as diffusion barriers to copper. Carbides have an advantage over the silicides, since carbon does not dissolve appreciably in copper.

References

1. N. Birks, G.H. Meier, *Introduction to High Temperature Oxidation of Metal*, Edward Arnold Publ., (1983).

2. S.Mrowec, A. Stoklosa, K. Goldewski, *Crystal Lattice Defects*, Vol. 5, 239, (1974).

3. S. Mrowec, A. Stoklosa, *Oxid. of Metals*, Vol.3 No. 3, 291, (1971).

4. C. Wagner, *Phys. Chem.*, Vol. 21, 25, (1933).

5. G. J. Yurek, J. P. Hirth, R. A. Rapp, *Oxidation of Metals*, Vol. 8, No. 5, 265, (1974).

6. G. Garnaud, *Oxidation of Metals*, Vol. 11, No. 3, 127, (1977).

7. G. Valensi, *Pittsburgh International Conference on Surface Reactions*, Corrosion Publ. Co., 156. (1948).

8. J. Paidassi, *Acta Metall.*, Vol. 6, 216, (1958).

9. J. Oudar, *L'oxydation des Metaux*, Vol. 2, Benard ed., Gauthier-Ballars, Paris, (1964).

10. S. Mrowec, *Oxidation of Metals*, Vol. 6, 178, (1973).

11. V. Ananth, S.K. Bose, S.C. Sircar, *Scripta Metallurgica*, Vol. 14, 687, (1980).

12. S.K. Roy, S.K. Bose, S.C. Sircar, *Oxidation of Metals*, Vol. 35, No. 1/2, 1, (1991).

13. W.J. Moore, B. Selikson, *J. Chem. Phys.*, Vol. 19, 1539, (1951), and Vol. 20, 927, (1952).

14. W.J. Moore, G.W. Castellan , *J. Chem. Phys.*, Vol. 17, 41, (1949).

15. K. Hauffe, *Oxidation of Metals*, Plenum Press, 165, (1965).

16 O. Kubaschewski, B.E. Hopkins, *Oxidation of Metals and Alloys*, Butterworths Scientific Publications, London England, 50, (1967).

17. F.S. Kroger, *The Chemistry of Imperfect Crystals*, Vol. 3, North Holland Publ. Co., Amsterdam, 2nd Ed., 89, (1974).

18. K. Hauffe, P. Kofstad, *J. Electrochem.*, Vol. 59, 399, (1955).

19. J.A. Leroux, E. Raub, *J. Chem.*, Vol. 188, 205, (1930).

20. B.E. Deal, A.S. Grove, *J. Appl. Phys.*, Vol. 36, 3770, (1965).

21. A.G. Revesz, B.J. Mrstik, *J. Electrochem. Soc.*, Vol. 133, 31, (1986).

22. P.J. Jorgensen, *J. Chem. Phys.*, Vol. 37, 874, (1962).

23. S.S. Christy, J.B. Condon, *J. Electrochem. Soc.*, Vol. 128, 2170, (1981).

24. F. Rochet, B. Agius, S. Rigo, *J. Electrochem. Soc.*, Vol. 131, 914, (1984).

25. E.A. Irene, *J. Electrochem. Soc.*, Vol.121, 1613, (1965).

26. F.S. Pettit, *Coatings for High Temperature Applications*, Applied Science, London, (1983).

27. P. Kofstad, *High Temperature Oxidation of Metals*, Wiley, New York, (1967).

28. J. Stringer, *Corros. Sci.*, Vol. 10, 513, (1970).

29. P. Hancock, R.C. Hurst, *Advances in Corrosion Science and Tech.*, Plenum Press, New York, (1974).

30. N.B. Pilling, R.E. Bedworth, *J. Inst. Met.*, Vol. 29, 529, (1923).

31. C. Zhou, W.W. Smeltzer, *High Temp. Oxid. and Sulph. Proc. Proceedings*, Vol. 22, 43, (1990).

32. P. Sayers, W. Petsis, ISHM, 11, (1987).

33. R.N. Godin, *Hybrid Circuit Tech.*, Aug., 31, (1990).

34. T.S. Wu, T. Shiramatsu, S.N. Chen, *IEEE Ch1457-1*, 11, (1979).

35. C.Y. Kuo, *U.S. Patent*, #4 122 232, (1978).

36. C.Y. Kuo, *U.S. Patent*, #4 409 261, (1983).

37. M.A. Nicolet, *Thin Solid Films*, Vol. 52, 415, (1978).

38. J.W.M. DuMond, J.P. Youtz, *Phys. Rev.*, Vol. 48, 703, (1935).

39. D. Gupta, K.N. Tu, K.W. Asai, *Phys. Rev. Lett.*, Vol. 35, 796, (1975).

40. H.S. Chen, L.C. Kimerling, J.M. Poate, W.L. Brown, *Appl. Phys. Lett.*, Vol. 32, 461, (1978).

41. M. Wittmer, *J. Vac. Sci. Technol. A2(2)*, Apr.-June, 273, (1984).

42. S.U. Campisano, E. Costanzo, E. Rimini, *Philos. Mag.*, Vol. 35, 1333, (1977).

43. K. Nakamura, S.S. Lau, M.A. Nicolet, J.W. Mayer, *Appl. Phys. Lett.*, Vol. 28, 277, (1976).

44. K.N. Tu, R. Rosenberg, *Thin Solid Films*, Vol. 13, 163, (1972).

45. R.G. Kirsch, J.M. Poate, M Eibschutz, *Appl. Phys. Lett.*, Vol. 29, 772, (1976).

46. A. Hiraki, E. Lugujjo, M.A. Nicolet, J.W. Mayer, *Phys. Status Solidi A*, Vol.7, 401, (1971).

47. A. Hiraki, E. Lugujjo, J.W. Mayer, *J. Appl. Phys.*, Vol. 43, 3643, (1972).

48. A. Hiraki, E. Lugujjo, *J. Vac. Sci. Technol.*, Vol. 9, 155, (1972).

49. E.I. Allessandrini, D.R. Campbell, K.N. Tu, *J. Appl. Phys.*, Vol. 45, 4888, (1974).

50. S.P. Murarka, *Silicides for VLSI Applications*, Academic Press Inc., (1983).

51. B.L. Crowder, S. Zirinsky, *IEEE J. Solid State Circuits*, SC-14, 291, (1979).

52. R. Pretorius, *J. Electrochem. Soc.*, Vol. 128, 107, (1981).

53. R. Pretorius, W. Strydom, J.W. Mayer, C. Comrie, *Phys. Rev.*, Vol. B22, 1885, (1980).

54. M. Bartur, M.A Nicolet, *Appl. Phys. Lett.*, Vol. 40, 175, (1982).

55. J.R. Chen, Y.C Liu, S. D. Chu, *Appl. Phys. Lett.*, Vol. 40, 263, (1982).

56. S.P. Murarka, C. Chang, *Appl. Phys. Lett.*, Vol. 37, 639, (1980).

57. S.P. Murarka, D.B. Fraser, W.S. Lindenberger, A.K. Sinha, *J. Appl. Phys.*, Vol. 51, 3241, (1980).

58. T. Mochizuki, M. Kashiwagi, *J. Electrochem. Soc.*, Vol. 127, 1128, (1980).

59. T. Inoue, K. Koike, *Appl. Phys. Lett.*, Vol. 33, 826, (1978).

60. A.K. Sinha, *J. Vac. Sci. Technol.*, Vol. 19, 778, (1981).

61. D.R. Wolters, *J. Electrochem Soc.*, Vol. 127, 2073, (1980).

62. D.R. Wolters, *J. Electrochem Soc.*, Vol. 127, 2073, (1980).

63. S.P. Murarka, *J. Vac. Sci. Technol.*, Vol. 17, 775, (1980).

64. T. Shibata, A. Wakita, T.W. Sigmon, J. F. Gibbons, T.R. Cass, *Appl. Phys. Lett.*, Vol. 40, 77, (1982).

65. S. Zirinsky, W. Hammer, F. d'Heurle, J. Baglin, *Appl. Phys. Lett.*, Vol. 33, 76, (1978).

66. F. Mohammadi, K.C. Sarawat, J.D. Meindl, *Appl. Phys. Lett.*, Vol. 35, 529, (1979).

67. M. Bartur, M.A. Nicolet, *Appl. Phys. Lett.*, Vol. 40, 175, (1982).

68. A.S. Grove, *Physics and Technology of Semiconductor Devices*, Wiley, New York, Chp. 2, (1967).

69. A.K. Vasudevan, J.J. Petrovic, *Mater. Sci. Eng.*, Vol. A155, 1, (1992).

70. J.J. Petrovic, *MRS Bulletin*, July, 35,(1993).

71. T.C. Chou, T.G. Nieh, *Thin Solid Films*, Vol. 214, 48, (1992).

72. D.A Berztiss, R.R. Cerchiara, E.A. Galbransen, F.S. Pettit, G.H. Meier, *Mater. Sci. Eng.*, Vol. A155, 165, (1992).

73. J.J. Petrovic, R.E. Honnell, A.K. Vasudevan, *Mater. Res. Soc. Symp. Proc.*, Vol. 194, 123, (1990).

74. J.J. Petrovic, R.E. Honnell, *Ceram. Eng. Sci. Proc.*, Vol. 11, 734, (1990).

75. A. Mueller, G. Wang, R.A Rapp, E.L. Courtright, T.A. Kirchen, *Mater. Sci. Eng.*, Vol. A155, 199, (1992).

76. T.A. Kircher, E.L. Courtright, *Mater. Sci. Eng.*, Vol. A155, 67, (1992).

77. J Schilichting, *High Temp. High Pressures*, Vol. 10, 241, (1978).

78. Von E. Fitzer, *Plansee Proc. 2nd Seminar Reutte/Tyrol*, 56, (1955).

79. T.C. Chou, T.G. Nieh, *J Mater Res.*, Vol. 8, 214, (1993).

80. C.H. Ho, S. Prakash, H.J. Doerr, C.V. Deshpandey, R.F. Bunshab, *Thin Solid Films*, Vol. 207, 294, (1992).

81. T.C. Chou, T.G. Nieh, *JOM*, Dec., 15, (1993).

82. P.J. Meschter, *Met. Trans.*, Vol. A23, 1763, (1992).

83. C.D. Wirkus, D.R. Wilder, *J. Am. Ceram. Soc.*, Vol. 49, 173, (1966).

84. T.C. Chou, T.G. Nieh, *Scripta Met. et Mat.*, Vol. 26, 1637, (1992).

85. T.C. Chou, T.G. Nieh, *Mat. Research Proc.*, Vol. 288, 965, (1993).

86. J.R. Cooper, R.L. Hanslen, *J. Chem. Phys.*, Vol. 39, 248, (1963).

87. G. Santoro, R.T. Dolloff, *J. Appl. Phys.*, Vol. 39, 2293, (1968).

88. W.S. Williams, *Phys. Rev.*, Vol. A135, 505, (1964).

89. L. E. Toth (ed.), *Transition Metal Carbides and Nitrides*, Academic Press Inc., New York, (1971).

90. S. Motojima, K. Funahashi, K. Kurosawa, *Thin Solid Films*, Vol. 189, 73, (1990).

91. W.C. Tripp, H.C. Grahan, *J. Electrochem. Soc.*, Vol. 118, 1195, (1971).

92. E. Randich, D.D. Allred, *Thin Solid Films*, Vol. 83, 393, (1981).

93. J.R Shappirio, J.J. Finnegan, *Thin Solid Films*, Vol. 107, 81, (1983).

94. J.R. Shappirio, J.J. Finnegan, R.A. Lux, D.C. Fox, *Thin Solid Films*, Vol. 119, 23, (1984).

95. L.K. Elbaum, M. Wittmer, *Thin Solid Films*, Vol. 107, 111, (1983).

96. L. Kaufman, E.V. Cougherty, *Tech. Documentary Rep., 63-4096 Part II*, Sept., (1965).

97. V. Svistunov, A. Beketov, E. Knyshev, N. Obabkov, V. Novgoradtsev, *J. Less Common Met.*, Vol. 67, 287, (1979).

98. L. K. Elbaum, M. Wittmer, C.Y. Ting, J.J. Cuomo, *Thin Solid Films*, Vol. 104, 81, (1983).

99. M. Wittmer, *J. Appl. Phys.*, Vol. 53, 1007, (1982).

100. M. Wittmer, *Appl. Phys. Lett.*, Vol. 36, 456, (1980).

101. C.Y. Ting, *J. Vac. Sci. Technol.*, Vol. 21, 14, (1982).

102. H.Y. Yang, X.A. Xhao, M.A. Nicolet, *Thin Solid Films*, Vol. 158, 45, (1988).

103. M. Ostling, S. Nygren, C.S. Peterson, *Thin Solid Films*, Vol. 145, 81, (1986).

104. M.A. Nicolet, S.S. Lau, *VLSI Science: Microstructural Science*, Vol. 6, Chp. 6, (1983).

105. C.Y. Kuo, *Proc. of Intnl. Symp. of Microelectronics*, Nov., 472, (1985).

106. P. Shewmon, *Diffusion in Solids*, 2nd Ed., Minerals Metals and Materials Society Publication, (1989).

107. Frost, Sulliva, NoA 1365, Sept., (1985).

108. P.T.B. Shaffer, *Plenum Press Handbook of High Temperature Materials No. 1 Materials Index*, Plenum Press, New York, (1964).

109. G.V. Samsonov, *Plenum Press Handbook of High Temperature Materials No. 2 Materials Index*, Plenum Press, New York, (1964).

110. E.A.Brandes, *Smithells Metals Reference Book*, 6th Ed., Butterworths and Co., (1983).

111. F.K. Storms, *Refractory Carbides*, Academic Press, New York, (1967).

112. E.L. Muetterties, *The Chemistry of Boron and its Compounds*, Wiley, New York, (1967).

113. *Powder Diffraction Files*, JCPDS- International center for diffraction data.

114. J.J. Licari, L.R. Enlow, *Hybrid Microcircuit Technology Handbook*, New Jersey, (1988).

115. C. Wagner, *Handbuch der Metallphysik*, Vol. 1, Part 2, 144, (1940).

116. A. Ronnquist, H. Fischmeister, *J. Inst. of Metals*, Vol. 89, 65, (1960-61).

117. M. Matyas, *Czechoslovak J. Physics*, Vol. 5, 214, (1955).

118. E.A. Gulbransen, W.R. McMillan, *J. Electrochem. Soc.*, Vol. 99, 393, (1952).

119. D.W. Bridges, J.P. Baur, G.S. Baur, W.M. Fassell, *J. Electrochem. Soc.*, Vol. 104, 749, (1957).

120. C.G. Cruzan, H.A. Miley, *J. Appl. Physics*, Vol. 11, 631, (1940).

121. F. Bouillon, *Bull. Soc. Chim. Belg.*, Vol. 60, 451, (1951).

122. W.W. Harris, F.L. Ball, A.T. Gwathmey, *Acta Met.*, Vol. 5, 574, (1957).

123. A. Dravnieks, *J. Amer. Chem. Soc.*, Vol. 72, 3761, (1950).

124. D.G. Ivey, G.R. Piercy, *Thin Solid Films*, Vol. 149, 73, (1987).

125. J. Li, J.W. Mayer, *Materials Chem. Phys.*, Vol. 32, 1, (1992).

126. K. Holloway, P.M. Fryer, *Appl. Phy. Letters*, Vol. 57,1737, (1990).

127. K. Holloway, P.M. Fryer, C. Cabral, J.M. Harper, P.J. Bailey, K.H. Kelleher, *J. Appl. Phys.*, Vol. 71, 5433, (1992).

128. C.S. Choi, G.C. Xing, G.A. Ruggles, C.M. Osborn, A.S. Shah, J.D. Hunn, *J. Electrochem. Soc.*, Vol. 138, 3062, (1991).

129. E. Kolawa, P.J. Pokela, J.S. Reid, J.S. Chen, R.P. Ruis, M.A. Nicolet, *IEEE Electron. Device Letters*, Vol. 12, 321,(1991).

130. D. Brett, *Thin Film Lecture Notes*, Dept. of Electrical Eng., Univ. of Alberta, (1992).

131. Y. Tamou, J. Li, S.W. Russell, J.W. Mayer, *Nucl. Instr. Methods B*, Vol. 64, 130, (1992).

132. D.Y. Shih, C.A. Chang, J. Paraszak, S. Nunes, J. Cataldo, *J. Appl. Phys.*, Vol. 70, 3052, (1991).

133. S.W. Russell, J. Li, J.W. Strane, J.W. Mayer, *Mater. Res. Soc. Symp. Proc.*, (1992).

Appendix A

Calculations Used for Tables 2-3a to d.

	ρ(g/cm^3)	MW(g/mol)
Cu_2O	6.11	143.0
CuO	6.51	79.5
Cu	8.96	63.5

$$2Cu + \frac{1}{2}O_2 = Cu_2O$$

$$Cu + \frac{1}{2}O_2 = CuO$$

For unit volume (1 cm^3) , there are 6.11g of Cu_2O

$$(6.11\ g)(143.0\ g/mol)^{-1} = 4.27 \times 10^{-2}\ mol$$

There are 4.27×10^{-2} mol of Cu_2O, therefore there are 4.27×10^{-2} mol of oxygen.

$$(4.27 \times 10^{-2}\ mol)\ (16\ g/mol) = 0.684\ g$$

For 1 cm^3 Cu_2O there are 0.684 g of oxygen consumed. ...(1)

Similarly, for CuO 1.31 g of oxygen are consumed. ...(2)

The values for Table 2-3a-d were calculated as follows

k_p(g^2/cm^4·s) and %CuO were taken from literature data.

$$\Delta m^2/cm^4 = k_p \cdot \text{time} \qquad ...(3)$$

$$\Delta m/cm^2 = \text{sqrt}\ (\Delta m^2/cm^4) \qquad ...(4)$$

For 850°C and 800°C (where the %CuO is negligible)

$$\text{Approx. oxide thickness} = \frac{(\Delta m/cm^2)}{0.684\ g/cm^3} \qquad ...(5)$$

$$k_p(cm^2/s) = \frac{k_p(g^2/cm^4 \cdot s)}{(0.684\ g/cm^3)^2} \qquad ...(6)$$

For 700°C and 600°C (where the %CuO is not negligible)

$$\text{Approx. oxide thickness} = \frac{\Delta m/cm^2 \times 100}{(0.684)(\%Cu_2O)+(1.31)(\%CuO)} \quad \ldots(7)$$

$$k_p(cm^2/s) = \frac{k_p(g^2/cm^4 \cdot s) \times 100}{(0.684)^2(\%Cu_2O)+(1.31)^2(\%CuO)} \quad \ldots(8)$$

From equation (1) there are 5.426 g/cm^3 of copper in Cu_2O.

From equation (2) there are 5.200 g/cm^3 of copper in CuO.

For 1 mole of Copper 11.7 cm^3 of Cu_2O can be formed, and

12.2 cm^3 of CuO can be formed.

Appendix B

Factors Which Affect Adhesion

The quality of adhesion depends on the condition of the interfacial layer between film and substrate. There are several ways in which good adhesion may be achieved [130], and can be a combination of the following: i) Mechanical anchoring where the film can mechanically anchor to a relatively rough surface. ii) Chemical compound formation, between film and substrate, which may give strong adhesion characteristics if chemical bonding occurs. iii) Diffused layer, where there is a gradual change in composition across the cross section. Partial solubility is required for diffusion. iv) Pseudo-diffused; this is formed by implantation of the film species into the substrate, which may occur in sputter deposited films.

There are several additional ways in which adhesion may be improved. They include: a) A clean substrate without unwanted impurities or oxides. b) An intermediate layer to promote adhesion, which usually forms a chemical compound or a diffused layer deposited between the film and substrate. c) A deposition technique where atoms arrive with a high energy and improve adhesion through their implantation. d) Substrate temperature may have a strong effect, as higher temperatures accelerate diffusion or compound formation. However, thermal stresses may be induced upon cooling.

Table B-1 gives a summary of some copper/metal thin film reactions. Group IV-A metals react with copper at lower temperatures (350°C - 450°C) and form compounds. The reaction with Hf though has not been characterized. Group V-A and VI-A metals are immiscible in copper except for W which forms a solid solution. They generally do not react until high temperatures are reached, >700°C. Copper reacts with most of the near noble and noble metals at relatively low temperatures [131]. Group VIII-A elements form compounds or solid solutions with copper at low temperatures as do Al and Au. Pd and Pt have complete solid solubility with ordered compounds forming

at low temperatures [132]. Mg and Sb have the lowest eutectic temperatures which are around 500°C. From Table B.1, it could be surmised that the low temperature compound forming metals could prove to be adhesion promoters between copper and SiO_2. One example of this is the formation of TiOx and Ti_5Si_3 at the Cu/SiO_2 interface which has significantly improved the adhesion over just copper on SiO_2. By annealing Cu-Ti alloy films on SiO_2 substrates in vacuum at 500°C, Ti segregates at the film/substrate interface due to the interfacial reaction between Ti in the Cu-Ti alloy and SiO_2 substrate [133].

Table B-1: Summary of initial phase formation in copper/metal bilayers. The metal, reaction temperature, and alloy properties are shown. S.S. stands for solid solution.

					III-B
					Al 250°C $CuAl_2$
IV- A	V-A	VI-A	VIII-A		
Ti 350°C TiCu	V >750°C immiscible	Cr >700°C immiscible	Co >450°C S.S.	Ni 250°C S.S.	
Zr 400°C CuZr+S.S.	Nb >450°C immiscible	Mo >750°C immiscible	I B	Pd 250°C Cu_3Pd	
Hf >450°C ?	Ta >750°C immiscible	W 750°C S.S.	Au 150°C Cu_3Au	Pt 300°C Cu_3Pt	

Appendix C

Calculation for the Reduction of CuO to Copper by Ion Milling

Based on calculations from Ref. 124

U = flux ~ 50 $\mu A/cm^2$

R = fraction reflected

A conservative damage depth for copper would be ~10nm.

(13° angle of inclination), (R=0.5).

Assume ions to be singly charge (some are likely to be doubly charged ~10%).

$$\frac{\#\text{of ions}}{\text{area} \cdot \text{time}} = \frac{R \cdot U}{q} = \frac{(0.5) \cdot 50\ \mu A/cm^2}{1.6 \times 10^{-13}\ \mu As/\text{ion}}, \quad q = \text{charge/ion} = 1.6 \times 10^{-19}\ C/\text{ion}$$

$$= 3 \times 10^{12}\ \text{ions/mm}^2 \cdot \text{sec.}$$

For CuO there are ~50 molecules/nm^3.

For an area of 1.0 mm^2 and a depth of 10 nm, the interaction volume is 10^{13} nm^3.

Therefore, there are 5×10^{14} molecules in the interaction volume.

Assuming the energy is equally divided among the molecules in the solid,

In 1 second, there is 1 ion deposited for about every 200 molecules.

If the average ion has an energy of 4000 eV.

There is ~20 eV transferred to each molecule.

Therefore: (20 eV) $(1.602 \times 10^{-19}$ J/eV) $(6.02 \times 10^{23}$ molec/mole)

= 1 930 kJ.

$$Cu + \frac{1}{2} O_2 = CuO \qquad \Delta G(300^\circ K) = -127\ kJ.$$

There is enough kinetic energy to reduce CuO to metallic copper.

Appendix D

Raw Data

Table D-1: Raw data for the oxide thickness measurements of bare copper.

Temperature (°C)	Time (seconds)	Oxide Thickness (mm)	Copper Consumed (calculated) (mg), (mm)
850°C	204	31.0	16.8, (18.9)
	264	38.5	20.9, (23.5)
	420	43.8	23.8, (26.7)
	900	55.5	30.1, (33.8)
800°C	204	26.5	14.4, (16.2)
	312	31.8	17.3, (19.4)
	600	39.3	21.3, (24.0)
	864	46.1	25.0, (28.1)
700°C	192	14.5	7.87, (8.84)
	300	16.5	8.95, (10.1)
	624	23.2	12.6, (14.1)
	888	26.0	14.1, (15.9)
600°C	192	6.30	3.42, (3.84)
	324	6.90	3.74, (4.21)
	600	12.1	6.57, (7.38)
	1020	14.8	8.03, (9.02)

Table D-2: Raw data for the oxide thickness measurements for Si/Cu/$MoSi_2$(200nm) samples.

Temperature (°C)	Actual Time (seconds)	Oxide Thickness (nm)	Copper Consumed (calculated) (mg), (nm)
850°C	234	3460	1800, (2010)
	348	3780	1965, (2200)
	420	3470	1805, (2020)
	528	3650	1900, (2120)
800°C	150	366	190, (213)
	300	604	314, (351)
	564	1148	597, (667)
700°C	228	200	104, (116)
	348	269	140, (156)
	612	451	235, (262)
600°C	152	20.5	11.0, (11.9)
	320	35.0	18.0, (20.3)
	644	85.0	44.0, (49.4)

Table D-3: Raw data for the oxide thickness measurements for Si/Cu/$MoSi_2$(400nm) samples.

Temperature (°C)	Actual Time (seconds)	Oxide Thickness (nm)	Copper Consumed (calculated) (mg), (nm)
850°C	204	90	46.8, (52.3)
	336	181	94.0, (105)
	492	195	101, (113)
	600	231	120, (134)
800°C	204	84	44.0, (48.8)
	312	134	70.0, (78.0)
	600	220	114, (128)
	864	260	135, (151)
700°C	192	0	0, (0)
	300	123	64.0, (71.5)
	624	175	91.0, (102)
	888	240	125, (140)
600°C	192	0	0, (0)
	324	0	0, (0)
	600	<10	<5.20, (<5.81)
	1020	40	21.0, (23.3)